Progress in Particle and Nuclear Physics 62 (2009) 257–303

Contents lists available at ScienceDirect

Progress in Particle and Nuclear Physics

journal homepage: www.elsevier.com/locate/ppnp

Review

Research opportunities at the upgraded HIγS facility

Henry R. Weller [a,b,*], Mohammad W. Ahmed [a,b], Haiyan Gao [a,b], Werner Tornow [a,b], Ying K. Wu [a,c], Moshe Gai [d], Rory Miskimen [e]

[a] *Duke University, Durham, NC 27708-0308, USA*

[b] *Triangle Universities Nuclear Laboratory (TUNL), Box 90308, Durham, NC 27708-0308, USA*

[c] *The Duke Free Electron Laser Laboratory (DFELL), Box 90319, Durham, NC 27708-0319, USA*

[d] *LNS at Avery Point, University of Connecticut, 1084 Shennecossett Road, Groton, CT 06340, USA*

[e] *Department of Physics, 1126 Lederle Graduate Research Tower (LGRT), University of Massachusetts, Amherst, MA 01003-9337, USA*

ARTICLE INFO

Keywords:
Free Electron Laser (FEL)
Compton back-scattering
Polarized γ rays
Nuclear structure
Nuclear Resonance Fluorescence (NRF)
Photon scattering
Photodisintegration
Nuclear astro-physics
Stellar helium burning
Optical time projection chamber
Gerasimov–Drell–Hearn (GDH) sum rule
Frozen spin polarized target
Optically-pumped polarized ^{3}He
Nucleon polarizabilities
Compton scattering
Spin polarizabilities
Photo-nuclear physics

ABSTRACT

The High Intensity γ-ray Source (HIγS) is a joint project between the Triangle Universities Nuclear Laboratory (TUNL) and the Duke Free Electron Laser Laboratory (DFELL). This facility utilizes intra-cavity back-scattering of the FEL light in order to produce intense γ-ray beams. An upgrade which allows for the production of γ-rays up to energies of about 100 MeV having total intensities in excess of 10^8/s is essentially complete. The primary component of the upgrade is a 1.2 GeV booster-injector which makes it possible to replace lost electrons at full energy. In addition, an upgrade of the present linear undulator to a helical system has made it possible to produce nearly 100% linear and circularly polarized beams. The full system was commissioned in the early part of 2007. A nuclear physics research program using beams at energies below 50 MeV commenced in the fall of 2007. The proposed experimental program includes low-energy studies of nuclear reactions of importance in nuclear astrophysics as well as studies of nuclear structure using the technique of nuclear resonance fluorescence (NRF). Few-body nuclear physics problems will also be addressed by studying photodisintegration of d, ^{3}He and ^{4}He. Future double-polarization experiments include a study of the Gerasimov–Drell–Hearn Sum Rule for the deuteron and ^{3}He, and an extensive Compton scattering program designed to probe the internal structure of the nucleon. A major focus of these studies will be the measurement of the electric and magnetic polarizabilities as well as the spin-polarizabilities of the proton and the neutron. This review will describe the principles of operation of the upgraded facility, followed by a description of the performance which has been achieved to date, and a projection of the performance anticipated in the near future. Following this, we will review several of the research areas of nuclear physics which are accessible using this facility, and describe both the results to date and proposed experiments being developed for the future.

Contents

* Corresponding author at: Triangle Universities Nuclear Laboratory (TUNL), Box 90308, Durham, NC 27708-0308, USA.
E-mail address: weller@tunl.duke.edu (H.R. Weller).
URL: http://www.tunl.duke.edu/higs/ (H.R. Weller).

0146-6410/$ – see front matter © 2008 Elsevier B.V. All rights reserved.
doi:10.1016/j.ppnp.2008.07.001

1. Introduction

The discovery of the Compton effect in the early 1920's via the scattering of x-rays from electrons in metals [1] was a critical moment for Quantum Mechanics still under development by providing the first experimental evidence of the wave-particle duality as displayed by x-ray electromagnetic radiation. Another four decades would pass before the Compton effect was recognized as a useful mechanism to convert low energy photons to very high energy x-ray and γ-ray photons. In 1963, Milburn, and Arutyunian and Tumanian, independently proposed a method of producing very high energy γ-ray beams via Compton back-scattering of photons with high-energy electrons in charged particle accelerators [2,3]. In the following years, the first experimental demonstrations of high energy γ-ray production using Compton scattering were carried out by several groups around the world, including Kulikov et al. with the 600 MeV synchrotron [4], Bemporad et al. with the 6.0 GeV Cambridge Electron Accelerator [5], and Ballam et al. with the 20 GeV Stanford linear accelerator [6,7].

While successful, the first demonstrations of γ-ray production by Kulikov et al. [4] and Bemporad et al. [5] had a very low γ-photon yield. With much improved photon yields (100–500 s^{-1}), Ballam et al. [7] at the Stanford Linear Accelerator Center (SLAC) were able to carry out the first physics measurements using the Compton γ-ray beam to study the photo-production

Table 1
Parameters of major Compton gamma source facilities around the world

Project name	LADON[a]	LEGS	ROKK-1M[b]	GRAAL	LEPS	HIγS[c]
Location	Frascati Italy	Brookhaven US	Novosibirsk Russia	Grenoble France	Harima Japan	Durham US
Storage ring	Adone	NSLS	VEPP-4M	ESRF	SPring-8	Duke-SR
Electron energy (GeV)	1.5	2.5–2.8	1.4–6.0	6	8	0.24–1.2
Laser energy (eV)	2.45	2.41–4.68	1.17–4.68	2.41–3.53	2.41–4.68	1.17–6.53
γ-beam energy (MeV)	5–80	110–450	100–1600	550–1500	1500–2400	1–100 (158)[d]
Energy selection	Internal tagging	External tagging	(Int or Ext?) tagging	Internal tagging	Internal tagging	Collimation
γ-energy resolution (FWHM)						
ΔE (MeV)	2–4	5	10–20	16	30	0.008–8.5
$\frac{\Delta E}{E}$ (%)	5	1.1	1–3	1.1	1.25	0.8–10
E-beam current (A)	0.1	0.2	0.1	0.2	0.1–0.2	0.01–0.1
Max on-target flux (γ/s)	5×10^5	5×10^6	10^6	3×10^6	5×10^6	10^4–5×10^8
Max total flux (γ/s)						10^6–3×10^9[e]
Years of operation	1978–1993	1987–2006	1993–	1995–	1998–	1996–

For performance of facilities other than HIγS, see review articles: (1) A. D'Angelo et al., Nuclear Instrum. Methods A **455**, 1 (2000); and (2) C. Schaerf, Physics Today, August 2005, 44 (2005).

[a] The LADON facility used both collimation and internal tagging. The tagging operation is listed.

[b] ROKK-1 (1982) and ROKK-2 (1987) are two older Compton gamma source facilities at Novosibirsk.

[c] HIγS has the highest flux performance between 5 and 20 MeV.

[d] HIγS covers the gamma energy range of 1–100 MeV by using commercially available FEL mirrors from 1064 to 190 nm. The planned vacuum ultraviolet (VUV) FEL mirror development will extend its operation up to about 158 MeV.

[e] The HIγS flux performance is expected to increase by at least one order of magnitude by 2010 with further development.

cross sections at several GeVs with a hydrogen bubble chamber. In 1978 the first γ-ray Compton light source facility for nuclear physics research, the Ladon project, was brought to operation in Frascati [8–12]. A higher γ-flux was produced by colliding the high intensity photon beam inside a laser cavity with the electron beam in the straight section of the 1.5 GeV ADONE storage ring at Frascati National Laboratories. This facility produced polarized γ-ray beams up to 80 MeV with an on-target flux of up to 5×10^5 s^{-1} for nuclear experiments. Following the success of the Ladon facility at Frascati, several new γ-ray Compton light source facilities were brought into operation, including LEGS [13] and HIγS [14] in the US, Graal in France [15], ROKK-1/ROKK-2/ROKK-1M in Russia [16–19], and LEPS in Japan [20,21]. The performance parameters of major Compton γ-source facilities around the world are summarized in Table 1. Reviews of Compton γ-ray beams and some of the listed facilities are found in [22–24].

Among these Compton gamma source facilities, the High Intensity Gamma-ray Source (HIγS) at Duke University is the first dedicated Compton γ-ray facility employing a high intensity Free-Electron Laser (FEL) as the photon driver. As a result, HIγS is a high intensity, nearly monochromatic, and highly polarized γ-ray source covering a wide range of energies from about 1–100 MeV, with a planned extension up to 150 MeV. With the completion of the recent accelerator and FEL upgrade, HIγS has demonstrated a new level of high intensity operation with a maximum total flux about 3×10^9 γ/s at 15 MeV, one or two orders of magnitude more powerful than any other Compton gamma source ever built and operated. The wide energy range and high flux performance of HIγS makes it a unique and superior γ-ray beam facility in the world, ideal for low and medium energy nuclear physics research.

This Review will begin with a brief overview of the fundamentals of γ-ray production via Compton scattering of photons from relativistic electrons. Following this, we will describe the upgraded HIγS facility, emphasizing its capabilities and performance characteristics. This section will conclude with a description of anticipated upgrades for the not too distant future.

We will then review the nuclear physics program which has been executed using this facility. We will also describe the research presently underway and some of the planned future studies. The first topic which we will describe will be several of the nuclear structure studies which have been completed. This work took advantage of the intense linearly polarized beams below 10 MeV which were used as a tool to perform nuclear resonance fluorescence (NRF) studies of dipole states in nuclei.

The next subject will be our present and planned photodisintegration studies of ^{3}He and ^{4}He. In addition to testing state-of-the-art theoretical predictions, it will be shown how the HIγS beams allow us to resolve several long-standing controversies involving few-body photodisintegration cross sections at low energies.

Another area of intense activity at HIγS is the work underway to study the primary nuclear reaction involved in oxygen formation in stellar helium burning. The experiment being developed will use an optical-time projection chamber to measure the $^{16}O(\gamma,\alpha)^{12}C$ reaction cross sections. This will provide us with cross sections for the inverse reaction $^{12}C(\alpha,\gamma)^{16}O$ at astrophysically relevant energies.

HIγS is uniquely suited to studies of the Gerasimov–Drell–Hearn (GDH) sum rule for d and ^{3}He below pion threshold. Preliminary results have been obtained in the case of the deuteron using data on the d(γ, n)p reaction taken with linearly polarized beams and unpolarized deuterium targets. These data make it possible for us to obtain an indirect determination of the GDH sum rule integrand at near-threshold energies. These same data also led to the first determination of the splittings of the three triplet p-wave amplitudes which are present in the case of E1 photodisintegration at energies near 15 MeV. This

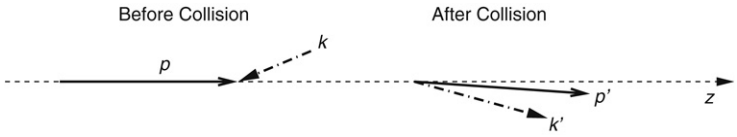

Fig. 1. Compton scattering of an electron and a photon.

is the first experimental measurement of these splittings. Our results are found to be in excellent agreement with theoretical predictions, especially when relativistic spin-orbit currents are taken into account. The real experiments on the GDH sum rule in d and ^{3}He, which are about to commence at HIγS, will utilize polarized targets and circularly polarized γ-ray beams. A detailed description of the experimental plans for this work will be presented.

Compton scattering experiments are a natural application of HIγS beams. A large collaboration has been working to develop a full program of study using polarized beams and polarized targets, designed to measure fundamental structure constants of the nucleons. The description of these experiments will show how HIγS will allow us to obtain precision measurements of the electric and the magnetic polarizabilities of both the proton and the neutron. We will also be able to measure the so-called spin polarizabilities of the nucleons, a set of theoretically predicted but unmeasured fundamental structure constants. The detailed experimental plans along with the accuracy of the anticipated results will be presented in this Review.

1.1. Theory of gamma-ray beam production

1.1.1. A brief review of the Compton scattering process

Compton scattering between an electron and a photon is shown in Fig. 1. We can list the four momenta of the electron and photon before and after collision as the following:

	Before collision	After collision
Electron	$p^i = (\mathcal{E}_e/c, \vec{p})$	$p'^i = (\mathcal{E}'_e/c, \vec{p'})$
Photon	$\hbar k^i = (\hbar\omega/c, \hbar\vec{k})$	$\hbar k'^i = (\hbar\omega'/c, \hbar\vec{k'})$

where $\mathcal{E}_e$ and $\vec{p}$ denote the energy and momentum of the electron and $\vec{k}$ is the wave number of the photon. Using conservation of four-momentum and for low-intensity electromagnetic waves, we can express the energy of the outgoing photon as:

$$E_\gamma \equiv \hbar\omega' = \frac{\hbar\omega(1-\beta\cos\theta_i)}{1-\beta\cos\theta_f + \frac{\hbar\omega}{\mathcal{E}_e}(1-\cos\theta_{ph})}, \tag{1}$$

where $\hbar$ is Planck's constant, $\hbar\omega$ is the energy of the incoming photon, E_γ ($\hbar\omega'$) is the energy of the outgoing photon, θ_i and θ_f are the angles between the momentum of the incoming and outgoing photons and that of the incident electron, ($\cos\theta_i = \hat{p}\cdot\hat{k}$ and $\cos\theta_f = \hat{p}\cdot\hat{k'}$), and θ_{ph} is the angle between two photons ($\cos\theta_{ph} = \hat{k}\cdot\hat{k'}$).

For a collision between relativistic electrons and low-energy photons, the energy of the scattered photons is peaked along the direction of the incident electrons. The scattered photon energy has a maximum value in a head-on collision with $\theta_i = \pi$ and $\theta_f = 0$,

$$\hbar\omega' = \frac{\gamma^2(1+\beta)^2}{1+R_0}\hbar\omega, \tag{2}$$

where γ is the Lorentz boost factor, $\beta = \frac{v}{c}$, and $R_0 = 2\gamma^2(1+\beta)\hbar\omega/\mathcal{E}_e$ is the recoil term. When the recoil is small ($R_0 \ll 1$), the maximum scattered photon energy is approximately, $\hbar\omega'_{\max} \approx \gamma^2(1+\beta)^2\hbar\omega \approx 4\gamma^2\hbar\omega$, where the second approximation holds for ultra-relativistic electrons with $\gamma \gg 1$. It is clear that the energy boost factor comes from two consequent Lorentz transformations between the laboratory frame and the electron-rest frame; each gives a boost of $\gamma(1+\beta)$.

The differential cross section of the Compton scattering process is well-known [25]. For example, the Compton cross section between an unpolarized electron and an unpolarized photon can be expressed for a given incident photon as

$$\mathrm{d}\sigma = 8\pi r_e^2\frac{\mathrm{d}y}{x^2}\left[\left(\frac{1}{x}-\frac{1}{y}\right)^2 + \left(\frac{1}{x}-\frac{1}{y}\right) + \frac{1}{4}\left(\frac{x}{y}+\frac{y}{x}\right)\right], \tag{3}$$

where $x = (s-m^2)/m^2$, $y = -(u-m^2)/m^2$, $s = (p+k)^2$, $t = (p-p')^2$, $u = (p-k')^2$, r_e is the classical electron radius, and Planck's constant and the speed of light are set to unity ($\hbar = 1, c = 1$). In the laboratory frame, x, y, and t are related to the known quantities,

$$x = \frac{2\gamma\hbar\omega(1-\beta\cos\theta_i)}{mc^2}, \qquad y = \frac{2\gamma\hbar\omega'(1-\beta\cos\theta_f)}{mc^2}, \qquad t = -\frac{2\hbar\omega\,\hbar\omega'(1-\cos\theta_{ph})}{c^2}.$$

The total cross section is given by

$$\sigma_{\rm tot} = \frac{2\pi r_e^2}{x}\left[\left(1-\frac{4}{x}-\frac{8}{x^2}\right)\ln(1+x)+\frac{1}{2}+\frac{8}{x}-\frac{1}{2(x+1)^2}\right]. \tag{4}$$

When $x \ll 1$ (i.e. the recoil is small), the total cross section is $\sigma_{\rm tot} \approx \sigma_0(1-x+\frac{13}{10}x^2)$, where $\sigma_0 = \frac{8\pi r_e^2}{3} = 6.652\times10^{-29}\ {\rm m}^2$ is the classical Thomson scattering cross section.

For the head-on collision of a relativistic electron beam and a low energy photon beam, scattered photons with the highest energy are peaked around the direction of the incident electron beam. In principle, this allows the formation of a nearly monochromatic Compton photon beam by using a simple collimation technique.

The differential cross-section of a polarized photon colliding with an unpolarized electron can be written in the center-of-mass frame or the laboratory frame for the head-on collision [25]:

$$\begin{aligned}
{\rm d}\sigma_p &= \frac{1}{2}{\rm d}\sigma + 2r_e^2\frac{{\rm d}y{\rm d}\phi}{x^2}\left\{(\xi_3+\xi_3')\left[-\left(\frac{1}{x}-\frac{1}{y}\right)^2-\left(\frac{1}{x}-\frac{1}{y}\right)\right]\right.\\
&\quad\left.+\ \xi_1\xi_1'\left(\frac{1}{x}-\frac{1}{y}+\frac{1}{2}\right)+\xi_2\xi_2'\frac{1}{4}\left(\frac{x}{y}+\frac{y}{x}\right)\left(1+\frac{2}{x}-\frac{2}{y}\right)+\xi_3\xi_3'\left[\left(\frac{1}{x}-\frac{1}{y}\right)^2+\left(\frac{1}{x}-\frac{1}{y}\right)+\frac{1}{2}\right]\right\}\\
&= 4r_e^2\frac{{\rm d}y{\rm d}\phi}{x^2}\left\{F_0+F_3(\xi_3+\xi_3')+F_{11}\xi_1\xi_1'+F_{22}\xi_2\xi_2'+F_{33}\xi_3\xi_3'\right\},
\end{aligned} \tag{5}$$

where ${\rm d}\sigma$ is the differential cross-section for an unpolarized photon, $\vec{\xi} = (\xi_1, \xi_2, \xi_3)$ and $\vec{\xi}' = (-\xi_1', -\xi_2', \xi_3')$ are the Stokes parameters [25] describing the degrees of polarization of incident and outgoing photons defined with respect to a fixed coordinate system, ϕ is the azimuthal angle of the scattering plane formed by the momenta of two photons with respect to the same coordinate system, and F_0, F_3, F_{11}, F_{22}, and F_{33} are cross-section contributions due to different polarization states of the photons. Clearly, for an incoming photon with a given polarization state, the cross-section depends on the polarization state of the outgoing photon.

Summing over all polarization states of the outgoing photon, the differential cross-section becomes

$$\begin{aligned}
{\rm d}\sigma_p &= {\rm d}\sigma - 4r_e^2\frac{{\rm d}y{\rm d}\phi}{x^2}\xi_3\left[\left(\frac{1}{x}-\frac{1}{y}\right)^2+\left(\frac{1}{x}-\frac{1}{y}\right)\right]\\
&= 4r_e^2\frac{{\rm d}y{\rm d}\phi}{x^2}\left\{(1-\xi_3)\left[\left(\frac{1}{x}-\frac{1}{y}\right)^2+\left(\frac{1}{x}-\frac{1}{y}\right)\right]+\frac{1}{4}\left(\frac{x}{y}+\frac{y}{x}\right)\right\}\\
&= 4r_e^2\frac{{\rm d}y{\rm d}\phi}{x^2}F,
\end{aligned} \tag{6}$$

where F is defined in the last part of the equation. For a polarized incoming photon, the outgoing photon is also polarized in general. The Stokes parameters of the outgoing photon, $\vec{\xi}^f$, can be calculated using

$$\xi_1^f = \frac{F_{11}}{F}\xi_1, \qquad \xi_2^f = \frac{F_{22}}{F}\xi_2, \qquad \xi_3^f = \frac{F_3+F_{33}\xi_3}{F}. \tag{7}$$

For the Compton γ-ray sources, if the incident low energy photon beam is polarized, the collimated outgoing γ-ray beam will also be polarized. The degree of polarization of the γ-ray beam depends on several factors, including the degree of polarization of the incident photon beam, the degree of collimation of the scattered photon beam, and the amount of recoil in the case of linear polarization. For HIγS, the reduction of linear polarization due to recoil is negligible. Furthermore, a nearly completely polarized FEL beam is used as the incident photon beam, with either horizontal or circular polarization. The finite opening angle of the γ-ray beam can contribute to the reduction of polarization of the HIγS beam. Nevertheless, this opening angle is very small since the collimator is located about 60 m away from the collision point. For the entire operation range of HIγS, the γ-ray beam can be collimated to achieve a very high degree of polarization, higher than 95% for both linear and circular polarization.

1.1.2. Compton γ-ray beam energy spectra

The γ-ray energy resolution is a critical parameter for nuclear physics research. Unlike Bremsstrahlung γ-ray beams, the γ-ray beams produced by Compton scattering have their photons concentrated in the high energy end of the spectrum. Exploring this extraordinary feature, a nearly monochromatic γ-beam can be produced by collimating the scattered photons.

The γ-beam energy resolution depends on the quality of the electron and photon beams. The most important factors include the energy spread and the angular spread of the electron beam, the energy spread of the photon beam, and the degree of collimation. Given the detailed knowledge of the electron and photon beam distributions, the γ-beam spectrum can be computed using either a Monte Carlo simulation code (such as CAIN [26]) or a numerical integration code such as the one developed at Duke [27]. This has been done routinely at the HIγS and the calculated spectra agree well with the measured spectra.

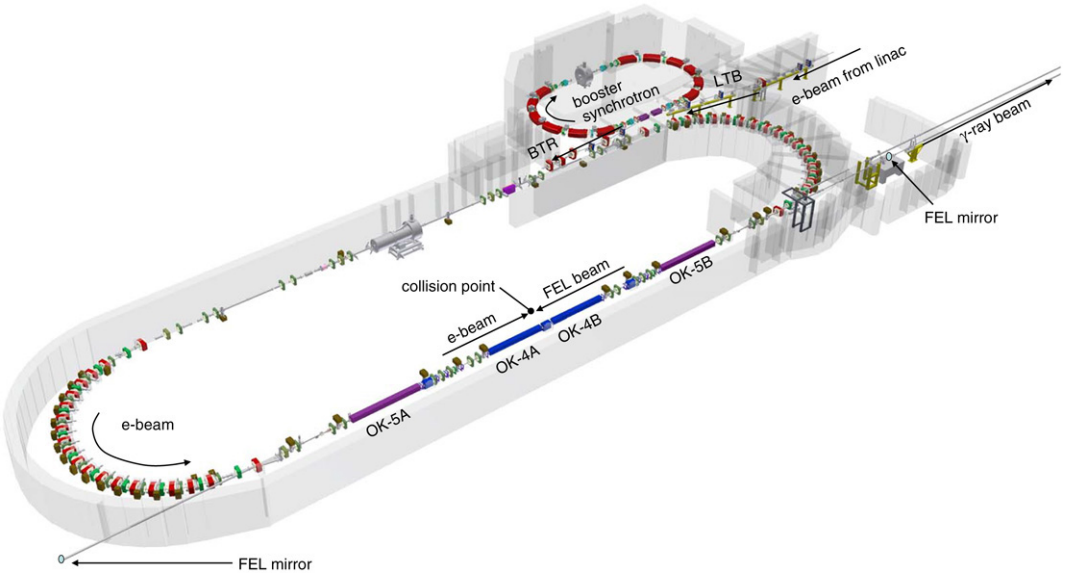

Fig. 2. The fully operational HIγS facility in 2007. Since 2004, the following upgrade projects have been completed: (1) a newly commissioned 0.24–1.2 GeV top-off booster synchrotron; (2) a new 34 m long storage ring straight section for hosting a HOM-damped RF cavity and for implementing a new injection scheme with the booster; and (3) the newly commissioned OK-5 FEL in the second 34 m long FEL straight section.

2. The HIγS facility

2.1. Overview of HIγS

The Duke Free-Electron Laser Laboratory (DFELL) operates storage ring based photon sources which are housed in a 65,000 square-foot facility located on the campus of Duke University in Durham, North Carolina, USA The accelerator facility layout is shown in Fig. 2. The 0.24–1.2 GeV electron storage ring is a dedicated driver for two types of light sources: (1) storage ring based ultraviolet (UV) and vacuum-ultraviolet (VUV) light sources, including UV–VUV free-electron lasers; and (2) a Compton γ source, the HIγS. The HIγS γ-ray beam is generated in the middle of a long straight section by colliding the electron beam with an FEL beam powered by the same electron beam.

The High Intensity Gamma-ray Source at Duke is a new generation Compton γ-ray source covering a wide range of beam energy with a great enhancement of γ-ray flux. Compared with the conventional Compton sources, HIγS is unique in two ways: (1) it uses the high intensity intra-cavity FEL beam as the photon source, and (2) it takes advantage of the low emittance and large energy acceptance of the modern storage ring. Because of this unique combination of electron and photon beams, HIγS has several important advantages including:

(1) the transverse alignment and time synchronization between the colliding electron and photon beams are realized automatically as the result of achieving the FEL lasing;
(2) γ beams with a small energy spread and a high flux can be delivered to the experimental areas by using a passive collimation system, without having to simultaneously measure the energy of the recoiling electrons (tagging);
(3) the selectable FEL wavelength allows HIγS to cover a wider range of beam energies than other Compton light sources driven by conventional lasers; and
(4) quasi-CW and pulsed modes of γ production can be realized with the same hardware system.

Since its first demonstration experiment in 1996 [14], the HIγS facility has undergone several major accelerator and FEL upgrades. The upgrades in recent years have been aimed at achieving the following three main goals, (1) to produce γ-ray beams with circular polarization; (2) to extend high-flux operation of HIγS above 20 MeV; and (3) to improve the γ-ray flux by more than one order of magnitude below 20 MeV. The fully upgraded HIγS facility was brought to operation in 2007 with its performance exceeding the design specifications for the upgrades [28]. This unique facility is now well positioned for a broad range of scientific applications.

In the following sections, we will first describe the accelerators and their recent upgrades, followed by a brief overview of the relevant FEL development. We will then give a detailed outline of the HIγS performance by discussing the γ-ray beam parameters and modes of operation. We will conclude this section with a discussion of future development plans for the HIγS facility.

Table 2
Main parameters of the booster synchrotron

Parameter	Value	Comments
Key design parameters		
Circumference (m)	31.902	
RF frequency (MHz)	178.55	
Number of RF bucket	19	
Natural emittance (ϵ_x, ϵ_y) (nm rad)	350, 15	
Betatron tune (ν_x, ν_y)	2.43, 0.46	
Present operation parameters		
Injection energy (GeV)	0.18–0.28	
Extraction energy (GeV)	0.18–1.2	
Cycle time (s)	1.3–2.5	Single bunch
Charge injected into storage ring (nC/s)	0.035–0.050	Single-bunch

2.2. Description of the accelerators and their recent upgrades

The DFELL accelerators include a 0.18–0.28 GeV linac pre-injector, a top-off, full-energy booster injector, and a 0.24–1.2 GeV electron storage ring. The storage ring is the driver for several FELs with various polarizations. In this section, we describe the status of these accelerators and their recent upgrades.

2.2.1. Linear accelerator

The electron beam is originated in a photo-cathode microwave electron gun. A high power nitrogen laser (0.4–0.5 mJ per pulse with a pulse duration of 0.5 ns) specially optimized for low time-jitter operation ($\leq$1 ns) is used as the photon source. The linac pre-injector consists of eleven S-band (2.856 GHz) linear accelerator sections and is typically operated at about 1 Hz. Before the development and construction of the booster synchrotron as the main injector, the linac was used as the primary injector to the storage ring. The electron beam energy was ramped up slowly in the storage ring for user operation.

2.2.2. Booster synchrotron as a top-off full-energy injector

Without a full energy injector, the performance of the storage ring based light sources, including HIγS, was severely limited. The main limitations came from two areas (1) a low single-bunch and multi-bunch beam current as limited by elevated beam instabilities at a low injection energy; (2) a low operation efficiency due to electron beam refill cycles and slow energy ramping in the storage ring. Without being able to continuously replace the lost electrons due to a large energy loss after Compton scattering, it was not practical to operate the HIγS in this so-called "electron-loss mode" with the γ-ray beam energy above 20 MeV. Furthermore, the low bunch current set a practical limit for the maximum flux possible for HIγS operation below 20 MeV. These problems could be solved by operating a full energy injector in the top-off mode. This injector would continuously refill the storage ring operated at a fixed energy. Furthermore, a higher operating energy of the storage ring would result in a higher beam current for high γ-ray flux production.

A proposal to upgrade the HIγS facility by constructing and operating a booster synchrotron as a full-energy, top-off injector for the storage ring was funded by the US Department of Energy in 2001. A full technical design of the booster synchrotron was completed and documented in a Technical Design Report [29] in 2004. The Budker Institute of Nuclear Physics (BINP), Russia was a major collaborator in developing this booster synchrotron. A large part of the booster hardware was built by the BINP. In addition, the BINP personnel participated in various stages of the booster development, from mechanical design, to hardware installation, to system integration and commissioning. The layout of the booster synchrotron is shown as part of Fig. 2. The main design and operating parameters are found in Table 2.

The development of the booster synchrotron faced challenges in several areas [30–41]. The first area of challenge arose from the compactness of the booster. Due to a rather limited project budget, a very compact synchrotron was designed with a circumference of 31.9 m but for a maximum extraction energy of 1.2 GeV. This led to several technical problems including (1) a high degree of magnet saturation when operating above 0.9 GeV; and (2) large shifts of betatron tunes and chromaticities during the energy ramp. The first problem was solved by employing a large number of (56) ramping power supplies to provide magnetic field compensation. The second problem was solved by developing a very sophisticated real-time control system with two operating modes, a "storage-ring mode" of operation for booster commissioning and an energy ramping mode for standard booster operation.

The second area of challenge was the requirement for rapid changes of the extraction energy in a wide energy range from the linac injection energy to a maximum energy of 1.2 GeV. This requirement stemmed from the need to change the γ-ray energy frequently while fixing the FEL wavelength. This challenge was met by building the magnetic field compensation deeply into the real-time processors of the booster control system using physics based controls, a novel method that was first developed for the storage ring control system at Duke [42]. By switching back and forth between the "storage-ring mode" and energy ramping mode, we would build up the ramping curve for magnetic power supplies step by step. Each step of the ramping curve represented a saved magnetic lattice instance which could be used for extraction.

Table 3
Main accelerator and beam parameters for the Duke storage ring in 2007

Accelerator/Beam parameters	Value	Comments
Operation energy	0.24–1.2 GeV	
Circumference	107.46 m	
Length of each straight section	34.21 m	
Length of each arc	19.52 m	
RF frequency	178.547 MHz	
Orbital revolution frequency	2.79 MHz	
Number of RF buckets	64	
Bunch modes		
One-bunch	FEL operation	
Two-bunch	HIγS operation	
Max beam currents		
One-bunch	95 mA	Achieved at $\geq$ 0.6 GeV
Two-bunch	$>$80 mA	Achieved at $\geq$ 0.3 GeV

The third area where we pushed the limit of the technology was the injection and extraction scheme. We had an unusual requirement of extracting any electron bunch from the booster and injecting it into any RF bucket in the storage ring, at a repetition rate of 25 Hz. To achieve this, the required extraction pulse length should be less than 11 ns. To reduce the requirement on the kicker strength, a vertical extraction (and injection) scheme was used to take advantage of a large vertical betatron function at the kicker ($\beta_y = 25$ m). The use of a single injection and a single extraction kicker also limited the operational betatron tunes of the magnetic lattice. Furthermore, the injection/extraction scheme required the use of a complex mixture of local and global orbit bumps. We met all of the above technical challenges and delivered an operational full-energy booster injector in 2007, meeting or exceeding all performance specifications. Since the spring of 2007, the booster injector has been operated reliably with top-off injection as the main mode of operation for all user programs.

2.2.3. Electron storage ring

The Duke electron storage ring is a two-and-one-half generation light source storage ring with a low emittance and a large energy aperture, dedicated to driving advanced light sources including free-electron lasers and Compton light sources [43–45]. The storage ring was first commissioned in 1994 with a maximum operation energy of 1.0 GeV. In 1996, the first FEL on the storage ring, the OK-4 FEL, was brought to operation. In the same year, operating in two-bunch mode the first nearly monochromatic γ-ray beam at 12.2 MeV was produced with close to 100% linear polarization by colliding the electron and OK-4 FEL beams inside the optical resonator [14].

The Duke storage ring has the shape of a race-track with two long straight sections, 34 m each, including an injection straight section to host the beam injection and RF system, and an FEL straight section dedicated to various configurations of FELs (see Fig. 2). The collision point for the photon and electron beams is located around the center of the FEL straight section in a magnetic field-free region. The storage ring is typically operated with a single-bunch beam in the FEL mode, a two-bunch beam for the γ-ray production, and a multi-bunch beam to generate spontaneous radiation from the wiggler and dipole magnets.

Parallel to the booster development, several major hardware upgrades were carried out on and around the Duke storage ring [46]. First, we installed a new higher-order mode (HOM) damped RF cavity system developed by the BINP on the storage ring, freeing up the old RF cavity for the booster synchrotron. Second, we completely overhauled the magnetic lattice of one of the straight sections to host a new injection scheme for the booster injector. Third, we greatly improved the radiation shielding around the first arc after the collision point in order to enable high flux operation in the "electron-loss mode".

One of the unique features of the Duke storage ring is its wide range of operating energies, from 0.24 to 1.2 GeV, an energy variation of a factor of five. For γ-ray production, this translates into a factor of 25 in the γ-ray energy range for a fixed FEL wavelength. Unlike other storage rings, changing the beam energy in the Duke storage ring can be done easily and rapidly; the storage ring is routinely operated at multiple energies in a day. This flexibility is realized using a state-of-the-art real-time control system which allows direct controls of magnetic optics parameters in physical units [42]. This control system provided for an energy-independent operation of the storage ring.

We summarize the main accelerator and beam parameters of the Duke storage ring in Table 3. The operation of the booster injector has greatly increased the capabilities of the storage ring in two aspects. The first one is associated with a higher beam current available for user operation. By injecting at a higher energy, the increased synchrotron radiation damping has helped to suppress beam instability. As a result, a much higher single-bunch current can be realized. For example, when operating above 600 MeV with FEL lasing, more than 95 mA of beam current can be stored in a single bunch, more than three times the maximum current that we reached with direct linac injection at a lower energy. For HIγS operation, we now routinely operate a two-bunch beam with a total current of 60–80 mA, with its maximum operating current limited not by the capability of the storage ring, but by the stability of the FEL mirrors due to FEL power loading. In short, with the booster injector, the performance of HIγS is no longer accelerator limited (or beam current limited), but rather FEL mirror limited. The second area of benefits is a much improved operating efficiency.

Table 4
Parameters of the FEL systems and electron beam for γ-beam production

	OK-4 FEL	OK-5 FEL
Polarization	Horizontal	Circular/Linear
FEL wigglers		
No. of wigglers	2	4 (2 installed)
No. of regular periods	33	30
Wiggler periods (m)	0.10	0.12
Wiggler gap (mm)	25	40 × 40
Max. magnetic field (T) (at 3 kA)	0.536	0.286
FEL resonator cavity		Same as OK-4 FEL
Length (m)	53.73	
Rayleigh range (m)	4.44–5.52	
Wavelength (nm)	1064–190[a]	
Optical beam size ($\sigma = \sqrt{\frac{\lambda Z_R}{4\pi}}$) (mm)	0.61–0.68 at 1064 nm 0.26–0.29 at 190 nm	
Round-trip loss (%)	0.3–2	
Electron beam at collision point		Same as OK-4 FEL
Horizontal beam size ($\sigma_x = \sqrt{\epsilon_x \beta_x}$) (mm)	0.14–0.40	
Vertical beam size ($\sigma_y = \sqrt{\epsilon_y \beta_y}$) (mm)	0.02–0.07	
Horizontal angular spread ($\sigma'_x = \sqrt{\epsilon_x / \beta_x}$) (mrad)	0.035–0.10	
Vertical angular spread ($\sigma'_x = \sqrt{\epsilon_y / \beta_y}$) (mrad)	0.006–0.02	

The OK-4 FEL and OK-5 FEL use different types of wigglers, the OK-4 and OK-5 wigglers, respectively. Both types of wigglers are electromagnetic.
[a] Multi-layer dielectric mirrors with high reflectivity are available commercially in this wavelength range.

Even though the booster was initially envisioned to enable γ-ray production in the "electron-loss mode", today top-off operation is used for all user research programs. The beam lifetime is no longer an issue as long as the experiments can tolerate occasional disruptions associated with injection. For HIγS operation below 20 MeV, the top-off injection has greatly enhanced the operation efficiency, effectively increasing the flux by a factor of two to four, compared with the pre-upgrade operation.

2.3. FEL development in recent years

The first FEL on the Duke storage ring is the OK-4 FEL [47–50], an FEL with horizontal polarization. The OK-4 FEL is an optical klystron (OK) FEL which consists of two OK-4 type planar electromagnetic wiggler magnets, sandwiching a buncher magnet. The FEL beam is accumulated inside a long optical resonator of 53.7 m, half the circumference of the storage ring. First brought into operation in 1996, the OK-4 FEL was the work horse for the first phase of the γ-ray applications between 1996 and 2005 [51,52]. The full potential of HIγS was not fully realized with the OK-4 FEL due to the lack of a full-energy injector for the storage ring as described above. Another limitation is the lack of circular polarization which requires helical wigglers.

A set of four helical electromagnetic wigglers, named the OK-5 wigglers, were developed for producing circularly polarized γ-ray beams [53–55]. The main parameters of the OK-4 and OK-5 wigglers, as well as parameters of the FEL cavity are summarized in Table 4. If all four OK-5 wigglers with a total length of 16 m would be used together in a single FEL, a substantial increase of the FEL gain could be realized. This would allow us to extend FEL operation into the VUV region below 190 nm. However, this long FEL would greatly reduce the performance of the storage ring when operated at a low electron beam energy due to significant degradation of electron beam dynamics [56,57]. This adverse effect on beam dynamics due to strong nonlinear fields of the OK-5 wigglers was recognized around 2003, following substantial computer simulation. This led to a new path to develop a circularly polarized FEL.

To manage the risk associated with operating the OK-5 wigglers and to keep the main light source, the OK-4 FEL, operational during the upgrade, we developed a three-phase upgrade plan to bring the OK-5 system into operation. In the first phase, the magnetic lattice for OK-5 wigglers was installed and commissioned with the electron beam. In the second phase, two of four OK-5 wigglers were installed and their impact on beam dynamics studied. The last phase would install the remaining two OK-5 wigglers (planned for 2008). This strategy worked quite well for us. In 2005, we brought the two-wiggler OK-5 FEL into operation, producing circularly polarized FEL and γ-ray beams [58,59]. This system preserves the linear polarization capability by keeping the OK-4 FEL in the upgraded storage ring. By having two complete FEL systems in the same straight section, we can produce both linearly and circularly polarized γ-ray beams from the same accelerator and deliver them to the same target room. The flexibility of this arrangement has greatly enhanced the capability of the HIγS.

2.4. HIγS performance and γ-ray beam parameters

In this section, we will first describe various operating modes of HIγS and then discuss the γ-ray beam parameters which are now available for the nuclear physics research with the present configuration of the accelerators.

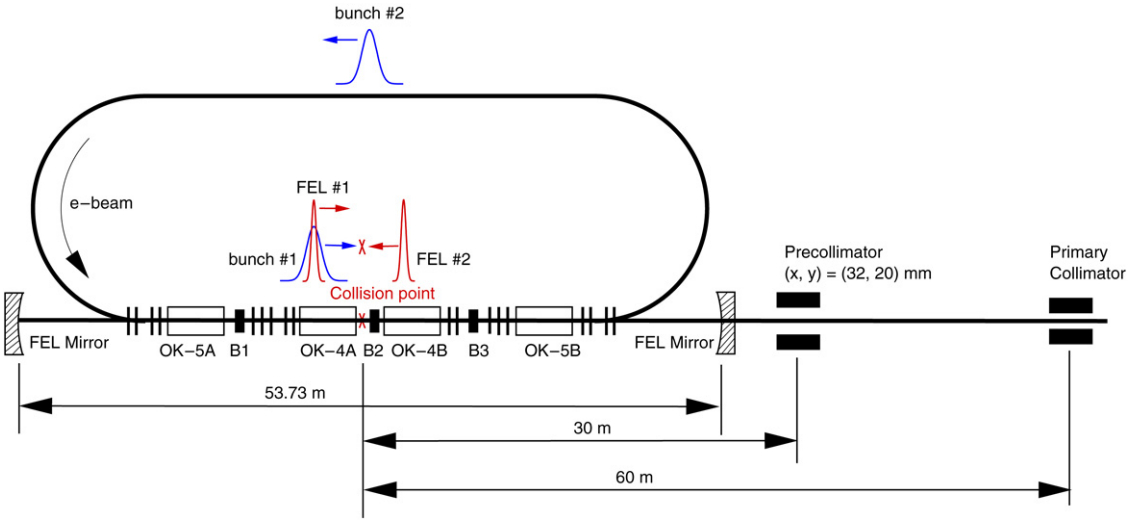

Fig. 3. The schematic of the HIγS operation with two electron beam bunches colliding with the FEL pulses in the center of the FEL resonator cavity.

2.4.1. HIγS operating modes

High intensity γ-ray beams are produced by colliding the FEL and electron beams in the FEL straight section as shown in Fig. 3. Like any colliding accelerator, the HIγS operation requires a minimum of two beams. In the symmetric two-bunch mode of operating, two out of sixty-four RF buckets are filled with beams separated by one half of the storage ring circumference. The photons in one FEL pulse generated by one electron bunch collide with the electrons in the other bunch, resulting in a continuous sequence of γ-ray bursts with a repetition rate of 5.58 MHz, twice the revolution frequency of the electron beam. Other electron bunch patterns can also be used to generate γ-ray beams. However, the symmetric two-bunch mode is the most effective way to achieve a high γ-ray flux when the maximum flux is not limited by the maximum current in a single bunch.

The operation of HIγS can be tailored to the special needs of various research programs. The γ-ray beam can be generated either in a quasi continuous-wave (CW) mode or in a pulsed mode; the HIγS can also be operated in the high-flux mode or in a high-resolution mode. Collectively, there are four possible operating modes obtained by mixing the requirements of the pulse structure and flux/energy-resolution. The quasi-CW, high-flux mode is the dominant mode of operation for most nuclear physics experiments. In this section, we will focus on the pulsed and high resolution modes of operation.

The pulsed mode of operation is desirable for suppressing various backgrounds during experiments by taking data only in the time window when the γ-ray beam is present [60]. The γ-ray beam pulsing is realized by pulsing the FEL beam using a device called an FEL gain modulator [61] which allows repeated, but very brief photon–electron interactions to build up the FEL beam. In this pulsed mode, the γ-ray beam is generated with micro- and macro-pulse structures. The macropulse with tens to hundreds of microsecond durations are repeated at a rate ranging from a few Hz to about 20 Hz. Within a macropulse, the micropulses are separated by about 179 ns as in the quasi-CW mode. The pulsed mode operation requires more frequent injection due to a much reduced electron beam lifetime and typically has a reduced flux. When optimized, the average γ-ray flux in the pulsed mode can be as high as 30%–50% of that in the quasi-CW operation.

In the high-flux mode, two RF buckets are filled with roughly the same amount of charge. The minimal γ-ray beam energy spread which can be achieved by collimation is determined mainly by the energy spread and angular spread of the electron beam. For example, below 20 MeV, the induced energy spread of the electron beam due to its interaction in the FEL is the dominant factor in determining the energy resolution of the γ-ray beam. Below 20 MeV, in the high-flux mode, the achievable full-width energy resolution of the collimated γ-ray beam is about 2.5%–3.5%, depending on the flux level.

For some nuclear physics experiments, higher resolution is required. Examples include the study of narrow nuclear resonances. An energy resolution better than 1% can be achieved in a special mode of operation using two electron bunches with substantially different amounts of charge. The γ-ray beam is then produced mainly by colliding the FEL beam of the high-charge bunch with electrons in the low-charge bunch. Great care is required to prevent the low-charge bunch from reaching FEL lasing. In this high-resolution mode, the typical γ-ray flux is more than one-order of magnitude lower than in the high-flux mode. In many circumstances, this flux compromise is acceptable because of the benefits which come with a higher energy-resolution.

2.4.2. HIγS performance

The upgraded HIγS facility has demonstrated a very high level of performance which has met and, in many cases, exceeded the performance specifications promised to the funding agency [62]. In this section, we will describe the γ-ray beam parameters and HIγS performance with a focus on the high-flux, quasi-CW mode of operation.

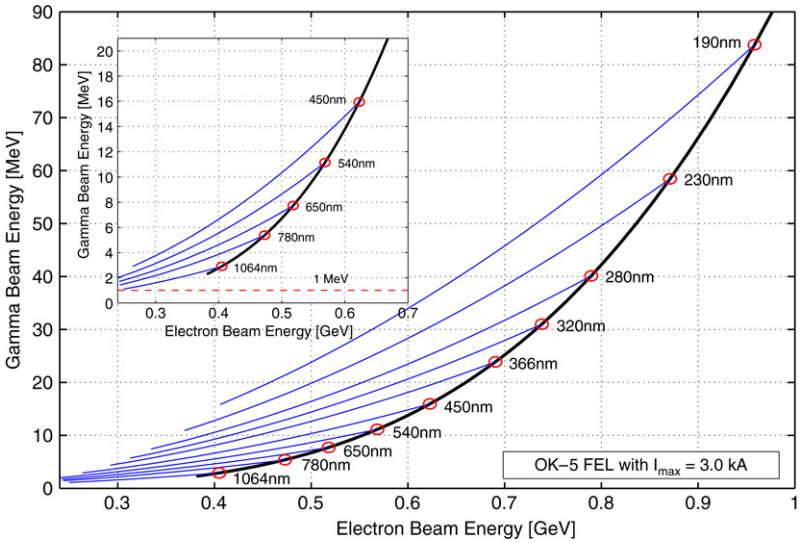

Fig. 4. The energy tuning range of the circularly polarized γ-ray beam with the OK-5 FEL and a number of FEL mirror sets. For a given FEL wavelength, the highest flux is achieved along the thick black curve which is determined by the maximum electron beam energy as limited by the maximum wiggler field. The inset shows more details of the γ-ray energy coverage below 16 MeV.

Table 5
Parameters of high-flux, quasi CW HIγS operation

Parameter	Value	Comments
E-beam configuration	Symmetric two-bunch beam	
E-beam current (mA)	10–80	In two bunches
γ-ray energy, E_γ (MeV)		
With mirrors 1064 to 190 nm	1–84	Available with existing hardware
With 156 nm mirror	85–158	Require FEL and mirror development
Total flux (γ/s)		
(a) No-loss mode ($\leq$20 MeV)		
E_γ = 1–3 MeV	5×10^7–5×10^8 [a]	
E_γ = 3–5 MeV	5×10^8–1×10^9	
E_γ = 5–10 MeV	1×10^9–2×10^9	
E_γ = 10–20 MeV	2×10^9–3×10^9	
(b) Loss mode (>20 MeV)		
E_γ = 21–60 MeV	$>2 \times 10^8$ [b]	
E_γ = 61–84 MeV	$>1 \times 10^8$ [b]	190 nm mirror
E_γ = 85–158 MeV	$>1 \times 10^8$ [c]	156 nm mirror
Linear and circular polarization	>95%	Depending on collimator size

[a] High flux horizontally polarized γ-ray beams can be produced by the OK-4 FEL. The circularly polarized γ-ray flux is low due to the dynamic impact of OK-5 wigglers.
[b] The flux is currently limited by the capability of sustaining a high intracavity power by the FEL mirrors.
[c] Radiation resistive FEL mirrors at 156 nm need to be developed and the FEL wigglers need to be powered at 4000 A.

The high γ-ray flux mode requires the use of high reflectivity FEL cavity mirrors which are typically dielectric multilayer mirrors. These mirrors have a narrow wavelength bandwidth of a few percent. For a given mirror set, the FEL can be operated with a range of electron beam energies. To maximize γ-ray flux, we have devised a plan to use a series of FEL mirrors covering a wide wavelength spectrum. Fig. 4 shows our scheme to tune the γ-ray beam energy using a set of commercially available high-reflectivity mirrors from 1024 to 190 nm. While plotted for the circular polarization with the OK-5 FEL, these curves also apply to the linear polarization with the OK-4 FEL. When tuning the γ-ray energy, switching to an appropriate mirror wavelength can increase the γ-ray flux. For example, a set of 780 nm mirrors has been used to produce γ-ray beams between 1.65 and 5.4 MeV. A higher flux can be realized at and below 3.0 MeV if a set of 1064 nm mirrors with a similar reflectivity are used.

The HIγS γ-ray performance is summarized in Table 5. With the present hardware configuration (as of February 2008), the HIγS can produce γ-ray beams from 1 MeV to 85 MeV using commercial mirrors. With 190 nm mirrors, the maximum γ-ray energy can be extended to about 100 MeV by upgrading the maximum operation current of the FEL wigglers from 3.0 kA to 3.6 kA. The minimal γ-ray energy is limited by the electron beam instability at a low operating energy. In

principle, operation below 1.0 MeV is possible but with a reduced γ-ray flux. While no longer limited by the capability of the accelerators, the γ-ray flux of the HIγS is determined by other practical factors, in particular the performance of the FEL mirrors.

Below 20 MeV in the so-called "no-loss mode", the Compton scattering does not cause any significant additional loss of electrons due to the small energy transfer to the γ photons. In this regime, the maximum γ-flux is limited by the maximum intracavity power that the FEL mirrors can sustain without significant surface deformation. This has limited the maximum two-bunch current to about 60–80 mA for user experiments. Using FEL mirrors with reflectivity better than 99.7%, the total flux is on the order of a few times 10^9 γ/s between 5 MeV and 20 MeV and an order of magnitude less between 1 MeV and 3 MeV (see Table 5). The on-target flux depends on the size of the collimator. For example, at 10 MeV with a collimator selecting a 3% energy resolution, the on-target flux is about 10^8 γ/s.

Above 20 MeV in the so-called "electron-loss mode", because of additional electron beam loss due to a large energy transfer to γ photons, the γ-flux in principle will be limited by the charge replacement rate, i.e. the storage ring injection rate. However, due to a more intense wiggler radiation, the FEL mirror deformation occurs earlier with a lower beam current (as low as 30 mA in two bunches). This has practically limited the total γ flux above 20 MeV to about 1–2 $\times$ 10^8 γ/s, independent of the injection rate. In addition, we have observed a significant reduction of UV FEL mirror lifetime due to radiation damage caused by intense harmonic synchrotron radiation from the wigglers. This problem will have to be dealt with effectively in order to extend the mirror lifetime.

With both OK-4 and OK-5 FELs in place, user programs have the choice of either linear or circular polarizations. A high degree of polarization can be realized (typically >95%); the degree of polarization will be reduced with less collimation. While not commonly used, switching between linear and circular polarizations can be accomplished in a few minutes. Switching between left- and right-circular polarization is also possible. At the present time, this is done manually and it takes about 20 min. In the future, this switch will be carried out using a solid-state switch to reverse the direction of the DC current to the wigglers. With this device, the circular polarization switch can be carried out in a few minutes, possibly in less than 60 s.

2.5. Future upgrades

At the present time, the High Intensity Gamma-ray Source at Duke is the most powerful Compton γ-ray source in the world. Its performance can be further improved with a modest investment in hardware development and upgrades in the coming years. With these upgrades, we expect to increase the γ-ray flux by a factor of ten or more below 20 MeV and by a factor of five or more above 20 MeV. We also plan to extend HIγS operation towards the pion-threshold energy of around 150 MeV. In this section, we discuss both the near-term and long-term upgrades for HIγS.

2.5.1. Near-term upgrades

In the next three years, we plan to carry out a series of upgrades to further improve the performance of HIγS. The first area of upgrades focuses on improving the FEL resonator, which includes the following developments: (1) to stabilize the FEL mirror temperature via better cooling; (2) to improve the FEL mirror lifetime by developing water cooled apertures to reduce harmonic wiggler radiation on the mirrors; (3) to increase the intracavity FEL power with higher reflectivity mirrors; and (4) to optimize the optical beam size at the collision point. Compared with the accelerator upgrades in recent years, these developments are relatively small scale and can be carried out incrementally with a very limited impact on daily operations. These developments will allow us to increase the γ-flux by at least one order of magnitude for gamma operation below 20 MeV. Above 20 MeV in the "electron-loss mode", these developments will significantly improve the stability of γ-beam operations while reducing the frequency of mirror changes due to a longer lifetime for UV mirrors.

The near-term accelerator upgrades have three different goals; all of them are related to operating above 20 MeV. The first upgrade is aimed at extending the maximum energy of the γ-ray beam from 85 to 100 MeV by upgrading the wiggler power supply and bussbar system to raise the maximum operating current from 3.0 to 3.6 kA. The second upgrade is aimed at increasing the charge injection rate into the storage ring to about 100 pC/s, which will then allow γ-beam production above 20 MeV to reach a total flux of 10^9 γ/s. The third upgrade is to complete the installation of two additional OK-5 wigglers in the middle of the FEL straight section while retaining the two-wiggler OK-4 FEL using a magnetic optics switchyard system. This arrangement preserves the linear polarization capability of the OK-4 FEL for low energy γ production. It also allows us to develop a new FEL with four OK-5 wigglers. This FEL with a very high FEL gain, is essential for VUV FEL operations below 190 nm, a critical development for HIγS to be able to produce γ-beams at and above the pion-threshold energy.

2.5.2. Long-term development

In the long term, our greatest challenges are to extend the HIγS operation above the pion-threshold energy of about 150 MeV. In the original HIγS proposal, it was assumed that FEL lasing around 100 nm would be realized in the near future. Today, a decade later, the shortest FEL lasing using an optical resonator stands at around 190 nm; the mirror damage problem due to intense VUV radiation remains unsolved. Recognizing this problem in 2003, we decided to focus on developing durable FEL mirrors with a wavelength around 150 nm via a close collaboration with industrial partners.

Without having an FEL operating at a very short wavelength (such as 100 nm), the γ-beam operation around 150 MeV poses several technical challenges. For example, using commercially available 190 nm mirrors, a 1.3 GeV electron beam is needed to produce 150 MeV γ-ray beams. In this scenario, we face two hardware limitations. First, the Duke storage ring was initially designed for 1.0 GeV operation. With an extensive temperature monitoring system, we have successfully pushed its maximum operating energy to 1.2 GeV with highly saturated magnets. Operating at 1.3 GeV will require a major upgrade of the storage ring magnet system. Effectively, this requires building a new storage ring. Second, the OK-5 wigglers were not designed to operate with a field high enough for 190 nm FEL operation with a 1.3 GeV electron beam. In turn, this will require a new set of FEL wigglers. In principle, if we have an adequate budget, all these technical problems can be solved.

Since 2003, we have been searching for a cost-effective solution. One possibility is based upon the assumption that 150 nm radiation-resistant FEL mirrors can be developed in the next few years. This will allow us to produce a 158 MeV γ-ray beam with a 1.2 GeV electron beam and a 150 nm FEL beam. This scenario requires operating the OK-5 wigglers well above their design specifications. This necessitates a major upgrade of the OK-5 power system. In sum, the progress in the mirror technology and the available budget will ultimately determine our upgrade path toward operating at 150 MeV in the future.

3. Nuclear structure @ HIγS

3.1. Nuclear resonance fluorescence

Nuclear structure studies @ HIγS have utilized the technique of nuclear resonance fluorescence (NRF) (See Ref. [63] for an earlier review of this and other aspects of the HIγS research program). The nearly mono-energetic intense 100% linearly polarized γ-ray beams @ HIγS are ideal for such investigations. It has been demonstrated that the HIγS beams do, in fact, make NRF studies possible at a new level of precision and efficiency [64].

The intensity distribution function of a $0^+ \rightarrow 1^\pi_1 \rightarrow 0^+$ photon scattering reaction can be derived using the angular correlation formalism [64]. If $W(\theta, \phi)$ represents the yield at polar angle θ, and ϕ is the azimuthal angle of the reacton plane with respect to the polarization plane of the incident γ-ray beam, then the analyzing power Σ is given by

$$\Sigma = \frac{W(90°, 0°) - W(90°, 90°)}{W(90°, 0°) + W(90°, 90°)} = \pi_1 = \begin{cases} +1 & J^\pi = 1^+ \\ -1 & J^\pi = 1^-. \end{cases} \tag{8}$$

Therefore, the parities of dipole excitations in a 0^+ ground state nucleus can be sensitively measured using detectors at $\theta = 90°$ and $\phi = 0°$ and 90°, respectively.

3.1.1. Dipole excitations in ^{138}Ba, ^{88}Sr, ^{92}Zr, and ^{94}Mo

The first NRF experiment performed at HIγS was on the nucleus ^{138}Ba [64]. A typical set of raw spectra obtained at $\overline{E}_\gamma = 5.62$ MeV is shown in Fig. 5. The measured analyzing powers of 18 dipole states were all found to be ~ -0.83, indicating that all of the observed states were electric dipole $J^\pi = 1^-$ states. A previously proposed strong 1^+(M1) state at 5.644 MeV was shown to be in fact a 1^-(E1) state. The fact that the observed analyzing power was somewhat less than the theoretical value of -1.0 was accounted for by a simulation which took the finite geometry of the target and detectors into account [64].

Following this initial demonstration of the potency of the HIγS beam in performing NRF measurements, the HIγS beam was used to study dipole excitations in ^{88}Sr, ^{92}Zr and ^{96}Mo. In the case of ^{88}Sr a previous experiment which used a Compton polarimeter and an unpolarized bremsstrahlung beam found evidence that the state at E = 4.742 MeV was of M1 character. It was suggested that this state might indicate the existence of a dynamical scissors mode in the semi-magic nucleus ^{88}Sr. Such a state could have properties similar to those of the mixed-symmetry two-phonon 1^+ state in ^{94}Mo.

The state at 4.742 MeV was determined to be an E1 (1^-) state in the HIγS experiment [65]. This assignment makes it very likely that it is the $J^\pi = 1^-$ member of the quadrupole–octupole coupled (QOC) two-phonon multiplet. This is surprising because the energy of this state is significantly larger than the two-phonon sum energy $E_{2^+\otimes 3^-} = 4.570$ MeV. This is unlike the results of a systematic survey which demonstrated that the 1^- member of the multiplet occurs at an energy which is a few percent below the sum energy in most nuclei [66]. This excess positive energy of the 4.742 MeV state implies that the energy anharmonicity

$$e = \frac{E(1^-) - (E(2^+_1) + E(3^-_1))}{E(2^+_1) + E(3^-_1)} \tag{9}$$

of this two-phonon 1^- state is positive, a fact which remains to be explained.

The unambiguous $J^\pi = 1^+$ assignment to the 3472 keV state in ^{90}Zr confirms the interpretation that this state is the dominant fragment of the low-energy M1 excitation strength distribution in this nucleus [67]. And the $J^\pi = 1^-$ assignment to the 3638 keV state makes it tempting to interpret it as a fragment of the QOC two-phonon state. However, this seems very unlikely since the total energy of the 2^+_1 and 3^-_1 states is only 3274 keV, which leads to an energy anharmonicity of $e = +0.111$, almost three times larger than the already atypical positive value of $e = +0.038$ previously observed in ^{88}Sr.

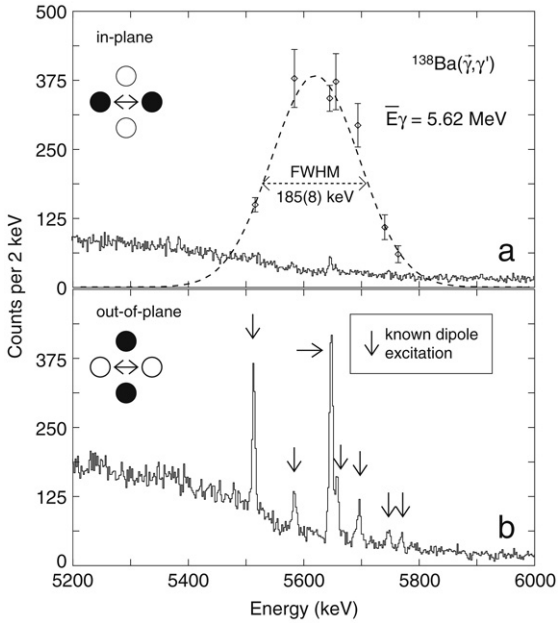

Fig. 5. γ-ray spectra from NRF studies on ^{nat}Ba target as published in [64]. The detectors were placed at a polar angle of 90° (a) in the polarization plane of the incident γ-rays, and (b) perpendicular to the plane of polarization. The arrows mark the known dipole states in ^{138}Ba. The dashed curve in (a) is obtained using an error-weighted fit to the known peak heights and represents the γ-ray intensity plotted in arbitrary units (from Ref. [64]).

The 1^+(M1) states found in ^{96}Mo were at 2794.5, 3300.1 and 3424.8 keV, respectively. Previous measurements were used to determine that the total M1 excitation strength of these three states is

$$\Sigma B(M1; 0_1^+ \rightarrow 1_{1,2,3}^+) = 0.47(2)\mu_N^2. \tag{10}$$

This strength is comparable to the summed M1 excitation strength found in ^{94}Mo ($0.67(7)\mu_N^2$) around 3.2 MeV. The M1 excitations in ^{94}Mo have been described as being the two-phonon 1^+ mixed-symmetry states resulting from the coupling of the one-phonon symmetric and mixed-symmetry quadrupole excitations of the ground state [68]. On the basis of the similarity in the location and magnitude of the strengths, the 1^+ states observed in ^{96}Mo were interpreted as fragments of the 1^+ member of the mixed-symmetry two-phonon multiplet of that nucleus.

1^- states were found at 3600 and 3895 keV in ^{96}Mo. As in the case of ^{92}Zr, these state are much higher in energy than the sum of the 2_1^+ and 3_1^- states, which is 3012 keV. This, along with the fact that no decay transitions to the 3_1^+ state were observed, makes it extremely unlikely that these 1^- states are harmonic QOC two phonon fragments.

3.1.2. Branching ratios and parities of states in rare-earth nuclei

A study on ^{172}Yb and ^{174}Yb determined the parity of six dipole states between 2.9 and 3.6 MeV [69]. These results were combined with additional data from previous NRF experiments on ^{150}Nd [70], ^{160}Gd [71], ^{162,164}Dy [72], ^{166,168,170}Er [73] and ^{176}Hf [74] in order to perform a systematic survey of the relationship between γ-decay branching ratios and parity quantum numbers for these rare-earth nuclei. Since we are dealing with well-deformed nuclei, the K-quantum number is expected to be good. For deformed even–even nuclei, the K-quantum number of $J = 1$ states can be assigned within the validity of the Alaga rules [75] from the electromagnetic decay branching ratios:

$$R = \frac{B(1_K^\pi \rightarrow 2_1^+)}{B(1_K^\pi \rightarrow 0_1^+)} = \begin{cases} 2 & K = 0 \\ 0.5 & K = 1. \end{cases} \tag{11}$$

The interacting boson model with s- and d-proton and neutron bosons indicates that all 1^+ levels have a branching ratio corresponding to $K = 1$. This suggests that states with $J = 1$ and $R = 2$ have negative parity. It has also been assumed in previous works that $R = 0.5$ ($K = 1$) implied positive parity. The results of the present study are summarized in Fig. 6, where it is seen that all states with $R_{exp} > 1$ have negative parity. It must be noted, however, that the parities are known almost exclusively for the strongest excitations. Therefore, the correlation between branching ratio and parity shown in Fig. 6 may not be observed for weaker excitations.

3.1.3. M1 strength in ^{40}Ar

Our final example of NRF@HIγS is the study of the spin-flip strength in ^{40}Ar [76]. The ground state of the ^{40}Ar nucleus has two-proton holes in the sd-shell and two-neutron particles in the $f_{\frac{7}{2}}$-shell relative to the $N = Z = 20$ shell closure of

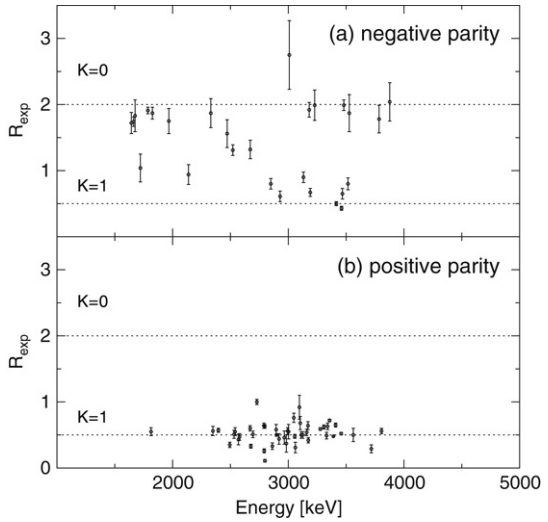

Fig. 6. Measured branching ratios R_{exp} for dipole states in different rare earth nuclei with negative parity (a) and positive parity (b), as published in [69]. All states with $R_{exp} > 1$ have negative parity. The dashed line indicate the value of R predicted by the Alaga rules (Eq. (11)).

^{40}Ca. Therefore, information on the level structure of ^{40}Ar can yield insight into the 2p–2h residual interactions which are important for understanding many nuclei including exotic neutron-rich ones.

The HIγS facility was used to scan the energy region between 7.7 and 11 MeV. All of the 28 dipole states observed were found to be E1 (1^-) except for one state at $E_x = 9.757$ MeV. This state contributes an M1 strength of B(M1) $\uparrow = 0.148(59)\ \mu_N^2$ in ^{40}Ar, and is the first observed 1^+ state in ^{40}Ar.

Shell model calculations were carried out using Nowacki's interaction in which ten valence protons are in the sd-shell and two valence neutrons are in the $f_{\frac{7}{2}}$–$p_{\frac{3}{2}}$ space [77]. The results predicted that a 1^+ state at 6.882 MeV contains the largest contribution to B(M1)$\uparrow$. The second largest contribution was predicted to arise from a state at 9.465 MeV with B(M1)$\uparrow = 0.105\ \mu_N^2$, dominated by the $\pi(d_{\frac{5}{2}} \rightarrow d_{\frac{3}{2}})$ spin-flip transition. The observed 1^+ state at E_x = 9.757 MeV was therefore identified as one fragment of the $d_{\frac{5}{2}} \rightarrow d_{\frac{3}{2}}$ spin-flip transition in ^{40}Ar. A summary of the comparison of theory and experiment is presented in Fig. 7.

This result constitutes the first evidence for spin-flip M1 strength in ^{40}Ar. Clearly, a future search for the predicted spin-flip strength at 6.882 MeV is essential.

3.1.4. Future prospects for NRF@HIγS

Additional studies are either being analyzed, in progress, or being planned. For example, various aspects of mixed-symmetry states are being addressed through studies in ^{164}Dy. And studies in the Pb isotopes are investigating the possibility of torodial modes of excitation by studying the coupling of strong E1 excitations of ^{208}Pb to single-particle wavefunctions having a different number of radial nodes. In ^{207}Pb, for example, coupling of the $\nu(3p_{\frac{1}{2}}^{-1})$ neutron hole to a collective 1^- state of the ^{208}Pb core results in a doublet of states with spin and parity quantum numbers $J^\pi = \frac{1}{2}^+$ and $\frac{3}{2}^+$. Preliminary results indicate that these states have been identified at 5.597 and 5.490 MeV, respectively. Studies are also underway to map out the E1 (1^-) strength in the isotopes ^{112}Sn and ^{124}Sn in the energy region expected to contain the Pygmy Dipole Resonance strength. A total of 72 dipole states have been observed to date, with all but one being E1 (1^-). Clearly, there is a bright and an important future for NRF studies@HIγS.

4. Low-energy electromagnetic few-nucleon physics

The three-nucleon and four-nucleon systems provide a natural laboratory for testing our understanding of the nuclear Hamiltonian. In particular, the study of electromagnetic processes gives information on electromagnetic currents, which can not be obtained by investigating pure hadronic processes. The electromagnetic currents are closely related to the underlying nuclear forces via the continuum equation. While pairwise interactions create two-body meson-exchange currents, three-nucleon force terms in the nuclear Hamiltonian lead to three-body contributions to the electromagnetic current.

Although calculational techniques for few-nucleon systems studied with electromagnetic probes are highly developed and reasonably successful in describing experimental data, a consistent treatment of nuclear interactions and currents is difficult to accomplish. However, there is promise that Chiral Perturbation Theory will provide the theoretical framework needed to treat electromagnetic nuclear processes in a rigorous and consistent way.

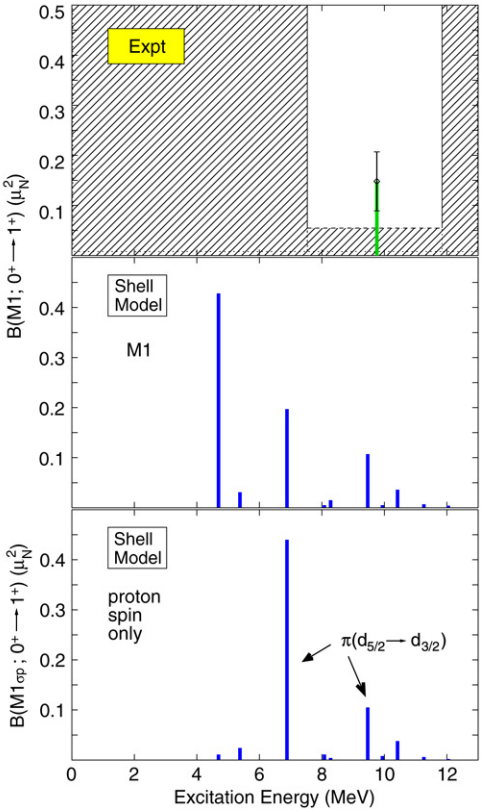

Fig. 7. (top) The 1st state observed in this work at 9.757 MeV and published in [69]. The white rectangle indicates the region investigated. (middle) M1 states from shell-model calculation. (bottom) Proton spin contributions only.

4.1. γ-^{3}He interactions

4.1.1. Two-body photodisintegration of ^{3}He

According to recent rigorous calculations performed by the Krakow group [78] using the Faddeev approach, and by the Trento group [79] using the Lorentz integral transform method, the angle integrated cross section for the two-body breakup reaction

$$\gamma + {}^3\mathrm{He} = \mathrm{p} + \mathrm{d} \quad (Q = -5.49\ \mathrm{MeV})$$

is sensitive to three-nucleon force (3NF) effects in the γ-ray energy range from 8 to 15 MeV. For example, at the cross section maximum near 10 MeV, the inclusion of the Urbana IX 3NF [80] lowers the total cross section by about 5% compared to calculations using only the nucleon–nucleon (NN) potential model Av18 [81]. Very recently, the Lisbon group [82,83] confirmed this conclusion and, in addition, showed that the Coulomb interaction in the exit channel has an even larger effect, reducing the cross section by about 8%.

Contrary to the significant progress made in the theoretical treatment of this reaction, the situation on the experimental side remains controversial. The existing experimental data can be grouped into two bands which are separated by about 40% in the region of the cross section maximum (see for example [84]), while the theoretical calculations split the difference between the two bands [83]. Interestingly, the two data points obtained very recently by Naito et al. [84] at $E_\gamma = 10.2$ and 16 MeV using the monoenergetic γ-ray beam produced at the National Institute of Advanced Industrial Science and Technology (AIST) in Tsukuba, Japan [86] via Nd-YLF laser-Compton backscattering clearly favors the lower band.

Initial experiments at HIγS focused on the 8–16 MeV energy range.

A high-pressure ^{3}He gas scintillator was used as target and detector. The gas was contained in a 0.1 cm thick stainless-steel cylinder of 5 cm diameter with a spherical end cap and total length of 10 cm. A 1 cm thick glass window allowed the scintillation light produced by the charged particles from the breakup of ^{3}He to be viewed by a 2 in. photomultiplier tube. A thin layer of MgO was deposited on the inside wall of the container and a wavelength shifter was evaporated on both the MgO layer and the inside of the glass window. The long axis of the scintillator housing was oriented perpendicular to the incoming γ-ray beam which had a diameter of 0.95 cm and an energy spread of about 2%. Fig. 8 shows pulse-height spectra from the breakup of ^{3}He at $E_\gamma = 10.0$, 12.5, and 15 MeV.

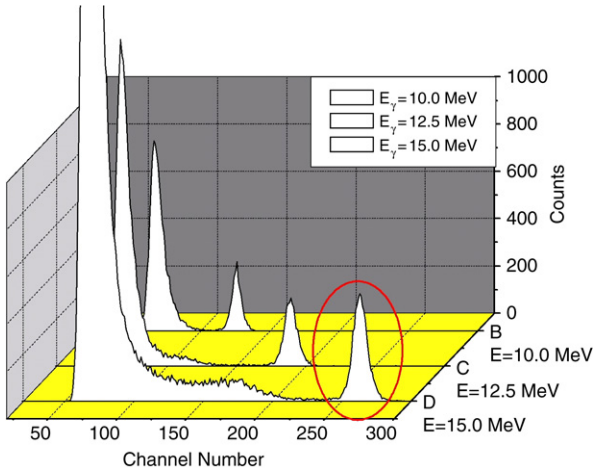

Fig. 8. Pulse-height spectra obtained with a high-pressure ^{3}He–Xe gas scintillator bombarded with 10.0, 12.5, and 15.0 MeV γ rays. See text for details.

At each energy the separated peak to the right (encircled in Fig. 8 for $E = 15$ MeV) is the sum of the proton and deuteron pulse heights resulting from the two-body breakup of ^{3}He. In addition, at $E_\gamma = 15$ MeV pulses produced by the two protons from the three-body breakup of ^{3}He are clearly visible between channel numbers 100 and 200. However, at lower channel numbers the spectra are dominated by pulses from recoil electrons generated by Compton scattering of the intense incident γ-ray beam. In order to reduce the range of the charged particles, especially those of the protons in the scintillator, it was necessary to add an appreciable amount of Xe (up to 30%) to the 35 atm of ^{3}He gas, resulting not only in an increased sensitivity to Compton scattering in the gas, but also in an increase of the pulse height produced by recoil electrons. In principle, for measurements with $E_\gamma < 20$ MeV the ^{3}He gas in the scintillator could be replaced by ^{4}He gas to determine and subtract events due to recoil electrons. However, we have not yet used this procedure to measure the cross section for the three-body breakup of ^{3}He. Contributions of γ-ray induced events in the xenon admixture above channel number 100 are extremely small as was verified with ^{4}He–Xe and pure Xe gas scintillators.

In order to deduce the two-body breakup cross section of ^{3}He from the spectra shown in Fig. 8, the incident γ-ray flux has to be known accurately. This is a non-trivial task due to the very high incident γ-ray flux. Currently, three different methods are being investigated at HIγS:

- Small angle Compton scattering from a copper plate located at 0° into a HPGe detector whose angular position can be automatically adjusted between 0° and 30° to optimize the detector rate and counting statistics. The copper plate and the HPGe detector are positioned downstream of the experimental setup. This technique provides for continuous monitoring of the incident γ-ray flux.
- Using accurately calibrated attenuators which can be automatically inserted into the γ-ray beam to measure the reduced flux at 0-deg directly with a high efficient and calibrated NaI or BGO detector. This detector can be automatically moved into the beam, while at the same time the γ-ray flux is monitored with the standard plastic scintillator paddle arrangement located in the collimator hut just outside of the HIγS target room. Once the attenuators and detector are taking out of the beam, the γ-ray flux for the actual cross-section measurements is then obtained from the counts registered with the plastic scintillator paddle. The precision attenuators made of copper are located about 30 m upstream from the HIγS target room just behind the FEL east mirror.
- Using the same scheme as in (b), but with the NaI or BGO detector replaced by a cylindrical array of ^{3}He filled proportional counters and with a deuterated target at its center. The cross section for photodisintegration of deuterium is known to 2% accuracy. The neutrons from the γ-ray induced deuteron breakup are moderated and detected in the calibrated ^{3}He detector array. The efficiency of this detector array has been determined with a calibrated ^{252}Cf neutron source. For not too high γ-ray fluxes or at low γ-ray energies the detector array can stay in the beam and serve as a continuous γ-ray monitor.

Once the two-body breakup cross section of ^{3}He has been measured to satisfactory accuracy at HIγS, we plan to use high-pressure ^{3}He–Xe gas scintillators positioned downstream of the experimental setup as alternative in-beam monitors for γ-ray energies between 7 and 30 MeV.

4.1.2. Three-body photodisintegration of ^{3}He

The measurement of the photon analyzing power $\Sigma(\theta_n, E_n)$ in the γ-ray induced breakup of ^{3}He was chosen as a pioneering study of low-energy few-body ($A > 2$) physics with polarized γ-ray beams at HIγS. In contrast to the cross section, the theoretical predictions for $\Sigma(\theta_n, E_n)$ are insensitive to both meson-exchange and three-nucleon force effects [78, 83]. In addition, as stated already in Section 4.1.1, the Lisbon group [82,83] has recently succeeded in incorporating the

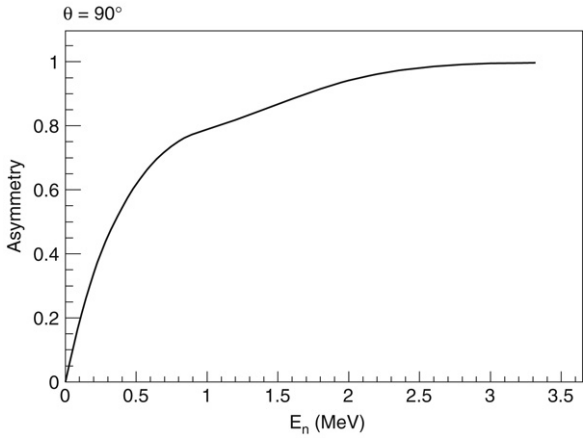

Fig. 9. Calculated photon analyzing power $\Sigma(90°, E_n)$ for the three-body breakup of ^{3}He at $E_\gamma = 12.8$ MeV. The calculations are from Deltuva [83] and employ the CD-Bonn nucleon–nucleon potential model [85] and include meson-exchange, Δ-isobar excitation, and Coulomb effects.

Coulomb interaction in their rigorous calculations. The reliability of the calculations for $\Sigma(\theta_n, E_n)$ allows the corresponding experiments to serve as a study of the systematics of our newly implemented techniques. Only with all systematic effects under control can we move on to more complicated observables in the $A = 3$ and $A = 4$ few-nucleon systems.

Fig. 9 shows a calculation of the Lisbon group [83] for the photon analyzing power of the three-body breakup of ^{3}He at 12.8 MeV and neutron emission angle $\theta_n = 90°$ (lab). As can be seen, the analyzing power approaches the magnitude of 1.0 for the highest neutron energies and then drops off for lower neutron energies. In order to compare experimental data for this observable to theoretical predictions, accurate data are needed as a function of neutron energy. The most straightforward method is to determine the neutron energy from a neutron time-of-flight (TOF) measurement. Of course, this method requires a sufficiently good TOF resolution in order to avoid long neutron flight paths. The low neutron energies involved with 12.8 MeV incident γ rays reduce the constraint on the time resolution somewhat. However, the change in time resolution of the detector and associated electronics as a function of detector pulse height must be known as well. The photon analyzing power $\Sigma(\theta_n, E_n)$ for the kinematically incomplete reaction

$$\gamma + {}^3\mathrm{He} = \mathrm{n} + \mathrm{p} + \mathrm{p} \quad (Q = -7.72\ \mathrm{MeV})$$

can be determined from the measured asymmetry obtained with incident linearly polarized γ rays of polarization $P_\gamma = 1.0$ located in the horizontal plane:

$$\Sigma\,(\theta_n, E_n) = \frac{\sigma\,(\theta_n, \phi_n = 0°(180°), E_n) - \sigma\,(\theta_n, \phi_n = 90°(270°), E_n)}{\sigma\,(\theta_n, \phi_n = 0°(180°), E_n) + \sigma\,(\theta_n, \phi_n = 90°(270°), E_n)}, \tag{12}$$

where $\sigma(\theta_n, \phi_n, E_n)$ is the yield of neutrons of energy E_n detected at polar angle θ_n and azimuthal angle ϕ_n.

In the following we describe two different experimental approaches for measuring $\Sigma(\theta_n, E_n)$.

- Photon Analyzing Power of ^{3}He at $E_\gamma = 12.8$ MeV and $\theta_n = 49.5°$–$157.5°$ (lab).
  The 12.8 MeV γ rays were produced via Compton backscattering of 2.7 eV FEL photons from 562 MeV electrons in the DFELL storage ring Free-Electron Laser. A 2.54 cm diameter and 91.4 cm long collimator made of aluminum was used to form the γ-ray beam for the actual ^{3}He asymmetry measurements, resulting in about 10^7 γ/s on target with an energy spread $\Delta E/E$ of about 3%. Lead shielding was placed after the collimator to remove γ rays that Compton scattered from the collimator. A HPGe detector positioned at 0° relative to the incident γ-ray beam was used to determine the γ-ray energy and its associated energy spread. In order to not overload the HPGe detector a relatively low γ-ray flux and small collimator (1.0 cm diameter) were used for these diagnostic measurements.

  The target consisted of a bottle filled with 170 atm of ^{3}He. The bottle was made of aluminum alloy 6082 with approximate length of 22.7 cm and 5.6 cm outer diameter, and wall thickness of 0.5 cm. An aluminum gas bottle was used as target vessel instead of steel, because it contains a negligible amount of ^{57}Fe. A target bottle made of steel would have resulted in an overwhelming neutron background, because at 12.8 MeV the γ-n cross section on ^{57}Fe is about 9 times larger than that on ^{3}He. However, the valve on the bottle was made of steel, precluding the target bottle from being mounted coaxially with the incident γ-ray beam. Instead, it was mounted with its long axis making a polar angle of 61.5° with the beam axis, resulting in an effective ^{3}He target length of 6.5 cm. Typically, the target bottle was mounted at an azimuthal angle of $\Phi = 0°$ with respect to the plane of the γ-ray polarization. To account for systematic errors induced by the asymmetric mounting of the target, the bottle was periodically rotated to an azimuthal angle of 90°, and measurements were also done for azimuthal angles of 45° and 225°.

  Neutrons produced in the photodisintegration of ^{3}He were detected using the Blowfish neutron detector array [87] (see also Fig. 23). This detector array consists of 88 BC-505 liquid scintillator detectors located on the surface of a sphere

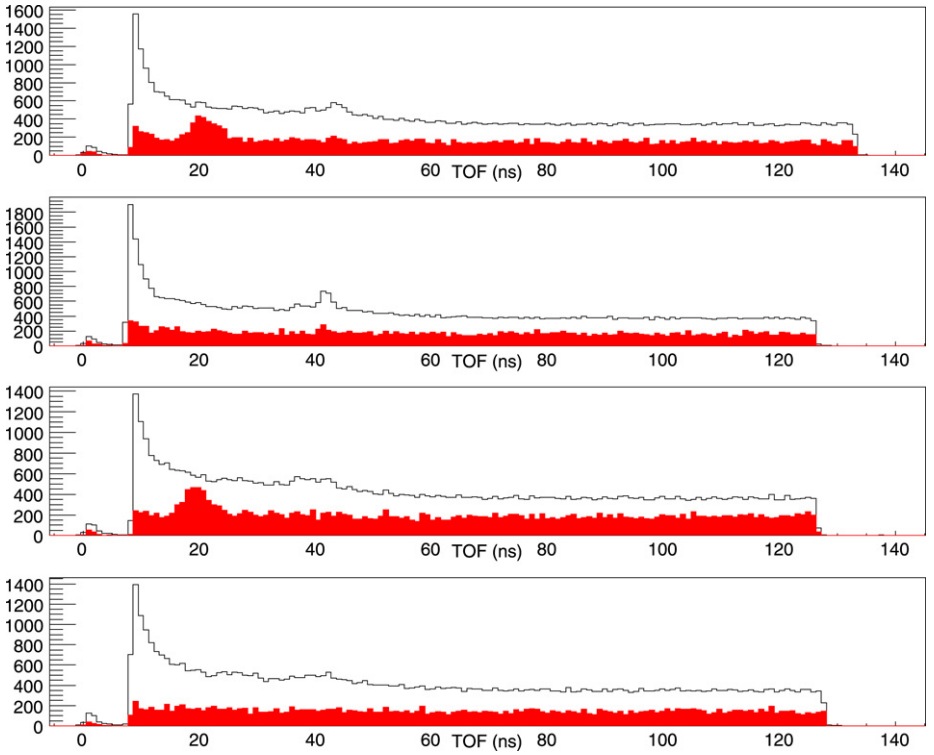

Fig. 10. Neutron time-of-flight spectra for the three-body breakup of ^{3}He at $E_\gamma = 12.8$ MeV and $\theta_n = 90$ (lab). See text for details.

with 40.6 cm radius centered on the target in 8 arcs uniformly covering the azimuthal angular range from 0° to 180°. The 11 detectors on each arc are uniformly positioned between polar angles of 22.5° and 157.5°. To reduce dead time, most of the detectors located at azimuthal angles of $\phi = 45°$, 135°, 225°, and 315° were turned off for the present experiment. In addition, all detectors located at the polar angles $\theta = 22.5°$ and 36.0° were turned off due to substantial beam-related background at these very forward angles. Gamma-ray induced signals (caused mainly by Compton scattering of the incident γ-ray beam from the wall of the target bottle) in the neutron detectors were greatly reduced due to the excellent pulse-shape-discrimination (PSD) properties of BC-505. The pulsed nature of the HIγS γ-ray beam (pulse every 179 ns) is ideal for neutron time-time-of-flight (TOF) measurements. Fig. 10 shows typical neutron TOF spectra. Here the start signal was obtained from the electron beam pick-off signal in the electron storage ring while the stop signal was derived from the neutron detectors. Time increases from left to right. Fig. 10 shows the ToF spectra for the detectors mounted at 90°. From the top to bottom, each subfigure shows the detectors mounted at beam left, up, right, and down. The black curves are the ToF histograms before any cuts have been applied, and the filled histrograms are with the PSD and pulse-height cuts applied, scaled up by a factor of 25.

The analysis of these data is underway. In order to convert the TOF spectra obtained for each individual neutron detector with its fairly short flight path of about 44 cm to neutron energy spectra, the time response of the detector-electronic system must be known very well. The goal is to obtain the photon analyzing power $\Sigma(\theta_n, E_n)$ as a function of neutron energy for the present 9 neutron detector angle settings ranging from 49.5 to 157.5 in the laboratory system. In addition, efforts are underway to explore whether relative cross-section data can be obtained in a reliable way from the present data.

- Photon Analyzing Power of ^{3}He at $E_n = 15.0$ MeV and $\theta_n = 90°$ (lab)

In practice, the experimental approach described above for measuring the photon analyzing power of ^{3}He is limited to incident γ-ray energies below the neutron production threshold of the material(s) containing the high-pressure ^{3}He gas. Above this energy the neutrons produced in the container wall will overwhelm the signal of interest. Even difference measurements with gas in and gas out will not yield accurate results.

In order to extend $\Sigma(\theta_n, E_n)$ measurements to higher γ-ray energies the passive high-pressure ^{3}He cell described in the previous section was replaced by an active high-pressure ^{3}He–Xe gas scintillator filled with 48.3 atm of ^{3}He and 2.7 atm of Xe. The long axis of the scintillator housing (see Section 4.1.1 for details) was oriented perpendicular to the γ-ray beam at an azimuthal angle of 45°.

The Blowfish detector array provides a maximum neutron flight path of about 43 cm. If the TOF technique is used for determining the neutron energies, a longer flight path is needed for higher neutron energies than those produced with 12.8 MeV incident γ rays. Therefore, we used the *Big Wheel* detector array (see Fig. 11) which can be configured to

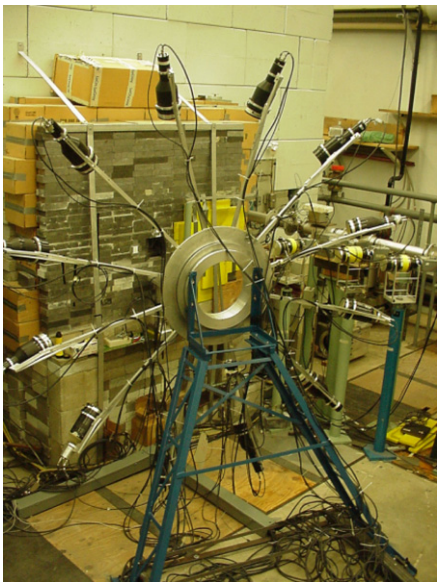

Fig. 11. *Big Wheel* neutron detector array. In contrast to this figure, the present experiment utilizes four neutron detectors at a polar angle of 90° and azimuthal angles of 0° and 180° (horizontal plane), and 90° and 270° (perpendicular to horizontal plane), respectively.

support up to 12 neutron detectors with a maximum flight path of 150 cm in the polar angular range from 15° to 165° and covering all azimuthal angles of interest.

For our initial study four liquid scintillator neutron detectors were installed at a center-to-center distance of 41.5 cm from the ^{3}He gas scintillator. These detectors, each 5 in. in diameter and 2 in. thick, were positioned at a polar angle of $\theta_n = 90°$ and azimuthal angles of $\phi_n = 0°$, 90°, 180°, and 270°, respectively, in the laboratory system. Instrumental asymmetries were canceled by rotating the setup by $+/-90°$ azimuthally (with the ^{3}He scintillator kept fixed in space). An identical scintillator cell filled with ^{4}He–Xe rather than with ^{3}He–Xe was used for purposes of measuring background.

The experiment was conducted using a 15 MeV γ-ray beam with 3% energy spread, 100% linearly polarized in the horizontal plane, and produced by Compton backscattering of 441.5 nm FEL photons from 600 MeV electrons, with an average flux of 6×10^6 $\gamma/(\text{cm}^2\ \text{s})$. The diameter of the γ-ray beam was 3 cm.

Neutron time-of-flight was measured using a start signal from the ^{3}He gas scintillator and a stop signal from the neutron detectors; both TOF and pulse height of the signal from the two protons produced in the gas scintillator were recorded in two-dimensional arrays and can be used in determining the analyzing power. TOF spectra (Fig. 12) were obtained by projecting the events in the two-dimensional display of TOF versus pulse height in the gas scintillator onto the TOF axis. The peaks centered around channel 225 are due to the neutrons of interest. Note the very different vertical scales for the detectors positioned in the horizontal plane (top panel of Fig. 12) and vertical plane (bottom panel). Due to the excellent PSD characteristics of our neutron detectors the TOF spectra are virtually free of Compton scattered γ-ray events. The counts to the right of channel 250 seen in the lower panel of Fig. 12 are due to neutrons scattered from the materials surrounding the ^{3}He gas. The measured value for $\Sigma(90°)$, obtained from the TOF spectra, integrated over all neutron energies above 1.23 MeV, is 0.946 ± 0.003 (stat.) with an estimated systematic uncertainty of 0.01. The main contribution to the systematic uncertainty comes from uncertainties in the precise value of the neutron detector energy thresholds and the choice of technique for background subtraction. The background itself was very small ($<1\%$). The result obtained in this work is in excellent agreement with the theoretical prediction for this quantity, found to be $\Sigma(90°) = 0.949$ by applying Monte-Carlo simulations of the experimental setup to point-geometry predictions [83] calculated with the Argonne v18 nucleon–nucleon potential model [81]. It should be noted that the differential cross section $\sigma(E_n, 90°)$ is about a factor of 5 higher at the highest neutron energy ($E_n = 4.8$ MeV) than at the lowest neutron energy detectable in the experiment ($E_n = 1.23$ MeV) lending the higher energy neutrons greater weight when calculating the analyzing power averaged over energy, hence the high value for this observable. The TOF spectra were deconvoluted into four equally wide neutron energy bins and $\Sigma(90°)$ obtained by this method is shown in Fig. 13 in comparison to the theoretical prediction.

The solid curve in Fig. 13 was calculated with the CD-Bonn nucleon–nucleon potential [88] with Δ-isobar excitation (to account for three-nucleon force effects) and the Coulomb interaction taken into account, while the nearly identical dashed curve is the result of using only the nucleon–nucleon potential model Av18 in the three-nucleon calculations [83]. These curves were calculated assuming a point-geometry experiment. Finally, the dotted curve represents the result when the finite geometry of our experimental setup is taken into account via a Monte-Carlo simulation. Clearly, the data obtained from the TOF spectra are in very good agreement with the theoretical prediction.

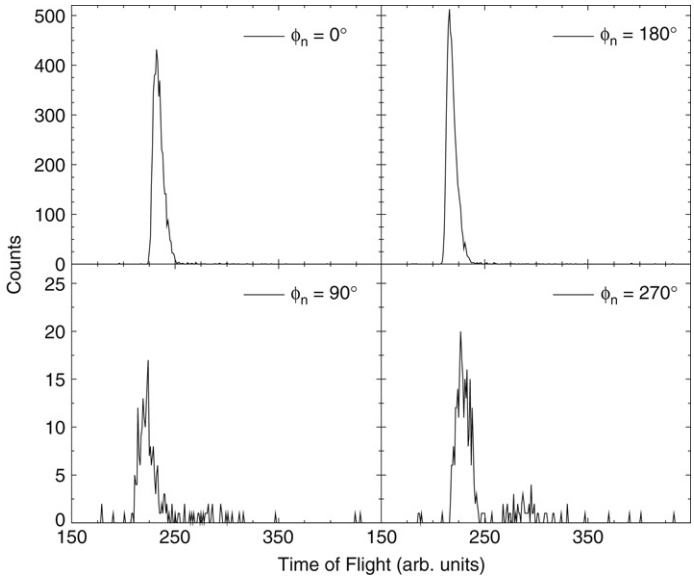

Fig. 12. Neutron time-of-flight spectra for the three-body breakup of ^{3}He at $E_\gamma = 15.0$ MeV and $\theta_n = 90°$ (lab). See text for details.

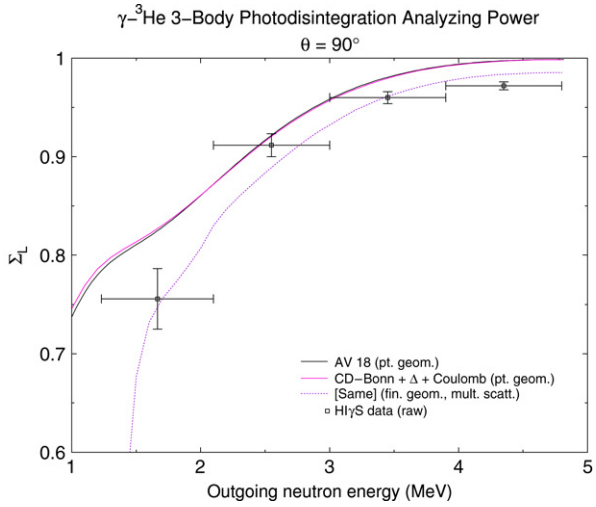

Fig. 13. Experimental data for the photon analyzing power $\Sigma(90°, E_n)$ of the three-body breakup of ^{3}He obtained from TOF spectra in comparison to theoretical predictions of Deltuva [83] at $E_\gamma = 15$ MeV.

A more detailed comparison of our data with theoretical predictions can be achieved by using the measured proton pulse-height distributions rather than the TOF spectra which were accumulated with a rather short flight path. The spectra shown in Fig. 14 were obtained by projecting the two-dimensional array of TOF versus proton pulse height in the gas scintillator onto the pulse-height axis.

The determination of the energy calibration and the energy-dependent energy resolution of the gas scintillator are currently being pursued in auxiliary experiments with neutron beams. In addition, the spectra shown in Fig. 14 are slightly distorted because some of the protons strike in inner wall of the gas cell before depositing their full energy in the gas volume. As a result, the measured energy distribution contains smaller pulse heights and must be corrected for this range effect. Efforts are currently underway to correct for this effect using detailed cross-section information provided by Deltuva [83]. Subsequently, we will deconvolute the energy spectra in order to determine $\Sigma(90, E_n)$ in smaller neutron energy steps than obtained with the associated TOF spectra.

4.2. γ-^{4}He interactions

For many reasons the ^{4}He nucleus is often considered as the link between the classical few-body systems, i.e., deuteron, triton and ^{3}He, and more complex nuclei. For example, one expects 3NF effects to be more important in the four-nucleon system than in the three-nucleon system.

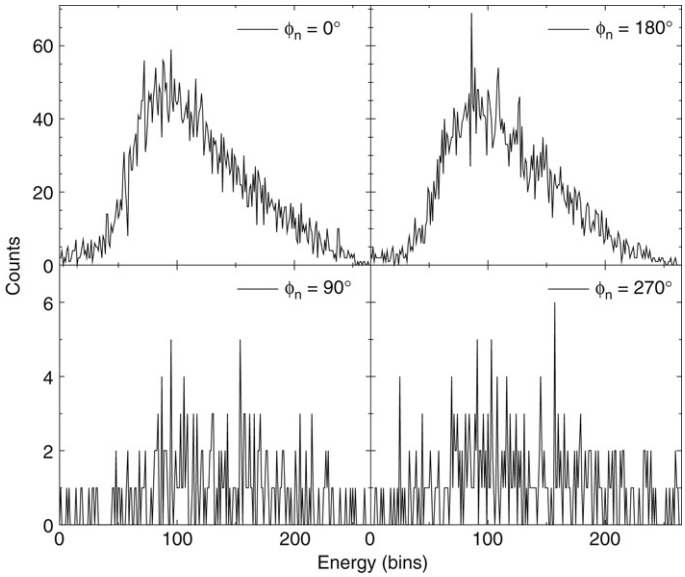

Fig. 14. Proton pulse-height spectra for the three-body breakup of ^{3}He at $E_\gamma = 15.0$ MeV and $\theta_n = 90°$ (lab). See text for details.

In the former one has six nucleon pairs and four triplets compared to three pairs and just one triplet in the latter. In addition, the higher density of ^{4}He might enhance the importance of 3NF effects. On the other hand and quite understandable, the theoretical treatment of the photodisintegration of ^{4}He is not yet as advanced as that of ^{3}He. Only very recently it became possible to calculate the total photoabsorption cross section of ^{4}He with a realistic nucleon–nucleon potential (Av18) and a 3NF (Urbana IX) using the Lorentz integral transform method of the Trento group [89]. The calculations reproduce the strong giant dipole peak, but they provide only a 6% reduction of the cross section in this energy regime once the 3NF is turned on. This is a surprising result, because the same calculations yield a 35% enhancement of the total photoabsorption cross section at pion threshold. This result is twice as large as obtained with Av18 and the Urbana IX 3NF for the total photoabsorption cross section of ^{3}He and ^{3}H. In the energy region of the giant dipole resonance near $E_\gamma = 26$ MeV the calculations are in very good agreement with the data of Nilsson et al. [90] and Wells et al. [91].

However, the experimental situation is still as controversial as it was about 25 years ago. The recent data of Shima et al. are about a factor of two lower than those of Nilsson et al. and Wells et al., while at $E_\gamma = 26$ MeV the data of Berman et al. [92] and Feldman et al. split the difference between those of Nilssen et al. and Shima et al. For a review article of all the experimental data prior to 1983 see [93]. More recent information is given in [94–96].

The photodisintegration reaction channels and their Q-values are:

$$\gamma + {}^4\mathrm{He} = {}^3\mathrm{H} + \mathrm{p} \quad (Q = -19.81\ \mathrm{MeV})$$
$$\gamma + {}^4\mathrm{He} = {}^3\mathrm{He} + \mathrm{n} \quad (Q = -20.58\ \mathrm{MeV})$$
$$\gamma + {}^4\mathrm{He} = \mathrm{d} + \mathrm{d} \quad (Q = -23.85\ \mathrm{MeV})$$
$$\gamma + {}^4\mathrm{He} = \mathrm{d} + \mathrm{n} + \mathrm{p} \quad (Q = -26.07\ \mathrm{MeV})$$
$$\gamma + {}^4\mathrm{He} = \mathrm{n} + \mathrm{p} + \mathrm{n} + \mathrm{p} \quad (Q = -28.30\ \mathrm{MeV}).$$

For the first time the two-body and three-body photodisintegration cross sections were measured simultaneously by Shima et al. in the energy range from 21.8 to 29.8 MeV [94]. The quasi-monoenergetic γ-ray beam was produced via Compton backscattering of laser light from relativistic electrons [86]. A nearly 4π time-projection chamber was used to detect the charged particles from the breakup of ^{4}He in an event-by-event mode. The accuracy of this new experimental method was verified in auxiliary measurements of the photodisintegration cross section of deuterium [94]. The same method was also used in the work of Naito et al. [84] in their measurements of the two-body and three-body breakup cross sections of ^{3}He (see Section 4.1.1 on two-body breakup of ^{3}He).

According to [94] the three-body photodisintegration cross section below $E_\gamma = 30$ MeV contributes only at the 3% level to the total photodisintegration cross section of ^{4}He. Therefore, we will concentrate in the following on the two-body photodisintegration cross section only.

4.2.1. Two-body photodisintegration of ^{4}He

The experimental determination of the cross-section ^{4}He(γ, p)^{3}H to ^{4}He(γ, n)^{3}He ratio has a long history [94,95]. By accurately determining this ratio it appears that Shima et al. have resolved the long-standing problem associated with claims

of large charge-symmetry breaking (CSB) effects in these two reactions. Their result for the cross-section ratio agrees well with the recent calculations of Quaglioni et al. [95] without introducing CSB effects in addition to those already included in the Av18 nucleon–nucleon potential model. However, the individual cross sections for the two reactions ^{4}He(γ, p)^{3}H and ^{4}He(γ, n)^{3}He disagree by about a factor of two with these calculations at $E_\gamma = 24.3$ MeV and 26.5 MeV, while the disagreement at $E_\gamma = 29.8$ MeV is only about 10%. Furthermore, the findings of Shima et al. for the ^{4}He(γ, n)^{3}He cross section at $E_\gamma = 24.3$ MeV and 26.5 MeV [94] are in clear disagreement with the very recent data of Nilsson et al. [96] at $E_\gamma = 24.6$ MeV and 26.7 MeV.

The results of Shima et al. [94] have far reaching consequences. The weak nuclear operators for the neutral current have the same mathematical structure as those for the strong nuclear electromagnetic current. If the data of Shima et al. were correct, they would significantly affect the production of r-nuclei by neutrino induced r-process nucleosynthesis.

In order to resolve this important issue, preparations are underway to measure the two-body breakup cross sections of ^{4}He at HIγS in the 20–30 MeV energy range using high-pressure ^{4}He gas scintillators as 4π detectors. Ideally, one wants to measure both reactions at the same time using the same target-detector system. For monoenergetic incident γ rays of 25.5 MeV the charged particles from the reaction ^{4}He(γ, p)^{3}H deposit 5.30 MeV of energy, while the ^{3}He particles from the reaction ^{4}He(γ, n)^{3}He have energies between 0.64 MeV and 1.70 MeV. In high-pressure gas scintillators the measured pulse height is a linear function of the deposited energy, independent of the nature of the strongly ionizing particle. Therefore, there is more than sufficient pulse-height separation between the reaction products of the two reactions of interest. However, at $E_\gamma = 25.5$ MeV the maximum proton energy from the reaction ^{4}He(γ, p)^{3}H is 4.50 MeV. The associated large difference in the range of the protons and ^{3}He ions of interest makes it a challenge to find the optimal total gas pressure and ^{4}He/Xe pressure ratio. Even with a total pressure of 150 atm there is need for adding some Xe to increase the stopping power for the protons, while at the same time the associated increase of the electron pulse height reduces the pulse-height separation between ^{3}He ions and electrons. If it turns out to be impossible to use one single gas scintillator, we will use two different, but individually optimized gas scintillators mounted back to back. This ensures that at least the γ-ray flux seen by the two different target-detector systems will be the same (except for γ-ray attenuation in the first gas scintillator) for both the ^{4}He(γ, p)^{3}H and ^{4}He(γ, n)^{3}He reaction. Equally important is the knowledge of the exact γ-ray energy and the associated γ-ray energy spread. Considering the rapid increase of the two cross sections below $E_\gamma = 26$ MeV and the narrow width of the calculated giant dipole peak, it is essential to use as small of a γ-ray energy spread as practically possible. Clearly, a 1% energy spread or better is desirable. For example, the γ-ray energy spread used in [94] was 6% compared to about 1% in [96]. This difference in γ-ray energy spread may be one of the reasons for the contradictory results obtained in the two experiments.

5. Study of oxygen formation in stellar helium burning with an optical readout time projection chamber (O-TPC)

Carbon and oxygen are produced during helium burning in Red Giant stars after which the star either undergoes supernova explosion (for $M > 8M_\odot$) or collapses to a white dwarf. Carbon and oxygen are some of the most important elements required to support life as we know it on earth, and as such, the understanding of the origin of carbon and oxygen was eloquently designated by Willie Fowler (in his 1984 Nobel Prize address to the APS) [97] as the "holy grail" of Nuclear Astrophysics. Moreover, the ratio of carbon to oxygen (C/O) at the end of helium burning is one of the most important parameters of stellar evolution theory. In a massive star (at least $8M_\odot$) the C/O ratio determines whether the star that undergoes Type II supernova collapses to a black hole as predicted for an oxygen rich star, or a neutron star as predicted for a carbon rich star [98]. A sun-like star that ends up as a carbon plus oxygen white dwarf is the progenitor star for a Type Ia supernova (SNeIa) explosion that produces as much light as an entire galaxy. The peak luminosity of a SNeIa is understood (empirically) to be related to its light curve [99] and as such SNeIa are now used as a standard candle for measuring distances comparable to the size of the observed universe (13.7 Billion Light Years). These Hubble type measurements of cosmological distances (using SNeIa) allow us to conclude that the universe is composed for the most part of dark matter (approximately 23%), and dark energy (approximately 73%) with the latter giving rise to a recent (5 Billion years ago) accelerated expansion of the universe [100]. The C/O ratio of a white dwarf affects the peak luminosity and the shape of the light curve of SNeIa [101]. Thus the understanding of stellar evolution and the calibration of the peak luminosity-light curve relationship [99] of SNeIa are essential for placing this conclusion on a firm theoretical foundation. The formation cross sections which govern the C/O ratio of a given star must be determined from laboratory measurements.

The outcome of helium burning is the formation of the two elements, carbon and oxygen [97,98,102]. The first stage in helium burning, the formation of ^{12}C via the triple alpha-particle capture reaction, is well understood ($\pm$12%) [97] and is denoted, using standard Nuclear Physics notation, as the ^{8}Be(α, γ)^{12}C reaction. Thus one must extract the cross section for forming oxygen via the fusion of carbon plus helium denoted by ^{12}C(α, γ)^{16}O. This reaction is dominated by two partial waves and one must extract the p-wave (S_{E1}) and d-wave (S_{E2}) astrophysical S-factors:

$$S = E \times \sigma e^{(2\pi\eta)}, \tag{13}$$

where η is the Sommerfeld parameter ($\eta = Z_1 Z_2 \frac{\alpha}{\beta}$, with α being the fine structure constant and $\beta = \frac{v}{c}$) and σ is the measured reaction cross section [102]. The S-factors must be known with an accuracy of $\pm$10% or better at the Gamow peak at 300 keV where stellar helium burning occurs. Current data are measured with sufficient accuracy at energies not lower than 1.2 MeV and the extrapolation to stellar burning energies of 0.3 MeV is particularly difficult due to substantial

contributions from bound states of ^{16}O. One of the main open questions is whether the interference of the bound and quasi-bound 1^- state(s) is destructive or constructive, in which case it leads to either a very small or a large (S_{E1}) S-factor when extrapolated down to 300 keV. Data at lower energies are needed to resolve this problem.

5.1. Recent measurements of $^{12}C(\alpha,\gamma)^{16}O$

Following an idea first proposed by Fred Barker [103] in 1971, during the 1990s it was postulated that one can measure the p-wave E1 S-factor using the beta-decay of ^{16}N [104–110] followed by alpha decay of ^{16}O. The concept of using the beta-delayed alpha-particle emission of ^{16}N was introduced to compensate for the fast drop of the cross section at lower energies due to the penetration through the Coulomb barrier. It was suggested that the beta-decay phase space enhances (by approximately W_0^5; where W_0 is the total energy available for beta-decay) the probability for low energy alpha-particle emission and leads to an interference pattern that was suggested to be sensitive to S_{E1}. Indeed the TRIUMF group used their ^{16}N data to quote the S-factor with 25% uncertainty [108] and the problem was considered solved. But later it was shown by Hale [111] that the interpretation of the experimental data on the beta-delayed alpha-particle emission of ^{16}N is inconclusive and the astrophysical S-factor (S_{E1}) is still ill determined by at least a factor of 4 and as much as a factor of 8. A recent measurement of the spectrum of beta-delayed alpha-particle emission of ^{16}N carried out at Argonne National Lab [112] was found to be in disagreement with the TRIUMF data [107,108], but in agreement with the Yale-UConn data [106,109,110]. This disagreement further complicates the attempt to indirectly extract the E1 astrophysical cross section factor (S_{E1}) and mandates a direct measurement(s) of the cross section at low energies.

Recent direct measurements of γ-rays from the $^{12}C(\alpha,\gamma)^{16}O$ reaction at lower energies [113,114] reveal a number of interesting observations. We first note that these measurements suggest a d-wave S-factor (S_{E2}) that is at least twice as large as the previously "accepted value". In addition the low energy data point(s) that are measured with low precision can not rule out a small p-wave S-factor (S_{E1}), as suggested by Hale [111].

One tantalizing new problem that was posed by the new γ-ray data [114] is the disagreement between the E1-E2 mixing phase (ϕ_{12}) extracted from the measured γ-ray angular distributions and the mixing phase predicted by theory:

$$\phi_{12} = \delta_2 - \delta_1 + \arctan(\eta/2)$$

where δ_1 and δ_2 are the p and d wave elastic phase shifts and η is the Sommerfeld parameter. In Ref. [114] this disagreement is considered as a simple disagreement between data and the prediction of R-Matrix theory. But in fact the above relationship is rooted in the Watson theorem and unitarity. This disagreement is observed already at high energies on the broad 1^- resonance located at 9.58 MeV where the capture cross-section is large. This disagreement (of data with unitarity) must be resolved.

We conclude that the astrophysical S-factors, S_{E1} and S_{E2}, must be measured directly at energies as low as possible and as close as possible to the Gamow window located at 300 keV where stellar helium burning occurs. The use of intense γ-beams [115–117] appears to be very advantageous for this study and in particular the High Intensity γ-ray Source (HIγS). In addition the experiment we propose for HIγS will utilize an Optical Time-Projection Chamber (O-TPC) and will measure complete angular distributions with high sensitivity for extracting ϕ_{12} due to the fact that we can measure over a large angular range including angles close to the beam position where gamma ray data cannot be obtained. Thus our proposed experiment will also allow for a resolution of the disagreement of the extracted ϕ_{12} mixing phase angle.

5.2. The proposed $^{16}O(\gamma,\alpha)^{12}C$ experiment

In order to determine the cross section of the $^{12}C(\alpha,\gamma)^{16}O$ reaction at center-of-mass energies as low as 700 keV, considerably lower than measured till now, it is useful to have an experimental setup with three conditions: enhanced cross section, high luminosity and low background. It turns out that the use of the inverse process, the $^{16}O(\gamma,\alpha)^{12}C$ reaction may indeed satisfy all three conditions. The cross section of the $^{16}O(\gamma,\alpha)^{12}C$ inverse reaction at the kinematical region of interest (photons of approx 8–10 MeV) is larger by a factor of 40–100 than the cross section of the direct $^{12}C(\alpha,\gamma)^{16}O$ reaction as a result of *Detailed Balance*. It is evident that with similar luminosities and lower background (see below), the photodissociation cross section can be measured at center of mass energies as low as 700 keV, where the direct $^{12}C(\alpha,\gamma)^{16}O$ cross section can be estimated to be of the order of 10 pb (thus the corresponding photodissociation cross section is approximately 0.5 nb). A very small contribution (less than 5%) from cascade γ decay [118] can not be measured in this experiment, but appears to contribute at a level which is below the design goal accuracy of our measurement of $\pm$10%.

The backscattered photons from HIγS will be collimated and will enter the target/detector Optical Time Projection Chamber (O-TPC) setup as shown in Fig. 15. With a Q value of -7.162 MeV, our experiment will utilize gammas of energies ranging from 7.9 to 10 MeV. Note that the incident photons will be linearly polarized and the emitted particles will be primarily in a horizontal plane with a $1+\cos^2 2\phi$ azimuthal angular dependence which simplifies the tracking of particles. The O-TPC detector will measure all possible kinematical variables including: energy (E), particle identification (dE/dx), scattering angle (θ) and azimuthal angle (ϕ), as well as track length(s) and geometry. The scattering angle will be deduced with high accuracy from the tracks recorded in the CCD camera relative to the beam direction using the approximately

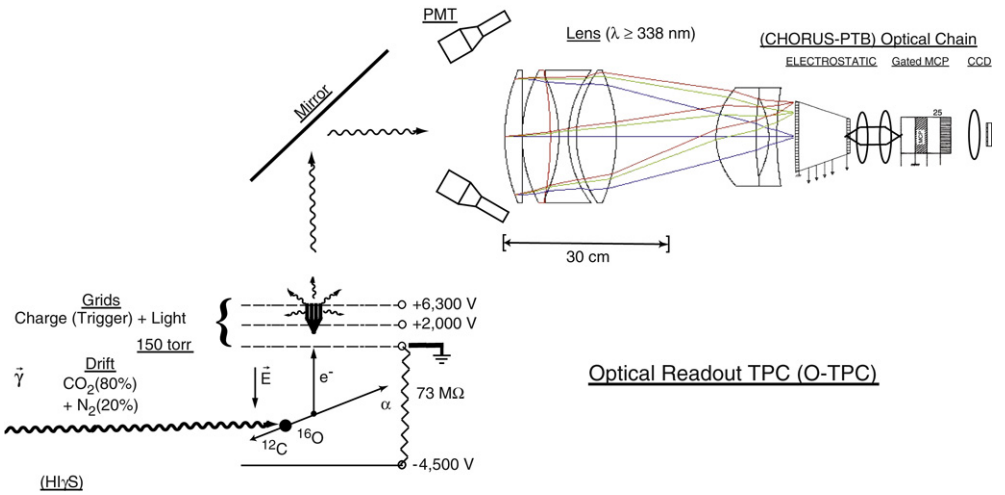

Fig. 15. A schametic of the optical time projection chamber (O-TPC).

5 cm long alpha track and approximately 1 cm long carbon track that are approximately 0.3 cm wide. The time projection information from the O-TPC will yield the azimuthal angle of the event of interest. The O-TPC detector will measure a complete angular distribution at each energy and will allow for a direct measurement of both the E1 and E2 amplitudes, as well as the mixing phase (ϕ_{12}).

The measured energy resolution of the TPC (3.2%), see below, will allow us to exclude events from the photodissociation of nuclei other than ^{16}O, including isotopes of oxygen that are present in the gas. The TPC is largely insensitive to e^+ e^- and single Compton electrons that deposit approximately 100 keV in the entire gas volume. Thus electron background events will be removed by requiring a total energy deposit larger than 1 MeV. We performed a test run at HIγS using silicon detectors immersed in helium gas exposed to 25 MeV γ-rays and we measured the outgoing particles (protons, deuterons and helions) in the presence of the large electron background. We concluded from this measurement that the electron background is manageable. We note that a similar research program with high intensity photon beams and a TPC already exists at the RCNP at Osaka, Japan [117], proving that tracks from low energy light ions can be identified in the TPC in the presence of the large electron background resulting from the intense γ beams. The Osaka experiment used a (traditional) TPC read by electronic channels, but our TPC is optically readout using Image Intensifiers and a cooled CCD camera, as we discuss below. An optical readout is very appropriate for such a low counting experiment and we chose such a readout due to the lower cost with most of the elements of the opto-electronic chain obtained from the CHORUS neutrino experiment at the Catholiqe University at Louvain-La-Neuve [119] and the gated micro-channel plate (MCP) provided by the Physikalisch-Technische Bundesanstalt (PTB), at Braunschweig, Germany. Currently we are also using a smaller lens of 60 mm diameter from PTB, considerably smaller than the design lens shown in Fig. 15 of 140 mm diameter.

5.2.1. The optical readout time projection chamber (O-TPC)

We have constructed an Optical Readout Time Projection Chamber (O-TPC) for the measurement of the ^{16}O$(\gamma,\alpha)^{12}$C reaction at HIγS. In Fig. 15 we show a schematic diagram of the constructed O-TPC which is based on the (OPAC) TPC constructed at the PTB and the Weizmann Institute, Rehovot, Israel [120]. Indeed OPAC was used as a prototype O-TPC for the design of the current detector. Extensive tests with $CO_2 + N_2$ gas mixtures (and other gas mixtures) as well as measurements of design performance were carried out at the Weizmann Institute and at the Laboratory for Nuclear Science (LNS) at Avery Point using OPAC [121]. Tracks of 1.0 MeV alpha particles were recorded using the prototype OPAC detector with a 10 cm diameter. The range of outgoing alpha-particles in the gas mixture is approximately 5 cm (at 150 torrs); hence the TPC is constructed with dimensions of 30×30 cm and 25 cm deep with the beam traveling in the center of the detector (at 12.5 cm height). The charged particles resulting from the photodissociation process induce secondary ionization electrons in the gas that drift along the electric field. The drift times are in the micro-second range. The electrons that reach the electron-amplification (cascade) parallel-grid avalanche multipliers are multiplied in an avalanche process by approximately a factor of 1000 or more, yielding the charge signals. Scintillation processes are induced by avalanche-electron excitations of nitrogen resulting in photons in the near UV range (mostly 338 nm and higher [121]). A fraction of the avalanche light is detected by the photomultiplier tube (PMT) shown in Fig. 15. The emitted light is focused by the lens onto a Hamamatsu V4440 (100-25 mm) demagnifier [119] with the (25 mm) back screen viewed by a Proxifier BZ2562 gated MCP Image Intensifier, also shown in Fig. 15. The cooled CCD camera, model SBIG2000XMI, takes a picture of the tracks displayed on the (25 mm) back screen of the Image Intensifier. Dedicated software has been developed for pattern recognition algorithms to select the typical back-to-back alpha-carbon tracks.

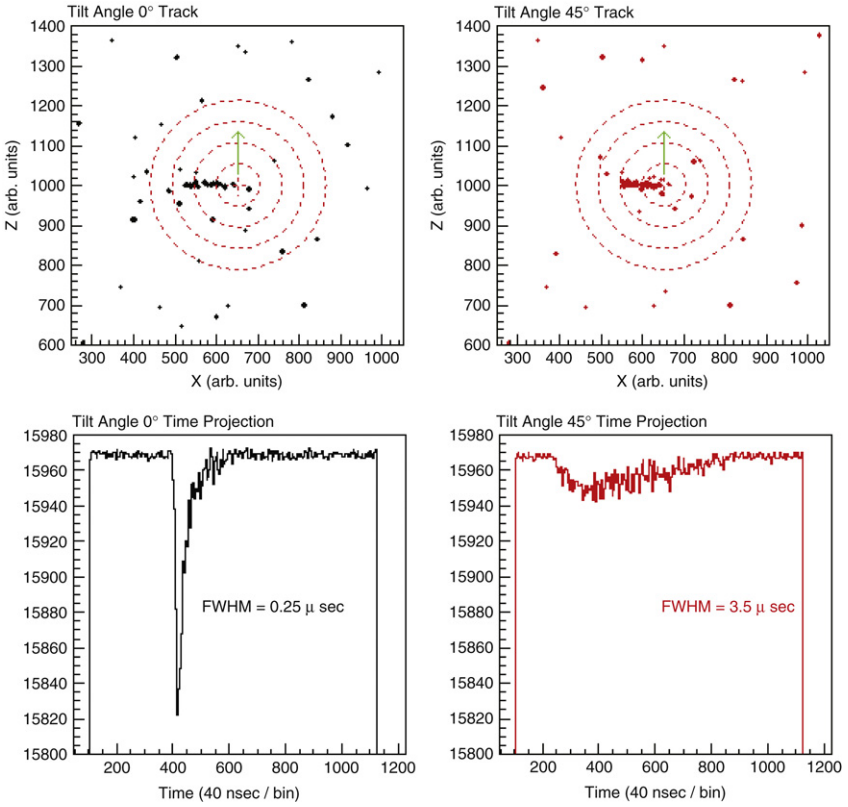

Fig. 16. The figure shows two tracks of α particles with different out-of-plane angles (β) of 0° (upper-left) and 45° (upper-right). The related time projections are shown at the bottom, respectively.

5.2.2. Tests and calibration of the O-TPC

Extensive tests and calibrations of the O-TPC were conducted at the LNS at Avery Point using a high resolution low intensity (10 nCi) ^{148}Gd source that emits 3.183 MeV alpha particles [122]. Further reduction of the energy of the alpha-particles was achieved by using thin (0.0008 cm) Mylar absorber foils. The total charge signal was preamplified in a charge sensitive CANBERRA 2003 preamplifier and analyzed in a spectroscopic amplifier with a large 6 μs shaping time. The resulting spectrum had a resolution (FWHM) of 2.6%.

The PMT pulses were digitized to allow for a measurement of the pulse shape and are shown in Fig. 16. For (horizontal) tracks parallel to the grid plane, the drift time of all electrons are very similar resulting in a pulse shape that is narrow in time. The time spread provides a direct measurement of the track inclination and thus the azimuthal angle; as for the standard Time Projection method. Tracks of 3.18 MeV alpha-particles from the ^{148}Gd source were recorded in the CCD camera and are shown in Fig. 17. At the gas pressure of 150 torr these tracks are only approximately 5 cm long and they occupy a small fraction of the total fiducial field view of the optical system. We note that the tracks are recorded with a very small background from stray light.

5.2.3. Design goal

The luminosity of our proposed $^{16}O(\gamma,\alpha)^{12}C$ experiment can be very large. For example, with a 30 cm long target with CO_2 gas at a pressure of 150 Torr and a photon beam of 5×10^7/s (phase 1), we obtain a luminosity of 1.5×10^{28} s^{-1} cm^{-2} (1.5 nb^{-1}/day). Thus a measurement of the photodissociation of ^{16}O with a cross section of 30 nb yields 45 counts per day, leading to a design goal sensitivity for measuring the direct $^{12}C(\alpha,\gamma)^{16}O$ reaction with a cross section as low as 0.5 nb, corresponding to energies as low as 1.5 MeV. A further upgrade of the beam intensity would be required for Phase 2 to approach the design goal sensitivity of 700 keV. The anticipated S_{E1} S-factors that will be extracted in Phase 1 and 2 are shown in Fig. 18.

Time Projection Chamber (TPC) detectors records tracks of outgoing particles, and thus one can measure scattering angles very close to 0° and 180°. Such data are not possible when measuring with a gamma-detector due to the finite size of the detector. In Fig. 19 we show simulated angular distributions to be measured with our O-TPC and we compare it to the measured values from EUROGRAM and to the value expected using the phase difference obtained from elastic scattering data (unitarity). We note that the determination of small values of ϕ_{12}, which are predicted by unitarity and the Watson Theorem, requires good data at very large scattering angles close to 180°. These data are missing in the gamma-ray study [114], but

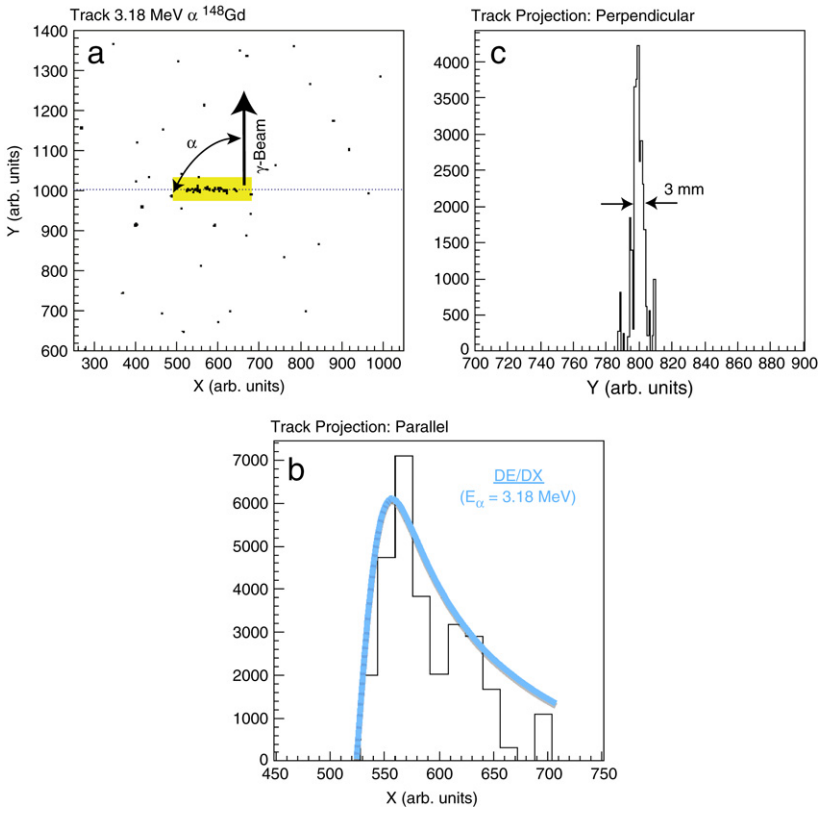

Fig. 17. Two projections of an α particle track (upper-left) are shown in this figure. A projection perpendicular to the track (upper right) equates to a total energy spectrum, and a parallel projection (bottom) indicates the range of the α particle in the gas mixture.

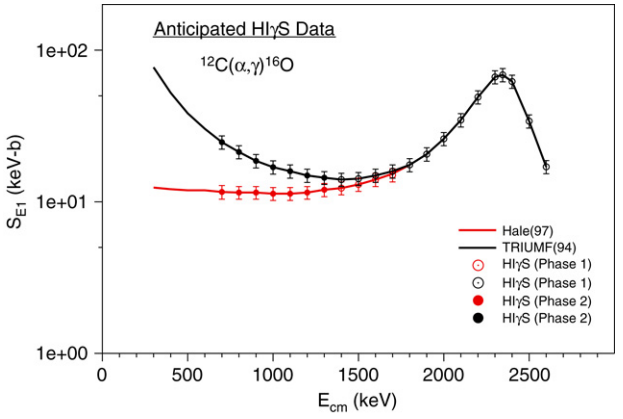

Fig. 18. The plot shows the anticipated HIγS measurement for the determination of S_{E1}.

can be obtained with our O-TPC. We also emphasize that large values of $\frac{S_{E2}}{S_{E1}}$ can be mimicked by large mixing phase ϕ_{12}. Thus if, in fact, the phase angle is small, as required by unitarity, we may conclude that the values of $\frac{S_{E2}}{S_{E1}}$ ratios are even larger than concluded in [114] and are considerably larger than "the accepted" values. These issues can only be resolved by measuring detailed angular distributions as we intend to do with the O-TPC at HIγS.

6. The Gerasimov–Drell–Hearn sum rule on the deuteron and ^{3}He

The range of physics problems which can be addressed using the HIγS facility is quite broad. In this section we will describe work which has been performed and planned work for the future studies of a fundamental sum rule in photonuclear physics known as the Gerasimov–Drell–Hearn (GDH) sum rule.

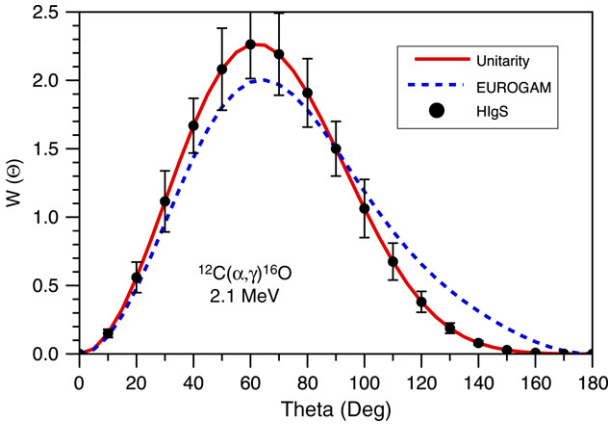

Fig. 19. The figure shows the anticipated angular distribution data at HIγS compared to the best fit for the EUROGAM data and the prediction based upon elastic scattering data (unitarity), as discussed in the text.

The Gerasimov–Drell–Hearn (GDH) sum rule is a measure of the spin response of any composite system. The sum rule relates the helicity dependent photoabsorption cross-section difference to the anomalous magnetic moment, κ, of the target. For a nuclear target with a ground state mass M, an anomalous magnetic moment κ, and a spin S, the GDH sum rule states

$$I^{GDH} = \int_{\omega_{th}}^{\infty} (\sigma_P(\omega) - \sigma_A(\omega)) \frac{d\omega}{\omega} = 4\pi^2 e^2 \frac{\kappa^2}{M^2} S, \tag{14}$$

where $\sigma_{P/A}$ is the photoabsorption cross section with photon and target spins parallel/anti-parallel, ω is the incident photon energy, and ω_{th} is the threshold energy for the inelastic process. The GDH integral is derived using Lorentz and gauge invariance, crossing symmetry, unitarity, and an unsubtracted dispersion relation applied to the forward Compton scattering amplitude [123]. A related sum rule is the sum rule for the forward spin polarizability γ_0:

$$\gamma_0 = \frac{-1}{8\pi^2} \int_{\omega_{th}}^{\infty} (\sigma_P(\omega) - \sigma_A(\omega)) \frac{d\omega}{\omega^3}. \tag{15}$$

Due to the $1/\omega^3$ weighting, this sum rule integral is expected to converge quite rapidly. The quantity γ_0 for the deuteron has been calculated to next-to-leading order in the pionless effective field theory [124]. Their result indicates that $\gamma_0 = 4.262$ fm^4. We will return to this subject later.

The GDH sum rule is interesting since it relates a static ground state property, the anomalous magnetic moment, to the excitation spectrum of the target. A finite anomalous magnetic moment restricts the energy-weighted integrated photoabsorption cross-section asymmetry to be positive, *i.e.*, the energy weighted cross section with photon and target spins parallel must be greater than the antiparallel cross section over the full integral.

The deuteron has a small anomalous magnetic moment ($\kappa_d = -0.143$ [125]). The measured value for κ_d predicts a GDH value of $I_d^{GDH} = 0.652$ μb. This value is significantly less than the predicted GDH values for the proton ($I_p^{GDH} = 204$ μb) and the neutron ($I_n^{GDH} = 232$ μb).

A theoretical calculation of the GDH integral for the deuteron has been performed by Arenhövel et al. [126] up to an energy of 2.2 GeV. This calculation includes the contributions from the photo-disintegration channel (up to 0.8 GeV) along with the contributions from the coherent and the incoherent single-pion production channels (up to 1.5 GeV for single pion production and 2.2 GeV for double pion production). Fig. 20 shows the predicted results of the GDH integrand of the deuteron up to 550 MeV.

As stated in Ref. [126], a very interesting and important result of this theory is the large negative contribution from the photodisintegration channel near the breakup threshold along with a large relativistic contribution below 100 MeV. Note that the integral up to 10 MeV is predicted to be ~ -630 μb while the value up to pion-production threshold is about -530 μb. The largest positive contribution to the GDH integrand arises from the relativistic correction in the energy region up to 100 MeV. As pointed out in the Ref. [127], this large relativistic effect is not surprising since the correct form of the term linear in photon momentum in the low-energy expansion of the Compton amplitude is only obtained if leading order relativistic contributions are included. The present work is the first attempt to test the prediction of the value of the GDH integral between photodisintegration threshold and 10 MeV. Clearly, future studies to verify the positive contribution below pion-threshold will be of great interest.

Measurements of the GDH integral on the proton and neutron to test the GDH Sum Rule have been and are being performed at MAMI, LEGS, ELSA and JLAB.

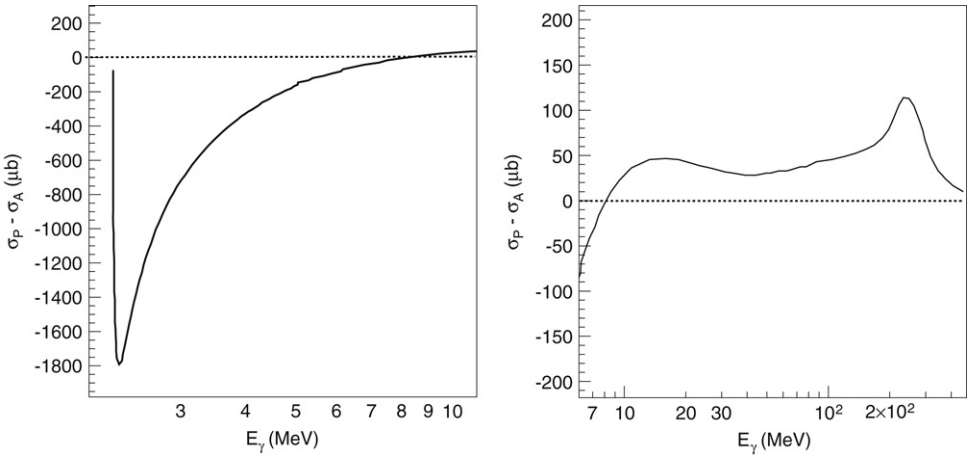

Fig. 20. The GDH sum rule integrand ($\sigma_P - \sigma_A$) for the deuteron as calculated in Ref. [126]. The left figure shows the large, negative near-threshold prediction, and the right figure shows the positive contributions which appear at higher energies.

The GDH integral for the deuteron having mass M_d and anomalous magnetic moment κ_d can be separated into two pieces

$$\int_{\omega_{th}}^{\infty} \mathrm{GDH}_d = \int_{\omega_{th}}^{k_\pi} \mathrm{GDH}_d + \int_{\omega_\pi}^{\infty} \mathrm{GDH}_d = 4\pi^2 \left(\frac{\kappa_d \mathrm{e}}{M_d}\right)^2 = 0.6\ \mu\mathrm{b} \tag{16}$$

where ω_{th} and ω_π correspond to the photodisintegration and photo-pion production threshold energies, respectively. The second term on the right hand side has been measured at LEGS, MAMI and ELSA. Its value can be estimated from the GDH integrals for the nucleons under the assumption that the impulse approximation is valid (this assumption is useful to obtain this estimate but is not significant to the basic argument since what will actually be measured at MAMI, LEGS, ELSA, and JLAB is the GDH integral for the deuteron). Thus,

$$\int_{\omega_\pi}^{\infty} \mathrm{GDH}_d = (204\ \mu\mathrm{b}) + (232\ \mu\mathrm{b}) = 436\ \mu\mathrm{b}. \tag{17}$$

Therefore, the previous equation predicts that

$$\int_{k_2}^{\omega_\pi} \mathrm{GDH}_d \cong -436\ \mu\mathrm{b}. \tag{18}$$

That is, if the assumptions underlying the GDH sum rules are generally valid, then asymmetries in the total cross sections dominated by high energy pion production and resonance excitation processes give a firm prediction for asymmetries in a very low-energy process, namely photodisintegration below pion threshold. This is a connection that merits testing.

6.1. Indirect determination of the GDH sum rule for the deuteron

A direct determination of the GDH sum rule integrand requires polarized targets and circularly polarized γ-ray beams. This measurement will be performed at HIγS from breakup threshold up to photopion-production energies once the current upgrades are completed. Meanwhile, a number of photodisintegration experiments on the deuteron using linearly polarized γ rays and unpolarized targets have been performed [128–131]. These experiments covered a range of γ-ray energies between 2.39 and 16 MeV. The focus of the majority of these experiments was to measure the photon asymmetry of the reaction. The asymmetry ($\Sigma(\theta)$) is given by

$$\Sigma(\theta) = \frac{1}{f}\frac{\sigma(\theta, \phi = 0^\circ) - \sigma(\theta, \phi = 90^\circ)}{\sigma(\theta, \phi = 0^\circ) + \sigma(\theta, \phi = 90^\circ)}, \tag{19}$$

where θ is the polar angle and ϕ is the azimuthal angle. The factor f is the fraction of linear polarization in the beam which is taken to be 1.0 ± 0.02 in the case of the γ-ray beams at HIγS [63].

The formalism of Ref. [132] can be used to write the GDH integrand in terms of the contributing transition matrix elements. Since we expect only $l = 0, 1, 2$ (s, p, and d waves) in the outgoing n–p channel at very low energies, we obtain:

$$\begin{aligned}\sigma_P - \sigma_A = \frac{\pi\lambda^2}{2}\Bigg[&-|M1(^1S_0)|^2 - |E1(^3P_0)|^2 - \frac{3}{2}|E1(^3P_1)|^2 + \frac{5}{2}|E1(^3P_2)|^2 \\ &- \frac{3}{2}|E2(^3D_1)|^2 - \frac{5}{6}|E2(^3D_2)|^2 + \frac{7}{3}|E2(^3D_3)|^2\Bigg],\end{aligned} \tag{20}$$

where the notation $(L_P)^{(2S+1)}l_J$ specifies the S (spin), l (orbital angular momentum), and J (total angular momentum) value of the outgoing n–p channel and L_P specifies the multipolarity and mode of the incoming γ ray. In obtaining this expression we are neglecting the M1($^3S_1$), E1($^1P_1$), and E2($^1D_2$) terms, which are expected to be negligibly small (see Ref. [131]). If splittings of the p- and d-waves are ignored so that the three p-wave amplitudes are taken to be equal to each other and the same for the three d-wave amplitudes, then only the M1($^1S_0$) term contributes. In this simplified form the GDH integrand becomes

$$\begin{aligned}\sigma_P - \sigma_A &= \frac{\pi\lambda^2}{2}[-|M1(^1S_0)|^2] \\ &= -3\sigma(M1). \end{aligned} \tag{21}$$

This result indicates that a measurement of the M1 cross section in a photodisintegration experiment is an indirect determination of the GDH sum rule value for the deuteron at very low energies.

An analysis of data from several photodisintegration experiments at HIγS was performed in order to extract information on the GDH integrand below 10 MeV [133]. Additional results were obtained from previously measured polarized neutron capture on proton data as well as unpolarized photodisintegration reaction studies which measured the outgoing neutron polarization [133].

6.1.1. Analysis of data

As reported in [133], the data on the M1 contribution from this experiment and others [128,129,131,136–139] were analyzed in order to obtain the GDH sum rule integrand using Eq. (21). The data of Refs. [128,131,139] were obtained by photodisintegrating the deuteron and measuring the photon asymmetry $\Sigma(\theta = 90^\circ \text{ or } 150^\circ)$. As described in Ref. [133], the fractional M1 contribution to the total cross section can be extracted from these measurements if it is assumed that the reaction proceeds only via M1(s-wave) and E1(p-wave) transitions. In order to extract the absolute M1 contribution to the total cross section, the experimentally measured fractional M1 contributions S(M1) were multiplied by the theoretical total photodisintegration cross sections. The total photodisintegration cross sections given by the Effective Field Theory (EFT) calculation of [134] and the potential model calculations of [135] are the same and agree with available data. Either one can be used to normalize the fractional S(M1) contributions to the total cross section. The data set of [129] was obtained using the same technique with full angular coverage between $\theta = 22.5^\circ$ and 157.5°. In this case, the asymmetry and cross section data as a function of angle were fit using expressions obtained from Ref. [140] in terms of the amplitudes (M1, E1, and E2) and one relative phase ($\phi_P - \phi_D$) in order to obtain M1, E1, and E2 contributions to the total cross section. The relative phase was set equal to the relative phase obtained from an n–p scattering phase shift analysis ($\sim 2^\circ$) [141] by invoking Watson's theorem [142]. Since the three triplet (E1) p-wave and the three triplet (E2) d-wave amplitudes were constrained to be equal, respectively, they did not contribute to the GDH integrand, as shown in Eq. (20).

As previously mentioned, an alternative means of obtaining the same information about the near threshold value of the GDH integrand for the deuteron is from the polarized radiative capture reaction p($\vec{n}$, γ)d. In this case it can be shown that the vector analyzing power at 90° is, for the case in which only S(M1) and P(E1) transition matrix elements contribute, given by:

$$A_y(90^\circ) = \frac{3|S||P|\sin(\phi_S - \phi_P)}{1 + \frac{9}{2}P^2}, \tag{22}$$

with

$$9|P|^2 + |S|^2 = 1.0. \tag{23}$$

As seen in Eq. (22), the vector analyzing power at 90° arises from the interference between the s- and p-wave amplitudes, and is proportional to the phase difference between these two transition matrix elements. As before the s- to p-wave phase difference can be obtained using the n–p elastic scattering phase shifts. These phase shifts were obtained from the SAID analysis [141]. The value of σ(M1) has been obtained from the value of $|S|^2$ (which is proportional to the percentage of the total cross section due to M1 radiation) using the total cross section as calculated in Ref. [134]. The polarized n–p capture data from Ref. [137] were analyzed using Eq. (22). The results are shown in Fig. 21.

One additional source of information on the M1 strength is the time reversed reaction to the polarized n–p capture study: the unpolarized photodisintegration of the deuteron in which the outgoing neutron polarization is determined. Since time-reversal invariance implies that $A_y(\theta) = P_n(\theta)$, the neutron polarization, $P_n(\theta)$, can be written in an expression which is identical to Eq. (22). Data from [136–138] were analyzed to obtain the relative S strength using Eqs. (22) and (23), and the resulting values were converted to an absolute σ(M1) cross section using the theoretical values of the total cross section as in the case of the n–p capture analysis. These results are also shown in Fig. 21.

Another data point is also available as a result of the fact that the thermal n–p capture cross section ($E_n \sim 0.025$ eV) is well measured. The value of this cross section is 332 ± 0.60 mb [143], and is known to be a pure M1 cross section. In order to include this in the results shown in Fig. 21, we use the principle of detailed balance to connect it to the photodisintegration cross section, then convert it to $\sigma_P - \sigma_A$ using the fact that this is equal to -3σ(M1). The result is that for $E_\gamma = 2.225$ MeV, $\sigma_P - \sigma_A = -1.641 \pm 0.0031$ μb. This point is also shown in Fig. 21.

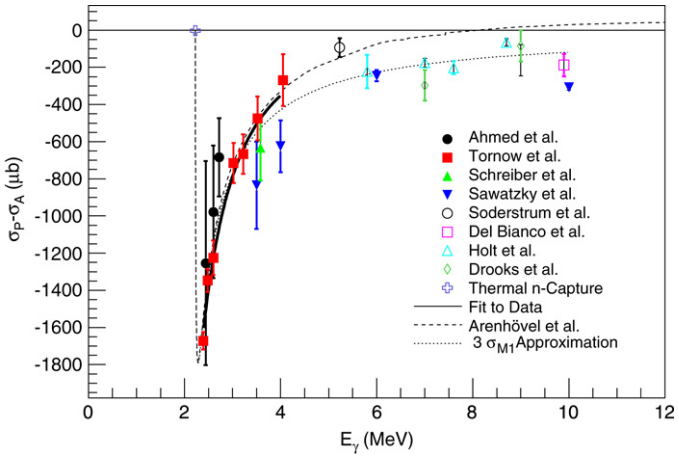

Fig. 21. (Color online) Experimental data points for the GDH sum rule integrand are shown along with their statistical errors. The thick solid curve is a fit to the data while the dashed curve is the prediction from Ref. [126]. The dotted curve is the same theory assuming $\sigma_P - \sigma_A = -3\sigma(\mathrm{M1})$. Figure is from Ref. [133].

The results of all of the above extractions of $\sigma_P - \sigma_A$ are summarized in Fig. 21. Recall that the basic assumptions made to obtain these results are that the photodisintegration of the deuteron at these energies can be described using M1 (with outgoing s-waves), E1 (with outgoing p-waves) and E2 (with outgoing d-waves). In addition, we have assumed that there is no splitting in the triplet E1 p-wave amplitudes and, likewise, in the triplet E2 d-wave amplitudes.

The theoretical predictions of [126] are also shown in Fig. 21 as the dashed line. We also show the result from this calculation which is obtained using the approximation $\sigma_P - \sigma_A = -3\sigma(\mathrm{M1})$. As can be seen in Fig. 21, these two results are in excellent agreement below $E_\gamma \sim 3.3$ MeV, but begin to separate above this energy. This is understood as being the result of a contribution to $\sigma_P - \sigma_A$ arising from the splitting of the triplet p-wave matrix elements and the triplet d-wave matrix elements with increasing energy. Despite some scatter in these data points obtained from very different experiments, the agreement between data points and the theory using the $\sigma_P - \sigma_A = -3\sigma(\mathrm{M1})$ approximation is, at least qualitatively, quite reasonable.

The full theory, when integrated over energy from threshold to $E_\gamma = 10$ MeV using Eq. (14), predicts a value of -634 μb. The theory also indicates that the value of this integral up to pion threshold is -520 μb. A positive contribution (theoretically arising from a relativistic contribution) between 10 MeV and pion-threshold must be responsible for this reduced value, but remains to be experimentally verified.

In order to extract an experimental value for the GDH integral from the results of Fig. 21 a fit was performed on the data of Fig. 21. The functional form of our fit was taken to be Lorentzian. A Lorentzian, parameterized by amplitude, width, and centroid, was used to fit the data by use of the minimization routine MINUIT [144]. Since the s-wave only approximation breaks down as the energy increases, the fit was limited to data below 4 MeV. The results of this procedure produced the solid curve shown in Fig. 21. The integral of this function from photodisintegration threshold up to 6 MeV was found to be -603 ± 43 μb. This experimental value is in agreement with the theoretical value of -627 for the GDH sum rule integrated over the same energy range and the value of -662 obtained from the $-3\sigma_{M1}$ approximation.

In addition to determining the GDH integral value in this near threshold region, the results shown in Fig. 21 can also be used to determine the value for the forward spin polarizability using Eq. (15). The result of integrating from threshold to 6 MeV is $\gamma_0 = 3.75 \pm 0.18$ fm^4. This result agrees with the leading order calculation ($\gamma_0^{LO} = 3.762$ fm^4), but is somewhat lower than the NLO result ($\gamma_0^{NLO} = 4.262$ fm^4). This difference is due to the very limited energy range of the experimental results, although the $1/\omega^3$ energy weighting in Eq. (15) does lead to fairly rapid convergence of this integral as shown in Fig. 22. The results are reported in Ref. [133].

6.1.2. Determination of the p-wave splittings and the GDH sum rule integrand at higher energies

This indirect determination of the GDH integrand for the deuteron has confirmed the prediction that the $^1S_0$ *state* of the deuteron gives rise to a large negative contribution to the value of the GDH integral below $E_\gamma = 10$ MeV. Quantitatively, the value we obtain is in agreement with the value predicted by the calculation of Ref. [126], although our result has a 7% uncertainty. Nevertheless, these results constitute the clearest experimental signature of the $^1S_0$ resonance in the deuteron to date.

Another HIγS experiment took advantage of the large solid-angle coverage of a segmented neutron detector array (Blowfish) to make precision measurements of the d($\vec{\gamma}$, n)p reaction at 14 and 16 MeV [130]. The Blowfish detector array, shown in Fig. 23, consists of 88 liquid scintillator (BC-505) neutron detectors positioned spherically around the target location at a radial distance of 16 in. from the target center. The array provides large angular coverage (about 25% of the 4π solid angle), allowing the detailed shape of the angular distribution of the polarized cross section to be measured. The

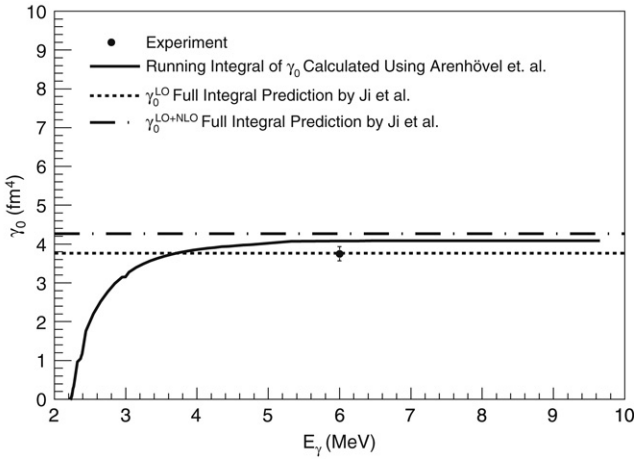

Fig. 22. Running integral of γ_0 calculated using $\sigma_P - \sigma_A$ predictions of Arenhövel et al. [126,135]. Also shown are the values of the full integral predictions of Ji et al. [124] for γ_0^{LO} and γ_0^{LO+NLO}. The predictions are compared to the experimental result integrated up to 6 MeV. Figure is from [133].

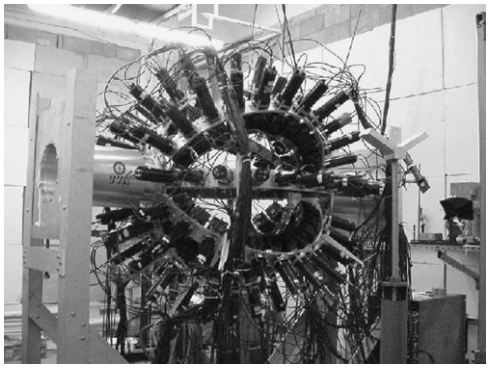

Fig. 23. The blowfish 88-neutron detector array. The front face of all detectors is located 16 in. from the center of the target.

detectors are mounted on 8 semicircular arms equally spaced by $\Delta\phi = 45°$, with 11 detectors per arm. Coverage in θ extends from 22.5° to 157.5° with $\Delta\theta = 13.5°$.

The liquid scintillator detectors allow pulse-shape discrimination (PSD) to be employed for distinguishing neutrons from γ-rays which enter the detectors. A gain monitoring system was used to carefully monitor the gains of each detector by means of a light pulse from a light-emitting diode (LED) which was periodically sent to each detector in the array. In addition, the entire array rotates as a rigid body around the beam axis, allowing systematic effects to be canceled by performing periodic rotations of the array by 45° in ϕ.

After being collimated to a size of 2.5 cm in diameter, the HIγS beam was incident upon a target which consisted of a thin-walled 4.7 cm long plastic container filled with heavy water (D_2O). An identical H_2O target was used to study backgrounds, which were found to be negligible. The pulsed nature of the HIγS beams allowed time-of-flight techniques to be used to reduce non-beam related backgrounds and to identify neutrons from the photodisintegration reaction. Collimated beam-on-target fluxes for this experiment were on the order of 10^5 γ/s.

The raw neutron yields were obtained after applying a PSD cut as well as a common pulse height cut for all detectors, and then summing the counts in the time-of-flight spectrum with a timing corresponding to that which is expected for neutrons of interest based on the kinematics of the reaction.

The angular distribution of the raw yields can be used to construct the two observables accessible for a measurement with linearly polarized beams and unpolarized target: the unpolarized differential cross section, $\sigma(\theta)$, and the linear analyzing power, $\Sigma(\theta)$, as defined in Eq. (19).

A Monte Carlo simulation was developed using the GEANT4 simulation toolkit [145] in order to correct for effects such as multiple scattering and finite geometry of the target and detectors. This was done by altering the angular distribution of neutrons resulting from the photodisintegration reaction until the simulated data obtained from GEANT4 matched the raw experimental yields. The cross section which was input into GEANT4 was parameterized in terms of associated Legendre

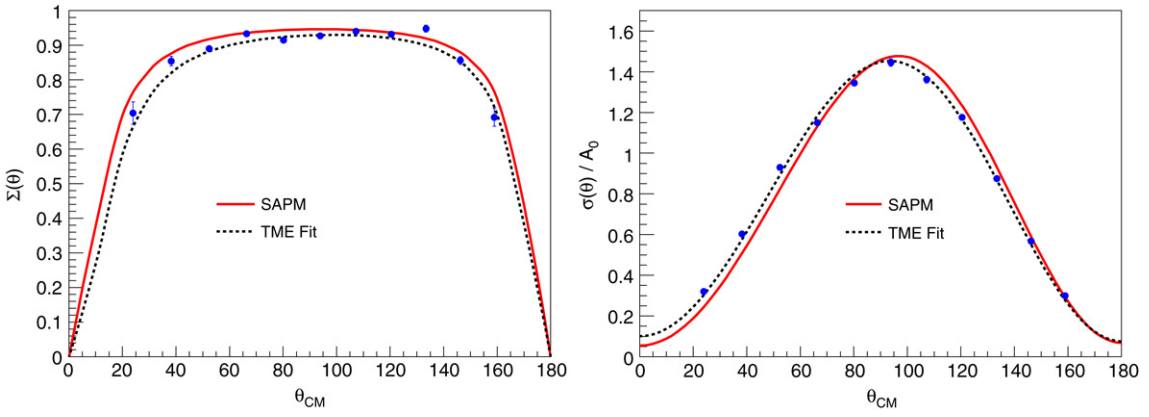

Fig. 24. (Color online) 14 MeV observables along with fits from the extraction of the TME amplitudes. The solid red curves are from the calculation of Ref. [126] (SAPM) and the dotted black curves represent the fit to the data. The errors on the data points are statistical only. Figure is from Ref. [130].

polynomials according to

$$\sigma(\theta,\phi) = A_0\left[1 + \sum_{k=1} a_k P_k(\cos\theta) + \sum_{k=2} e_k P_k^2(\cos\theta)\cos 2\phi\right], \tag{24}$$

where the P_k and P_k^2 functions are the associated Legendre polynomials, and the a_k and e_k coefficients are parameters which were varied until the experimental results were reproduced. The A_0 parameter sets the overall scale of the total cross section, σ_T, via $\sigma_T = 4\pi A_0$. Since the absolute value of the cross section was not obtained from this measurement, A_0 was simply a scale factor, which was ultimately set to 1.0. It was found that satisfactory fits to the yields were obtained with $k \leq 4$. Finally, the observables were corrected by applying a factor to each data point consisting of the ratio of the observables based on the cross section that was input into GEANT4 to the outputted simulated observables from GEANT4.

The results for the observables obtained at 14 MeV are shown in Fig. 24 where they are compared to the theoretical results of Ref. [126] (which will be referred to as SAPM heretofore). The systematic errors on the data points were estimated to be of the same order of magnitude as the statistical errors (size of the dots in some cases) shown in Fig. 24.

The polarized differential cross section can be written in terms of the amplitudes and phases of the reduced transition matrix elements (TMEs) which contribute to the reaction at these energies using the formalism of [146]. The reduced TMEs represent the strength of the transition and are dependent upon only the radial part of the TMEs, with the angular part factored out. The TMEs are labeled by the electric or magnetic multipole responsible for the transition (i.e. $E1$, $M1$, $E2$, etc.), and the quantum numbers of the outgoing n–p system using the notation ${}^{2s+1}l_J$. The channel spin is denoted by s, which for two spin 1/2 particles can take on values of 0 or 1, l is the orbital angular momentum in spectroscopic notation (s-waves are l = 0, p-waves are l = 1, d-waves are l = 2, etc.), and J is the total spin, $\vec{l} + \vec{s}$.

Selection rules allow some of the TMEs to be omitted from the fits since they are expected to be negligible. For instance, negligible amplitudes are expected from the $E1\,{}^1\mathrm{p}_1$ term, since it corresponds to a a "spin-flip" electric transition, and from the $M1\,{}^3s_1$ term since it has the same quantum numbers as the ground state of the deuteron making it negligible due to orthogonality.

Using these and similar considerations along with guidance from the SAPM calculation and limiting ourselves to $M1$, $E1$, and $E2$ multipoles and partial waves less than or equal to $l = 2$, the following TMEs were included in the fits to the data: $(E1)\,{}^3\mathrm{p}_0$, $(E1)\,{}^3\mathrm{p}_1$, $(E1)\,{}^3\mathrm{p}_2$, $(E2)\,{}^3\mathrm{d}_1$, $(E2)\,{}^3\mathrm{d}_2$, and $(E2)\,{}^3\mathrm{d}_3$. The $(M1)\,{}^1s_0$ strength was set equal to the value predicted by SAPM [126].

The relative phases of the TMEs were fixed by using Watson's theorem [142], which identifies the TME phases with the n–p scattering phase shifts. This identification is valid as long as there are no other open reaction channels and if the mixing between orbital angular momentum states is small. Both conditions are met for the energies of this experiment. The n–p scattering phase shifts were obtained from the SAID phase shift analysis [141]. This left the seven TME amplitudes as free parameters in fits to the data, which are shown in Fig. 24.

The set of amplitudes obtained from the fits converged to two distinct solutions depending on the seed values for the amplitudes passed to the fit. Both solutions returned identical χ^2 values and neither could be eliminated as a possible solution from the point of view of the fits.

The results indicate very good agreement with the calculation of Ref. [126] for the percent contribution of the triplet $E1$ p-wave amplitudes. The results for the p-wave amplitudes for 14 MeV are shown as percentages of the total cross section and compared to the theory in Fig. 25. Also shown in the figure is the SAPM calculation [126] without the inclusion of relativistic currents, so that the dependence of the p-wave splittings on those effects can be seen.

As previously discussed, the quantity $\sigma_P - \sigma_A$, which enters into the GDH sum rule integrand, can be written in terms of the TME amplitudes extracted from the fits to the data. Since absolute normalizations were not obtained for the measured

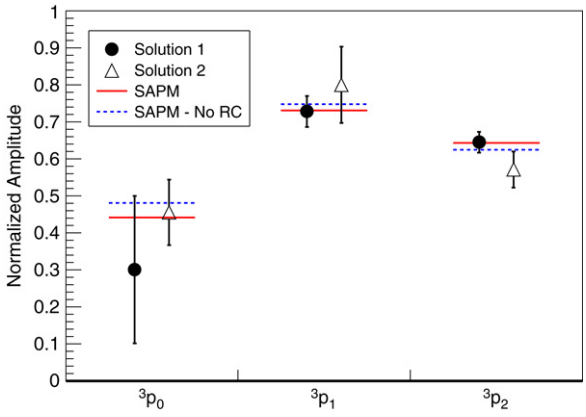

Fig. 25. (Color online) The squares of the three normalized triplet E1 p-wave amplitude at 14 MeV as extracted from the data and compared to the calculation of Ref. [126]. The solid red line is the prediction from the full calculation and the dashed blue line is the prediction for the calculation without the inclusion of the relativistic contributions (RC). Error bars are statistical only. Figure is from Ref. [130].

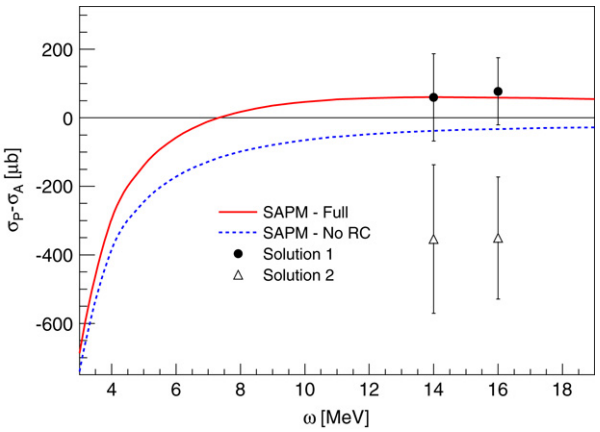

Fig. 26. (Color online) $\sigma_P - \sigma_A$ for the two solutions extracted for the TME amplitudes of the reaction at each beam energy. Also shown is the full calculation of Ref. [126] and the calculation without relativistic contributions (RC). Error bars are statistical only. Figure is from Ref. [130].

cross sections, the cross section difference was normalized using the theoretical value of the total cross section, which agrees with existing data to better than 10%.

The results for $\Delta\sigma$ are shown in Fig. 26 for both solutions at each energy. As can be seen from that figure, the different splittings obtained for the p-wave amplitudes result in very different GDH integrand results.

Although the experimental results do not favor one of these solutions over the other, the integrand values designated Solution 1 are to be preferred to those designated Solution 2, since the Solution 2 values would contribute to producing a total sum rule value that is much too negative, which would most likely violate the sum rule when integrated over all energies. These results are the first experimental indication of a positive value of the GDH integrand in the region near photodisintegration threshold. As Fig. 26 demonstrates, a positive value at these energies is due to the inclusion of relativistic contributions in the theory. These contributions must be included in the calculation in order to achieve the small value of the GDH sum rule expected for the deuteron when integrated over all energies.

A direct measurement of this integrand will begin at HIγS in 2008. This experiment will utilize the circularly polarized beams from OK-5, the 88-neutron detector array *Blowfish* [147] (as shown in Fig. 23), and a frozen-spin polarized target (described below). It is expected that the integrand between 10 and 100 MeV will be measured to an accuracy of about 3% in about 400 h.

6.2. The GDH sum rule for ^{3}He

The experimental determination of the GDH integral on ^{3}He from the two-body breakup to the pion production threshold is particularly interesting due to the fact that polarized ^{3}He nucleus is commonly used as an effective polarized neutron target.

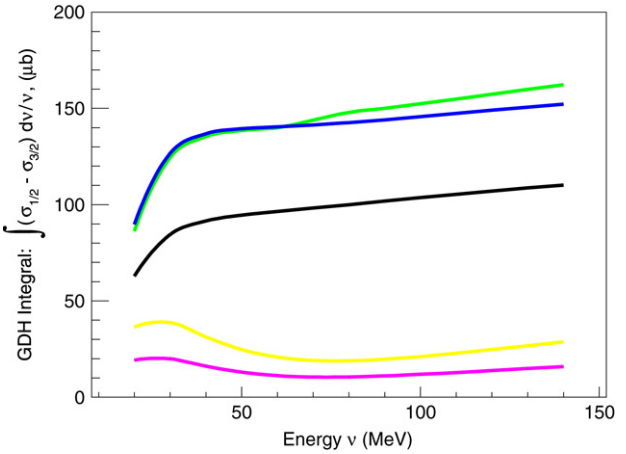

Fig. 27. (Color online) Theoretical predictions of the ^{3}He GDH integral from 20 MeV up to the pion production threshold. The five curves with different colors are: green line: CD-Bonn+MECs; blue line: RCO; yellow line: RCO + Δ isobar; black line: Explicit MECs; magenta line: Implicit MECs via the Siegert theorem. See text for details about these calculations.

The GDH integral on ^{3}He can be broken into three parts,

$$\int_{\nu_{thr}}^{\infty} \mathrm{GDH}_{^3\mathrm{He}} = \int_{\nu_{thr}}^{\nu_\pi} \mathrm{GDH}_{^3\mathrm{He}} + \int_{\nu_\pi}^{\sim 2\text{–}3\ \mathrm{GeV}} \mathrm{GDH}_{^3\mathrm{He}} + \int_{\sim 2\text{–}3\ \mathrm{GeV}}^{\infty} \mathrm{GDH}_{^3\mathrm{He}}. \tag{25}$$

The GDH sum rule predictions for ^{3}He, the proton and the neutron based on the known values of their anomalous magnetic moments are 496 μb, 204 μb and 233.5 μb, respectively. On the right hand side of Eq. (25), the second part has not been measured directly, but is estimated at being equal to about 247 μb on the basis of an extrapolation of recent experimental data [148]. The third part represents the contribution above the nucleon resonances which can be written into the following neutron and proton integrals in the plane wave impulse approximation:

$$\int_{\sim 2\text{–}3\ \mathrm{GeV}}^{\infty} \mathrm{GDH}_{^3\mathrm{He}} = P_n \times \int_{\sim 2\text{–}3\ \mathrm{GeV}}^{\infty} \mathrm{GDH}_n + P_p \times \int_{\sim 2\text{–}3\ \mathrm{GeV}}^{\infty} \mathrm{GDH}_p \tag{26}$$

where GDH_i refers to GDH sum rule for nucleon i, P_n is the effective polarization of the neutron, 87%; and P_p is the effective polarization of proton, −2.7% [149]. The high energy part of the GDH integral for the proton and the neutron have been estimated using a Regge type approach and found to be −26 μb and 35 μb [150], respectively. Therefore, the high energy part of the ^{3}He GDH integral is expected to be

$$\int_{\sim 2\text{–}3\ \mathrm{GeV}}^{\infty} \mathrm{GDH}_{^3\mathrm{He}} = 87\% \times 35 + 2.7\% \times 26 = 36.6\ \mu\mathrm{b}. \tag{27}$$

The first part of the right side of Eq. (25) is therefore estimated as being about 212 μb based on the experimental data and the plane wave impulse approximation picture. On the other hand, the state-of-the-art three-body calculations give values for this part of the integral between 16 μb and 136 μb [151,152]. In [151], the meson exchange currents (MECs) are included directly, i.e. the transverse E and M multipoles are calculated from spatial 1-body and 2-body currents. The relativistic current operator (RCO) calculation assumes current conservation and replaces the dominant parts of the electric multipoles by the Coulomb multipoles. It is very hard to achieve exact current conservation with realistic NN models, especially for nonlocal ones like CD Bonn. Therefore they yield different results. In [152], two models for the nuclear current operators are used. One is the explicit MECs in which the π- and ρ-like pieces are connected by the so-called Riska prescription [153] to the NN potential of AV18, and the other is with the current operator constructed using the Siegert theorem [154]. In Fig. 27, the calculations by Deltuva et al. [151] are shown as the green, blue and the yellow curves. The green line uses the CD Bonn potential plus MECs, the blue line uses RCO and the yellow line is RCO plus Δ isobar. The calculations by Golak et al. [152] are shown as the black line with explicit MECs and the magenta line is the result obtained using the Siegert theorem.

If indeed a polarized ^{3}He nucleus is a very effective polarized neutron, one expects an enormous strength in the first part of the integral (212 μb) of Eq. (25). Thus, measurements from the two-body photodisintegration threshold to the pion threshold can be used to study how effective polarized ^{3}He is as a polarized neutron target, as well as providing stringent tests of the state-of-the-art three-body calculations including future effective field theory calculations. Such measurements, in combination with the $Q^2 \to 0$ GDH integral measurement above the pion threshold from JLab, will provide a test of the GDH sum rule on the ^{3}He nucleus for the first time.

The HIγS facility is an ideal place for such a measurement. The experiment requires measurements of the total two-body and three-body breakup cross-sections as a function of incident photon energy starting from the two-body breakup

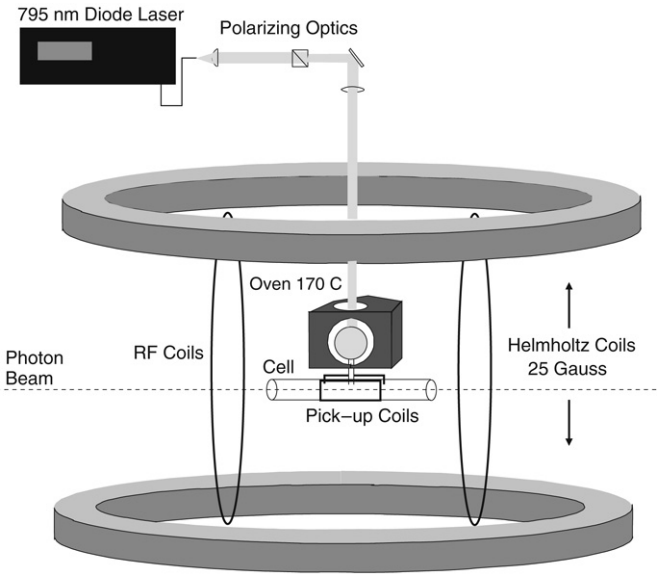

Fig. 28. A schematic drawing of the polarized ^{3}He target in the transverse spin configuration.

threshold of ^{3}He up to pion production threshold for circularly polarized photons scattering off a longitudinally polarized ^{3}He target. For relatively low incident photon energies, the detection of the proton is sufficient to separate the two-body process from the three-body process for which the neutron will be detected. For higher incident energies, coincidence detection of both neutron and proton is necessary for the three-body breakup channel. The high pressure polarized ^{3}He target which will be used will have a much thinner wall thickness so that the low energy charged particles can exit. The polarized ^{3}He targets [155] which will be used in these measurements are based on the spin-exchange optical pumping technique with a wall thickness of 500 μm. The polarized ^{3}He target is based on the principle of spin exchange between optically pumped alkali-metal vapor and noble-gas nuclei [156]. The design is similar to that used in electron scattering experiments in Hall A at Jefferson Lab (JLab) [157]. A central feature of the target will be sealed glass target cells, which will contain a ^{3}He pressure of about 10 atmospheres at room temperature. With a density of 2.5×10^{20} atoms/cm^3, and a cell length of 40 cm, the target thickness will be $1 = 1.0 \times 10^{22}$ atoms/cm^2. Due to the fact that the HIγS photon beam spot size is significantly larger than the electron beam size, the diameter of the HIγS target cell will be much larger than that of the ^{3}He target at JLab, with a diameter of 2.9 cm. Fig. 28 shows the schematics of the polarized ^{3}He target setup. Polarizations of 40%–45% have been achieved.

The target polarization will be monitored using the NMR technique of adiabatic fast passage (AFP) [158]. The signals are calibrated by comparing the ^{3}He NMR signals with those of water. Further, the polarization will also be measured during the experiment by the electron paramagnetic resonance (EPR) technique [159–162].

For a photon flux of 5×10^7/s with an energy spread of 7%, a target polarization of 40% and a target thickness of 1.0×10^{22}/cm^2, the projected HIγS measurement of the ^{3}He integral from the two-body threshold to the pion production threshold will have a statistical uncertainty of ± 11 μb obtained in a total beam time of 500 h.

7. The compton @ HIγS program

Nucleon polarizabilities comprise a set of fundamental quantities related to the structure of the nucleon, describing the response of the nucleon to external electromagnetic fields. These quantities can be accessed through low energy Compton scattering experiments. Compton scattering from nucleons at low energy is specified by low-energy theorems up to and including terms linear in photon energy. These terms are completely determined by the static properties of the nucleon, i.e. the nucleon charge, mass and its anomalous magnetic moment. At next to leading order in photon energy there appear new structure constants which are related to the dynamic response of the nucleon's internal degrees of freedom. The electric (α) and magnetic (β) scalar polarizabilities, which describe the response of the nucleon to external electric and magnetic fields, respectively, enter in terms which are second order in photon energy. At the third order four new parameters, γ_1 to γ_4, the spin polarizabilities, appear. While spin polarizabilities do not have as intuitive a physical interpretation as the electric and magnetic polarizabilities, they are nevertheless just as fundamental.

In the last two decades or so significant efforts have been devoted to Compton scattering measurements from the proton in order to extract the proton electric and magnetic polarizabilities [163]. A combined analysis of the low-energy differential cross section data yields $\alpha_P = [12.1 \pm 1.1(\text{stat})]^{+0.5}_{-0.5}(\text{th}) \times 10^{-4}$ fm^3 and $\beta_P = [3.4 \pm 1.1(\text{stat})]^{+0.1}_{-0.1}(\text{th}) \times 10^{-4}$ fm^3. While the proton's electric and magnetic polarizabilities are known relatively well, our knowledge of the neutron's polarizabilities

is much poorer than that of the proton due to the lack of free neutron targets in nature. The first experimental determination of the neutron's polarizability consisted of low-energy neutron scattering from heavy nuclei [164].

The neutron's electric and magnetic polarizabilities can also be extracted from experiments using deuterium targets. In recent years, coherent elastic Compton scattering by the deuteron, and the quasi-free Compton scattering from the deuteron have been investigated. The most precise information on the neutron's electric (α_n) and magnetic polarizabilities (β_n) is from the quasifree Compton scattering experiment carried out at MAMI B(Mainz) [165]: $\alpha_n = 12.5 \pm 1.8(\text{stat})^{+1.1}_{-0.6}(\text{syst}) \pm 1.1(\text{model})$, $\beta_n = 2.7 \mp 1.8(\text{stat})^{+0.6}_{-1.1}(\text{model}) \mp 1.1(\text{model})$, in units of 10^{-4} fm^4.

Compared to the nucleon electric and magnetic polarizabilities, very little is known about nucleon spin polarizabilities ($\gamma_i, i = 1$–4) which are further described later. Unpolarized Compton scattering differential cross-section measurements are not sensitive to the nucleon spin polarizabilities. Double-polarization asymmetries from circularly polarized photons Compton scattered off a polarized nucleon target have been shown to be sensitive to the nucleon spin polarizabilities [166–168]. Single spin observables and double-polarization observables from Compton scattering on nucleon and nuclear targets are being proposed at the upgraded HIγS facility. These new experiments will advance our knowledge of the nucleon polarizabilities greatly, therefore providing stringent tests of the theory of strong interactions as it is cast in various approximations.

7.1. Compton scattering at low energies

The general amplitude for Compton scattering based on parity, charge conjugation, and time reversal symmetry can be written [169] in terms of six structure dependent functions $A_i(\omega, \theta)$, $i = 1, \ldots 6$. The six structure dependent functions, $A_i(\omega, \theta)$ ($i = 1, \ldots, 6$) are separated into the pion-pole ("anomalous") contributions and the remaining ("regular") terms:

$$A_i(\omega, \theta) = A_i(\omega, \theta)^{\pi^0-\text{pole}} + A_i(\omega, \theta)^{\text{reg}}. \tag{28}$$

One can now carry out a low energy expansion of the six "regular" structure functions in powers of photon energy.

For each structure function the leading order terms in the ω expansion are given by *model-independent* Born contributions for scattering from a spin 1/2 point particle with anomalous magnetic moment and are fixed by low energy theorems of current algebra. The higher order terms in ω are model dependent quantities and the comparison between data and theoretical predictions provides sensitive tests of the validity of the theoretical approaches. The more familiar electric and magnetic polarizabilities enter the amplitude at the $O(\omega^2)$ and measure the response or deformation of the system to quasi-static electric and magnetic fields. The γ_i ($i = 1, \ldots, 4$), which enter the amplitude at the ω^3 order, are the so-called *spin polarizabilities*. They determine independently the response of a microscopic target with spin 1/2 to a quasi-static electromagnetic field when the spin degree of freedom is involved. For example, an induced dipole $\vec{p}_s$ can be constructed by $\vec{p}_s = \gamma_3 \vec{\Delta}(\vec{S} \cdot \vec{B})$, where $\vec{\Delta}$ is the d'Alembertian, $\vec{S}$ denotes the spin of the target, and $\vec{B}$ is the intensity of the external magnetic field.

The only quantities which have been experimentally determined to date are the so-called forward and backward spin polarizabilities γ_0 and γ_π. The forward and backward spin polarizabilities are linear combination of the γ_i:

$$\begin{aligned} \gamma_0 &= \gamma_1 - \gamma_2 - 2\gamma_4 \\ \gamma_\pi &= \gamma_1 + \gamma_2 + 2\gamma_4. \end{aligned} \tag{29}$$

Both γ_0 and γ_π can be obtained in a model dependent way by relying on a multipole analysis of single-pion-photoproduction data.

The backward spin polarizability $\gamma_\pi = \gamma_1 + \gamma_2 + 2\gamma_4$ has been extracted by the LEGS group using unpolarized Compton scattering data from the proton [170]. However, the extracted value of $\gamma_\pi = (-27.1 \pm 2.2) \times 10^{-4}$ fm^4 contradicts the predictions of standard dispersion theory [171–173] as well as those of chiral perturbation theory [169,197,198]. The theoretical prediction for γ_π from chiral effective field theory is -36.7×10^{-4} fm^4 [169]. The LEGS result is in disagreement with the TAPS result $\gamma_\pi = (-36.1 \pm 2.2) \times 10^{-4}$ fm^4 [174]. The most recent Mainz experiment [203] using the LARA detector extracted a backward polarizability value of $(-37.9 \pm 0.6_{\text{stat + syst}} \pm 3.5_{\text{model}}) \times 10^{-4}$ fm^4, and is in agreement with the earlier result from Mainz [174]. The new data confirm the previous observation that there is a systematic discrepancy between Mainz results and LEGS' results. The clarification of the situation will benefit from double polarization Compton scattering experiments [175] in which circularly polarized photons are scattered from a polarized proton target. The neutron backward spin polarizability was determined to be $\gamma_\pi^n = (58.6 \pm 4.0) \times 10^{-4}$ fm^4 [176].

As mentioned in Section 6, a sum rule exists for γ_0, which was originally discovered by Gell-Mann, Goldberger and Thirring (GGT) [177]:

$$\gamma_0 = \frac{1}{4\pi^2} \int_{\nu_0}^{\infty} \frac{\mathrm{d}\omega}{\omega^3} [\sigma_-(\omega) - \sigma_+(\omega)], \tag{30}$$

where ν_0 is the pion production threshold, and $\sigma_-(\omega)$, $\sigma_+(\omega)$ are the total photoabsorption cross-sections when the total helicity of the photon–nucleon system is 1/2 and 3/2 along the photon momentum direction, respectively.

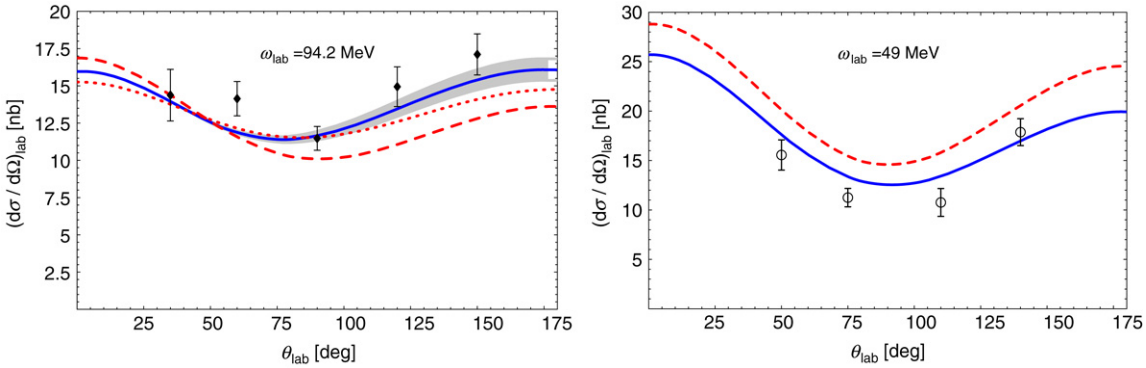

Fig. 29. Comparison of data and theory for Compton scattering from the deuteron. Right: Example of a prediction using proton polarizabilities with (solid) and without (dashed) *NN*-rescattering in intermediate states. Left: Example of 1-parameter fit result using the Baldin sum rule for the deuteron (solid, with stat. uncertainty), compared to χEFT without explicit $\Delta(1232)$ ($\mathcal{O}(p^3)$, dashed) and to a fit [166] at $\mathcal{O}(p^4)$ ($\alpha^s_{E1} = 11.5,\ \beta^s_{M1} = 0.3$, dotted). From Ref. [185].

The following results on γ_0 were reported [178] based on the multipole analysis of the photo-pion production data:

$$\gamma_0 \sim -1.34 \times 10^{-4}\ \text{fm}^4\ \text{(proton)} \qquad (31)$$
$$\gamma_0 \sim -0.38 \times 10^{-4}\ \text{fm}^4\ \text{(neutron)}.$$

The most recent extraction of the proton forward spin polarizability is from the Mainz GDH experiment [179], and the extracted value of γ_0 based on the Mainz data and the dispersion analysis is $\gamma_0 = [-1.01 \pm 0.08(stat) \pm 0.10(syst)] \times 10^{-4}$ fm^4 [180].

7.2. Compton scattering from deuterium and nucleon polarizabilities

In the past ten years, great progress has been made in studies of the proton polarizabilities through Compton scattering from the proton [181,174], largely facilitated by the advent of high duty-cycle tagged photon facilities. The 100% linearly polarized beams at HIγS make it possible to make a significant improvement on the accuracy of these results. As previously discussed in Ref. [63], sum-rule independent measurements of the electric (α_p) and magnetic (β_p) polarizabilities of the proton can be obtained using a 120 MeV beam with an intensity of 10^7 γ/s with uncertainties of about 5%. This is especially significant in the case of β_p where the present uncertainty is greater than 30%.

Investigations of the neutron polarizabilities, however, have lagged behind, primarily due to the lack of free neutron targets. As previously mentioned, these measurements are performed using deuterium, measuring either the quasi-free $d(\gamma, \gamma' n)p$ reaction or the elastic scattering $d(\gamma, \gamma)d$ reaction.

Only three measurements of the differential cross section for the $d(\gamma, \gamma)d$ reaction have been performed to date. Lucas et al. at Illinois [182] measured 4° at 49 MeV and 2° at 69 MeV. Lundin et al. at Lund [183] covered only a limited range of forward and backward angles at 55 and 66 MeV. Hornidge et al. at Saskatoon [184] extended the energy range up to 95 MeV and obtained a five-point angular distribution. Typical statistical uncertainties in the differential cross sections were around 10% for the 49–69 MeV data and ∼7% for the 95 MeV data.

On the theoretical side, a new "industry" of effective field theory (EFT) has arisen in the past ten years (starting with the development of chiral perturbation theory) and great attention has been focused on Compton scattering calculations for the deuteron. Until recently, the comparison of the predictions of these calculations with the available data has been quite unsatisfactory, especially with the back-angle data at 95 MeV. In fact, a fit to the available data [185] yielded a result in which β_N actually exceeds α_N, in striking contrast to the proton polarizability values ($\alpha_p = 12$ and $\beta_p = 3$). However, a new calculation which employed Chiral Effective Field Theory with explicit $\Delta(1232)$ degrees of freedom within the Small Scale Expansion up to leading-one-loop order has apparently resolved this problem [185]. Their results, which utilized the isoscalar Baldin sum rule [186], indicated good agreement with the available data at all energies and yielded values of the isoscalar polarizabilities of $\alpha_N = (11.3 \pm 0.7\ (\text{stat}) \pm 0.6\ (\text{Baldin})) \times 10^{-4}$ fm^3 and $\beta_N = (3.2 \mp 0.7\ (\text{stat}) \pm 0.6\ (\text{Baldin})) \times 10^{-4}$ fm^3, implying that the neutron and proton polarizabilities are essentially the same. The available data are shown along with the results of their global fits in Fig. 29. While this is a very encouraging result, the need for higher quality data remains obvious.

Recently, there have been a series of EFT calculations [187–190] which collectively suggest detailed experimental approaches to the problem of determining the isoscalar nucleon polarizabilities. These calculations have been performed using EFTs where the pions have been integrated out. Such pionless theories have been shown to be highly successful for systems whose characteristic momenta are below the pion mass.

One of the recent papers [189] recommends that "future high-precision deuteron Compton scattering experiments be performed at 25–35 MeV photon energy where the nucleon polarizability effects are appreciable and the pionless effective

field theory is most reliable''. These authors, in fact, state that a measurement (of the absolute value of the cross section) with a 3% error will constrain the isoscalar electric polarizability to an error 3×10^{-4} fm^3, or about 25% of the expected value of 12×10^{-4} fm^3.

There are, in fact, two separate considerations here. One is the absolute value of the cross section. As pointed out in Ref. [189], there is a 12% effect on this quantity at 30 MeV when using $\alpha_N = 10$; $\beta_N = 1.2 \times 10^{-3}$ fm^3, the leading order results of chiral perturbation theory, as opposed to setting α_N and β_N equal to zero. If the results of Chiral Perturbation Theory are accepted, then a 3% measurement of the absolute value of the cross section will indeed determine both α_N and β_N to within 25%. The second consideration comes from examining the shape of the angular distribution of the differential cross section. A 3% statistical uncertainty measurement will determine both α_N and β_N to an accuracy of 1×10^{-4} fm^3. We are therefore proposing to perform a precision measurement of the absolute differential cross section (∼5%) and of the angular distribution (eight angles with 3% statistics) at an incident γ-ray energy of 50 MeV. At this energy, the effect in the absolute cross section is about 25%, so that a 5% measurement will determine $\alpha_N = 10\beta_N$ to an accuracy of 2.0×10^{-4} fm^3, which is significantly better than the theoretical error.

The thickness of our liquid deuterium target will be determined by careful measurements of the cell geometry and the monitoring of the target cell pressure and temperature during the experiment. Following the method of [191] we expect to be able to determine our target thickness to an accuracy of 1%. The combination of uncertainties in beam integration (2%), detector efficiency and solid angle (2%), target thickness (1%), and peak fitting/background subtraction (2%) should allow us to make an absolute cross section measurement at the ∼6%–7% level of accuracy.

Measurements of the shape of the differential cross section will be dominated by the statistical accuracy (∼3% for our measurements). The use of 8 identical detectors (HINDA — see below) in a well defined geometry will essentially eliminate instrumental asymmetries. This will, in an early stage of the program, be verified directly by measuring an angular distribution with a single detector, rotated to eight different positions, and comparing the results to that obtained when eight different detectors are used. Detectors will also be interchanged to measure their relative efficiencies and to remove instrumental asymmetries.

In summary, we are proposing a comprehensive experimental program which will determine the isoscalar electric and magnetic polarizabilities of the nucleon. We are proposing to perform a careful measurement of the differential cross section for Compton scattering from the deuteron at an incident energies between 30 and 80 MeV. EFT calculations and a model independent sum rule will be used to determine the separate values of α_N and β_N from the differential cross section to an accuracy of ∼10%. At the same time, accurate (∼6%) measurements of the absolute cross section will determine the polarizabilities to an accuracy of ∼20% and will provide a consistency check of the above results. These measurements are expected to provide neutron polarizability measurements for both α_n and β_n to an overall accuracy of better than ∼20%.

7.3. The HINDA spectrometer

A proposal for the development of a large acceptance detection system (HINDA) was recently funded by the NSF through their MRI program [192]. This array will consist of eight large high-resolution NaI detectors surrounded by 3 in. thick segmented NaI shields. A schematic diagram of HINDA spectrometer is shown in Fig. 30. The central ''core'' detectors are 10 in. in diameter and 12 in. long. Their resolution at 20 MeV is typically better than 3%. The 3 in. thick NaI shields consist of eight optically isolated segments. The very good resolution (5% for 0.5 MeV γ rays) of these segments make it possible to extract the escape peaks, or to sum them back into the full energy peak in the core detector spectra. The entire assembly can also be used as a single detector, by summing the signals of the core detector plus the eight segments of the shield. The system also possesses excellent cosmic-ray rejection efficiency, in excess of 90%.

The detectors will be configured in a manner illustrated in Fig. 30. This installation allows the detectors to be in or out of a single scattering plane. Each detector is also equipped with a 6 in. thick Pb collimator. All core detectors and every shield segment is outfitted with an LED pulser to allow for gain monitoring and accurate dead time measurement.

7.4. Nucleon spin polarizabilities from double-polarization compton scattering

Spin polarizabilities of the nucleon can be probed directly via circularly polarized photons Compton scattered from a polarized nucleon target. Because the Thomson amplitude is real and the spin-dependent amplitudes are complex, it is necessary to use circularly polarized incident photons to obtain a cross section asymmetry linear in γ_i at $O(\omega^3)$. We are proposing the use of circularly polarized photons incident on the target, where the spin polarization of the target is either along the beam direction, or in the scattering plane transverse to the beam direction.

Hildebrandt et al. [167] studied the sensitivity of the spin-dependent Compton scattering cross section to the spin-polarizabilities of the proton in an $O(p^3)$ calculation. Here we briefly summarize our conclusions from an examination of these calculations.

For longitudinal target polarization, the effect of the pion-pole term (chiral anomaly) in the cross section asymmetry is dominant, and the spin-polarizability effect from nucleon structure is distinctly weaker. Nevertheless, at photon energies of approximately 100 MeV and lab angles near 110° there is significant sensitivity to the polarizabilities. For the transverse target polarization, the spin-polarizability effect is significant and comparable to the pion-pole term. This sensitivity is appreciable at lab angles greater than 70°, and photon energies of approximately 100 MeV.

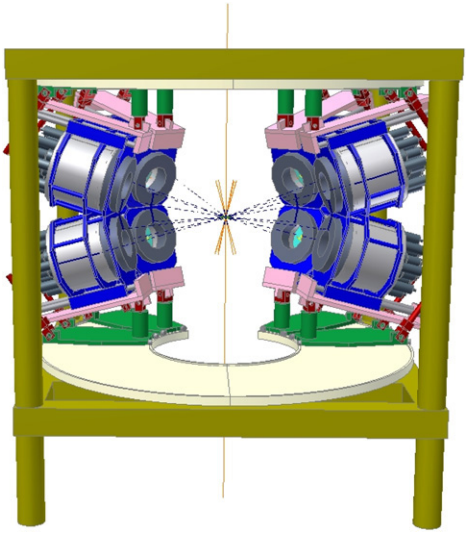

Fig. 30. The HINDA Spectrometer — An array of eight 10 in. × 12 in. NaI detectors each of which is surrounded by a 3 in. thick segmented NaI shield.

7.4.1. Spin-dependent Compton scattering experiment on the proton

Based on the theoretical considerations presented previously, the proposed experimental setup for the proton spin-polarizability measurements at HIγS is as follows:

- Photon detection over a range of angles from 60° up to approximately 160°. Because the largest physics asymmetry is seen with transverse target polarization, the detector elements should be in the plane of the target polarization.
- Incident photon energies ranging from approximately 30 MeV (almost no spin polarizability effect) up to 140 MeV. The photon polarization will be circular.
- Data taking with longitudinal and transverse target polarizations.

7.4.2. Polarized proton targets

The U.Va. group [193] in collaboration with the TUNL Capture Group, is currently building a frozen-spin (Butanol) polarized target for the GDH experiment at HIγS. This target will be similar to one under construction for JLab Hall B. The HIγS target has a length of 7.3 cm and a diameter of 2.0 cm. The density of Butanol will be $\sim$1.0 g/cm^3. A dilution factor of 13% and a packing factor of $\sim$60% lead to a target thickness of $\sim 3.5 \times 10^{23}$ polarized protons per cm^2. The polarization is expected to be 70%–80%.

It is a great advantage to use a polarized scintillating target. Having a signal from the target that would tag a Compton (or π^0) event is a great advantage for reducing backgrounds in these experiments. This possibility was seriously considered for the spin-Compton [194] and the polarized pion threshold photoproduction experiments at Mainz [195] several years ago. However, the huge flux of low energy photons in the Mainz bremsstrahlung beam made use of the scintillating target problematic. Even with low-Z beam hardeners to reduce the low energy photon flux, the anticipated minimum ionizing background load in the scintillator was over 1 MHz. Fortunately, because of the nearly monochromatic character of the HIγS beam, the low energy backgrounds will be greatly reduced, making the HIγS beam ideal for the use of a polarized scintillating target. Presently the U.Va.–TUNL group in collaboration with the University of Massachusetts group (led by Rory Miskimen), is planning to build a scintillating-frozen-spin target. This target will be based on the experience of the group at Paul Sherrer Institute which has constructed a polarized scintillating frozen-spin target [196].

We plan to construct the polarized target from scintillating disks 2 cm in diameter and 0.5 cm thick, where the scintillating material is doped with the polarizing agent tempo in the casting process. The target will utilize ten scintillating disks in a row, with a 2 mm gap between disks. The disk array is held together with three thin graphite rods glued at 120° intervals around the outside of the disks. The total target thickness is 5 cm, with 2.6×10^{23} polarized protons/cm^2. The target stack is designed to fit into the space where Butanol beads are placed in the non-scintillating version of the frozen spin target. To allow scintillation light to escape from the target region, we propose to construct the first vacuum wall that separates the helium dilution region from the inner vacuum space with a transparent material, such as acrylic or pyrex. To capture scintillation light coming out of the target region, blue-to-green wavelength shifting fibers (WLS), 1 mm square, will be wound around the transparent vacuum wall. Approximately 7% of the photons incident on the WLS fibers are captured and transported to the fiber ends. The fiber ends will be coupled to avalanche photodiodes or solid state photomultipliers, with active areas from 1 to 2 mm in diameter. The detectors will be positioned within the inner vacuum space so that the generated heat load will have minimal effect on the 100 mK target region.

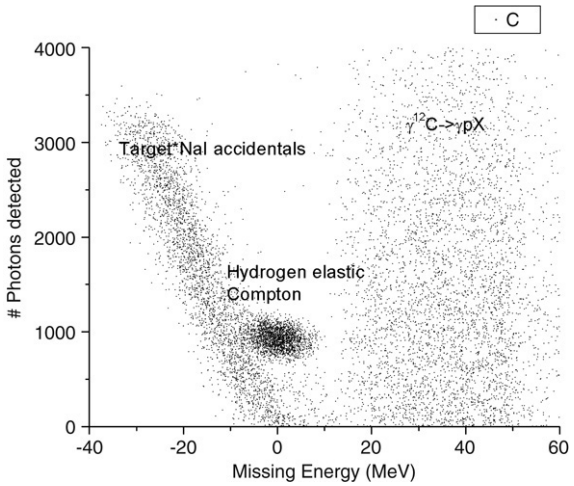

Fig. 31. Scatter plot of binding energy in the scintillating target versus proton kinetic energy obtained from the simulation.

The most important feature of the scintillating target is its ability to distinguish quasi-free Compton scattering events off the protons in ^{12}C from Compton events on hydrogen. A Fermi gas model program was developed to study how these events might be separated. The light collection efficiency and the quantum efficiency of the photodetector which will view the scintillating target material are estimated at 10% and 15%, respectively. Energy resolution in the NaI detector was taken as 3% (FWHM). The NaI detector has a size of 10 in. $\times$ 12 in., and is positioned 1 m from the target.

Fig. 31 shows a scatter plot of measured binding energy in the scintillating target, defined as $BE = E_i - E_f - T_p$, versus measured proton kinetic energy T_p for 100 MeV Compton scattering at 90° in the x–z (horizontal) plane. In the 2-dimensional plot the free Compton events can be easily identified and separated from the quasi-free events.

In summary, our monte-carlo studies indicate that the scintillating target should perform very well in a spin-dependent Compton scattering experiment.

7.4.3. Rate calculations and projections

Cross section estimates are presented using the scintillating target. For these estimates we assume 2.6 $\times$ 10^{23} protons per cm^2 in the target, with a polarization of 84%, and 100% detection efficiency for recoil protons. For the photon flux we assume 1 $\times$ 10^7 γ/s, with 100% circular polarization. The proposed detector geometry consists of the HINDA array with eight NaI detector elements, arranged in two arcs, four on beam left and four on beam right, at angles of approximately 60°, 90°, 120°, and 150°. The efficiency of the NaI's is taken as 60%, and they are positioned 80 cm from the target.

Our studies indicate that sensitivity to the polarizabilities is maximized by measuring the helicity-dependent cross sections, not just the asymmetry. Also, the most effective test of the model-dependent calculations used to extract the polarizabilities is obtained by measuring helicity-dependent cross sections. For these reasons we plan to measure cross sections in the experiment. We expect that it will be possible to measure the photon flux at the 3% level. In addition to taking production data at beam energies of 100 and 120 MeV, we also plan to take data at a beam energy of 30 MeV as a way to test the systematic errors in the experiment. At 30 MeV theoretical uncertainties in the Compton cross sections are expected to be very small.

Fig. 32 show the helicity-dependent cross sections for a longitudinal and transverse polarized target at a γ-ray energy of 110 MeV. Also shown are the projected error bars for a measurement at HIγS assuming 100 h of beam time for each target polarization. Fig. 32 demonstrates that there is considerable sensitivity to the spin polarizabilities in the helicity-dependent cross sections below pion threshold, particularly at backward angles with the longitudinal polarization, and at mid to backward angles with transverse polarization.

To estimate how accurately individual spin polarizabilities can be measured in an experiment at HIγS, we produced pseudo-data using estimated acceptances, efficiencies and running times. Then the spin polarizabilities were fit to the pseudo-data using the theoretical model of Hildebrandt et al. [167]. For this estimate we assumed 10^7 γ/s, incident γ-ray energy of 110 MeV with 100% circular polarization, the HINDA NaI detector array, and a polarized scintillating target 5 cm long with 80% polarization. The running times are 200 h with longitudinal polarization, and 200 h with transverse polarization. The fitting uncertainties for the four spin polarizabilities ranged from 0.2 to 0.4 in units of 10^{-4} fm^3. For the largest spin polarizability, γ_1 in Hildebrandt model, the fractional uncertainty is $\pm$4%.

In summary, we propose to make a measurement of the proton spin polarizabilities at HIγS using a scintillating polarized target. In phase I of the HIγS program, data will be taken at energies of 30 MeV and 100 MeV, with running times of approximately 50 and 400 h, respectively. In phase II of the program, data will be taken near pion threshold, with running times of approximately 200 h. Simulations show that data taken in the phase I program will have sensitivity at the level of

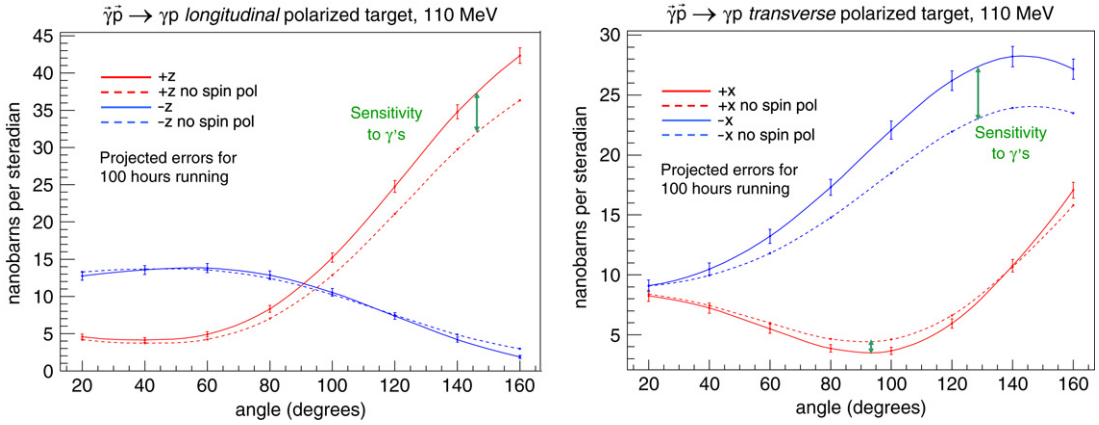

Fig. 32. Projected measurements (shown by the data points whose error bars are statistical only) of the proton spin polarizabilities as a function of photon angle at a γ-ray energy of 110 MeV for a longitudinally polarized target (left) and transverse polarized target (right). The solid (dashed) curves are with (without) spin-polarizabilities included (see Ref. [167]).

Table 6
The calculated spin polarizabilities (from Ref. [197]) are given along with the anticipated statistical uncertainties expected from the HIγS measurements which would be obtained within the specified beam time

Proton	HIγS uncertainty	Neutron	HIγS uncertainty
$\gamma_1^p = 1.1$	± 0.05	$\gamma_1^n = 3.7$	± 0.43
$\gamma_2^p = -1.5$	± 0.36	$\gamma_2^n = -0.1$	± 0.03
$\gamma_3^p = 0.2$	± 0.24	$\gamma_3^n = 0.4$	
$\gamma_4^p = 3.3$	± 0.17	$\gamma_4^n = 2.3$	± 0.57

The proton results assume 400 h of beam time while the neutron results are based upon the assumption of a 2000 h elastic Compton scattering experiment on polarized ^{3}He.

0.2 to 0.4×10^{-4} fm^3, which is sufficient to test and differentiate between different models for the low-energy spin structure of the proton.

7.4.4. Spin-dependent Compton scattering on the "neutron"

The static-spin polarizabilities of the nucleons have been calculated by several groups [169,197–199]. The earlier calculations were performed at order p^3 (where p denotes the small momenta and pion masses, collectively) and ϵ^3 (where ϵ denotes all other small parameters such as the nucleon-delta mass splitting), and were only sensitive to the isoscalar spin polarizabilities, so the calculated values were the same for the neutron and the proton. More recently [197,198], the first nonvanishing contributions to the isovector part of the spin polarizabilities were calculated in a p^4 order calculation using heavy baryon chiral perturbation theory (HBCHPT). The results indicate that overall these corrections are almost an order of magnitude smaller than the isoscalar values with the exception of γ_1. The values of the neutron and proton spin polarizabilities obtained in Ref. [197] are presented in Table 6.

Note that the values given here correspond to the structure part only, since the non-structure pole term contributions have been removed. Finally, we note that there are some differences between the values of the neutron and proton spin polarizabiliites presented in Refs. [197,198]. However, the authors of Ref. [198] state that these difference are due to the fact that the authors of Ref. [197] chose not to include a particular one-particle-reducible diagram in their definition of the polarizabilities. They go on to say that if this term is included, then the two calculations are in agreement-which is reassuring.

Note that we are proposing to extract the values of the *static* spin polarizabilities for the proton and the neutron. Future experiments will attempt to measure the dynamic (energy dependent) spin polarizabilities. As discussed in Ref. [167], the energy dependence of the four leading spin polarizabilities of the proton and neutron should provide profound insight into the dispersive behavior of the internal degrees of freedom of the nucleon, caused by relaxation effects, baryonic resonances and mesonic production thresholds.

Since there is no free neutron target in nature, effective neutron targets, i.e. nuclear targets, the deuteron and ^{3}He, are commonly used for the study of the neutron. A polarized ^{3}He nucleus is very useful in probing the neutron electromagnetic and spin structure because of the unique spin structure of the ^{3}He ground state. It is dominated by a spatially symmetric S wave component in which the proton spins pair off and the spin of the ^{3}He nucleus is carried by the unpaired neutron [200].

The first experiment being planned at HIγS will be elastic polarized Compton scattering off a polarized ^{3}He target. The advantage is a much larger Compton scattering cross-section and a relatively straightforward theoretical calculation of the Compton scattering process. A recent calculation of the elastic scattering process was performed using chiral perturbation

theory to next-to-leading order [201]. The quantities Δ_z and Δ_x are defined by taking the beam helicity to be along $\hat{z}$ so that Δ_z (Δ_x) is the difference between the differential cross section when the target is spin polarized along $+\hat{z}(+\hat{x})$ and $-\hat{z}(-\hat{x})$. These authors find that Δ_z and Δ_x are sensitive to two different linear combinations of γ_1, γ_2, and γ_4 of the neutron and the measurement will provide an unambiguous determination of γ_1, as well as constraints on γ_2 and γ_4. The HINDA array will be used to detect the scattered γ rays. The polarized ^{3}He target is a high-pressure target based on the spin-exchange optical pumping technique. The double polarization asymmetry will be formed by flipping the circular polarization of the incident photon beam. The target spin direction will be reversed from time to time to minimize effects due to systematic false asymmetries. In this experiment, we will align the target spin parallel and perpendicular to the incident photon momentum direction in the scattering plane to measure both the parallel asymmetry ($A_\parallel$) and the perpendicular asymmetry ($A_\perp$).

7.4.5. Projected measurements from the elastic Compton scattering process

In projecting the asymmetry results, we assumed a photon flux of 2×10^7 γ/s for a photon energy spread of 5 MeV at an incident photon energy of 114 MeV and a target thickness of 1.1×10^{22} atoms/cm^2 with a target polarization of 45%. The circular polarization of the photon beam is taken to be 100%. A solid angle acceptance of 0.05 sr was assumed for each scattering angle bin. A total beam time of 2000 h was assumed in the projection with 1000 h for each of the two target spin orientations. The projected results given in Table 6 show clearly the high precision that HIγS measurements will achieve even with a modest photon flux (2×10^7/s), therefore providing the much needed sensitivity in probing the neutron spin polarizabilities.

7.4.6. Anticipated results on neutron spin polarizabilities

The nucleon spin polarizabilities have been calculated by several groups [197,198,202] at the next-to-leading order (NLO) in chiral perturbation theory. Predictions on all four neutron spin polarizabilities at NLO in heavy-baryon chiral perturbation theory by Kumar, McGovern and Birse [198] are:

$$\begin{aligned}
\gamma_1 &= [-21.3]\tau_3 + 4.5 - (2.1 + 1.3\tau_3)\\
\gamma_2 &= 2.3 - (3.1 + 0.7\tau_3)\\
\gamma_3 &= [10.7]\tau_3 + 1.1 - (0.8 + 0.1\tau_3)\\
\gamma_4 &= [-10.7]\tau_3 - 1.1 + (3.9 + 0.5\tau_3)\\
\gamma_0 &= 4.5 - (6.9 + 1.5\tau_3)\\
\gamma_\pi &= [-42.7]\tau_3 + 4.5 + (2.7 - 1.1\tau_3),
\end{aligned} \tag{32}$$

where $\tau_3 = -1$ for neutron, and the term in brackets are the third-order anomalous contribution. The values of the neutron spin polarizability are $\gamma_1 = 25.0$, $\gamma_2 = -0.1$ $\gamma_3 = -10.3$, $\gamma_4 = 13.0$, $\gamma_0 = -0.9$, and $\gamma_\pi = 51.0$. One can see that the rather large absolute polarizability values for γ_1, γ_3, γ_4 and γ_π are due to the anomalous contribution. Several authors [169,180] define the nucleon spin polarizabilities differently from those of Kumar, McGovern and Birse [198] and Ji et al. [202] by removing the pion pole contribution. The corresponding neutron spin polarizabilities values obtained at the NLO in heavy-baryon chiral perturbation theory [198] using the definition of Refs. [169,180] are therefore: $\gamma_1 = 3.7$, $\gamma_2 = -0.1$ $\gamma_3 = 0.4$, $\gamma_4 = 2.3$, $\gamma_0 = -0.9$, and $\gamma_\pi = 8.3$.

These measurements will allow the extraction of the individual neutron spin polarizabilities for the first time. These projected results show clearly the high impact of the projected HIγS measurements in probing the neutron spin polarizabilities. Achieving the desired intensity of the photon flux is essential to the success of the proposed elastic Compton scattering program.

8. Summary and outlook

There were two major objectives for this review paper: to describe the upgraded HIγS facility and its operating parameters, and to provide an overview of the initial nuclear physics research program which is presently underway at this facility.

We have seen that the upgraded HIγS facility produces γ-ray beams which are unique. The collimated beams are nearly mono-energetic, are ~100% polarized and have intensities which have not been previously available. These beams can be used without tagging, which leads to much greater counting rates in many experiments. An additional bonus is the time structure of the beams which make time-of-flight techniques very easy to implement.

A number of nuclear structure studies, especially nuclear resonance fluorescence studies to make parity assignments, can be executed at HIγS in a unique, sensitive and straightforward manner. We have tried to describe some of the early results obtained in such studies as well as to indicate where future studies are headed.

HIγS also provides a powerful tool for new studies of few-nucleon systems. The extremely clean and intense beam, combined with state-of-the-art detection systems, is making it possible to resolve some long-standing discrepancies in few body photodisintegration cross section measurements. Future studies at HIγS should settle some of theses problems once and for all.

Opportunities to tackle fundamental problems in nuclear astrophysics are also apparent with HIγS. This review focused on a HIγS project designed to perform accurate measurements of the $^{12}C(\alpha,\gamma)^{16}O$ cross section by means of the inverse reaction. At the time of writing, the apparatus for this work, the Optical Time Projection Chamber, is fully constructed and awaiting beamtime. Results should be available in the very near future.

The combination of the 100% linearly and/or circularly polarized beams with polarized targets opens up additional new vistas. This review described the activities which are presently underway aimed at measuring the Gerasimov Drell Hearn integral below pion- threshold. These experiments are uniquely suited to the nature of the HIγS γ-ray beams. All of the detector systems have been assembled, the polarized ^{3}He target is ready to go, and the frozen spin d-target is nearing completion. It is expected that results for both ^{3}He and d will be available within the next two years.

Of course it is natural to use a γ-ray beam in order to perform Compton scattering measurements. Once again, the unique features of the HIγS beams offer special opportunities for such studies. For example, the intense 100% linearly polarized beams will lead to much more precise measurements of the electric and magnetic polarizabilities of the proton. And the combination of circularly polarized beams and polarized targets will make it possible to measure the spin-polarizabilities of the nucleons for the very first time. The timing for these results, expected in the 2–3 years time frame, could not be better. Theoretical advances in both Chiral effective field theory and Lattice QCD calculations are and will be producing results in the same time frame. The confrontation of these theories with the HIγS measurements should be an enlightening and an exciting event.

These initial experiments represent just that: a startup package of first round experiments. It seems clear to us that as the HIγS facility evolves and matures, many new and more exciting experiments will be identified and performed. We are looking forward to a bright future at this facility.

Acknowledgments

This work was partially supported by the US-DOE under grant nos. DE-FG02-97ER41033, DE-FG02-03ER41231, and DE-FG02-94ER40870.

References

[1] A.H. Compton, Bull. Nat. Res. Council (US) 20 (1922) 19; Phys. Rev. 21 (1923) 483.
[2] R.H. Milburn, Phys. Rev. Lett. 10 (1963) 75.
[3] F.R. Arutyunian, V.A. Tumanian, Phys. Lett. 4 (1963) 176.
[4] O.F. Kulikov, et al., Phys. Lett. 13 (1964) 344.
[5] C. Bemporad, et al., Phys. Rev. B 138 (1965) 1546.
[6] J.J. Murray, P.R. Klein, SLAC Report No. SLAC-TN-67-19, unpublished, 1967.
[7] J. Ballam, et al., Phys. Rev. Lett. 23 (1964) 498.
[8] L. Casano, et al., Laser Unconv. Opt. J. 55 (1975) 3.
[9] G. Matone, et al., Lect. Notes Phys. 62 (1977) 3.
[10] L. Federici, et al., Nuovo Cimento Lett. 27 (1980) 339.
[11] L. Federici, et al., Nuovo Cimento B 59 (1980) 247.
[12] D. Babusci, et al., Nuclear Instrum. Methods A 305 (1991) 19.
[13] A.M. Sandorfi, et al., IEEE Trans. NS-30 (1984) 3083.
[14] V.N. Litvinenko, et al., Phys. Rev. Lett. 78 (1997) 4569.
[15] D. Babusci, et al., Nuovo Cimento A 103 (1990) 1555.
[16] A.A. Kazakov, et al., JETP Lett. 40 (1984) 445.
[17] G.Ya. Kezerashvili, et al., Nuclear Instrum. Methods A 328 (1993) 506.
[18] G.Ya. Kezerashvili, et al., AIP Conf. Proc. 343 (1995) 260.
[19] G.Ya. Kezerashvili, et al., Nuclear Instrum. Methods B 145 (1998) 40.
[20] T. Nakano, et al., Nuclear Phys. A 629 (1998) 559c.
[21] T. Nakano, et al., Nuclear Phys. A 684 (2001) 71c.
[22] D. Babusci, et al., Rivista Nuovo Cimento 19 (1996) 1.
[23] A. D'Angelo, et al., Nuclear Instrum. Methods A 455 (2000) 1.
[24] C. Schaerf, Phys. Today 2005 (2005) 44.
[25] L.D. Landau, E.M. Lifshitz, et al., Quantum Electrodynamics, 2nd ed., in: Course of Theoretical Physics, vol. 4, Reed Ed. and Prof. Pub., 1982.
[26] P. Chen, et al., Nuclear Instrum. Methods A 355 (1995) 107.
[27] Y.K. Wu, C. Sun, An integration code for e^-–γ Compton scattering (unpublished), 2007.
[28] Y.K. Wu, Proc. of the 2007 Part. Acc. Conf., 2007, pp. 1215–1217.
[29] Y.K. Wu, et al., Technical Design Report for the Upgrade of the High Intensity Gamma-ray Source, DFELL Internal Report, March, 2004.
[30] V. Popov, et al., Proc. of the 2005 Part. Acc. Conf., 2005, pp. 3901–3903.
[31] S. Mikhailov, et al., Proc. of the 2005 Part. Acc. Conf., 2005, pp. 3544–3546.
[32] S.M. Hartman, et al., Proc. of the 2005 Part. Acc. Conf., 2005, pp. 3792–3794.
[33] V. Popov, et al., Proc. of the 2005 Part. Acc. Conf., 2005, pp. 3919–3921.
[34] G.Y. Kurkin, et al., Proc. of the 2005 Part. Acc. Conf., 2005, pp. 3159–3161.
[35] S.F. Mikhailov, et al., Proc. of the 2007 Part. Acc. Conf., 2007, pp. 1212–1214.
[36] V. Popov, et al., Proc. of the 2007 Part. Acc. Conf., 2007, pp. 521–523.
[37] J. Li, et al., Proc. of the 2007 Part. Acc. Conf., 2007, pp. 3582–3584.
[38] V. Popov, et al., Proc. of the 2007 Part. Acc. Conf., 2007, pp. 4051–4053.
[39] S.M. Hartman, et al., Proc. of the 2007 Part. Acc. Conf., 2007, pp. 515–517.
[40] Y.K. Wu, et al., Proc. of the 2007 Part. Acc. Conf., 2007, pp. 4063–4065.
[41] S.F. Mikhailov, et al., Proc. of the 2007 Part. Acc. Conf., 2007, pp. 1209–1211.
[42] Y.K. Wu, et al., Proc. of the 2003 Part. Acc. Conf., 2003, pp. 2482–2484.
[43] V.N. Litvinenko, et al., Nuclear Instrum. Methods A 375 (1996) 46.
[44] Y. Wu, et al., Nuclear Instrum. Methods A 375 (1996) 74.

[45] Y. Wu, et al., IEEE Trans. Nucl. Sci. v. 44 (1997) 1753.
[46] Y.K. Wu, et al., Proc. of the 2005 Part. Acc. Conf., 2005, pp. 3934–3936.
[47] V.N. Litvinenko, et al., Nuclear Instrum. Methods A 407 (1998) 8.
[48] V.N. Litvinenko, et al., Nuclear Instrum. Methods A 429 (1998) 151.
[49] V.N. Litvinenko, et al., Nuclear Instrum. Methods A 470 (2001) 66.
[50] V.N. Litvinenko, et al., Nuclear Instrum. Methods A 475 (2001) 195.
[51] S.H. Park, et al., Nuclear Instrum. Methods A 407 (1998) 224.
[52] S.H. Park, et al., Nuclear Instrum. Methods A 475 (2001) 425.
[53] V.N. Litvinenko, et al., Nuclear Instrum. Methods A 475 (2001) 247.
[54] V.N. Litvinenko, et al., Nuclear Instrum. Methods A 475 (2001) 97.
[55] V.N. Litvinenko, et al., Nuclear Instrum. Methods A 475 (2001) 407.
[56] Y.K. Wu, et al., Phys. Rev. E. 68 (2003) 046502.
[57] Y.K. Wu, et al., Proc. of the 2003 Part. Acc. Conf., 2003, pp. 391–393.
[58] Y.K. Wu, et al., Proc. of the 2005 FEL Conference, 2005, pp. 407–410.
[59] Y.K. Wu, et al., Phys. Rev. Lett. 96 (2006) 224801.
[60] M.W. Ahmed, et al., Nuclear Instrum. Methods A 516 (2004) 440.
[61] I.V. Pinayev, et al., Nuclear Instrum. Methods A 475 (2001) 222.
[62] Under Dept. of Energy Grant DE-FG02-01ER41175-0.
[63] Henry R. Weller, Mohammad W. Ahmed, Modern Phys. Lett. A18 (23) (2003) 1569–1590.
[64] N. Pietralla, et al., Phys. Rev. Lett. 88 (2002) 012502.
[65] N. Pietralla, et al., Phys. Rev. C65 (2002) 047305.
[66] J.E. Garcia-Ramos, et al., Phys. Rev. C61 (2000) 064309.
[67] C. Fransen, et al., Phys. Rev. C 70 (2004) 044317.
[68] V. Werner, et al., Phys. Lett. B 550 (2002) 140.
[69] D. Savran, et al., Phys. Rev. C 71 (2005) 034304.
[70] J. Margraf, et al., Phys. Rev. C 47 (1996) 1474.
[71] H. Friedrichs, et al., Nuclear Phys. A 567 (1994) 266.
[72] J. Margraf, et al., Phys. Rev. C 52 (1995) 2429.
[73] H. Maser, et al., Phys. Rev. C 53 (1996) 2749.
[74] M. Scheck, et al., Phys. Rev. C 67 (2003) 064313.
[75] G. Alaga, K. Alder, A. Bohr, B.R. Mottelson, K. Dan. Vidensk. Selesk. Mat. Fys. Medd. 29 (1955) 1.
[76] T.C. Li, et al., Phys. Rev. C 73 (2006) 054306.
[77] S. Nummela, et al., Phys. Rev. C 63 (2001) 44316.
[78] R. Skibinski, et al., Phys. Rev. C 67 (2003) 054001–054002.
[79] V.D. Efros, W. Leidemann, G. Orlandini, E.L. Tomusiak, Phys. Lett. B 484 (2000) 223.
[80] B.S. Pudliner, et al., Phys. Rev. C 56 (1997) 1720.
[81] R.B. Wiringa, V.G.J. Stoks, R. Schiavilla, Phys. Rev. C 51 (1995) 38.
[82] A. Deltuva, A.C. Fonseca, P.U. Sauer, Phys. Rev. C 71 (2005) 054005.
[83] A. Deltuva, Private communication, 2006.
[84] S. Naito, et al., Phys. Rev. C 73 (2006) 034003.
[85] R. Machleidt, Phys. Rev. C 63 (2001) 024001.
[86] H. Ohgaki, et al., IEEE Trans. Nucl. Sci. 38 (1991) 386.
[87] B. Sawatsky, et al., Private communication, 2004.
[88] R. Machleidt, F. Sammarruca, Y. Song, Phys. Rev. C 53 (1996) R1483.
[89] D. Gazit, et al., Phys. Rev. Lett. 96 (2006) 112301.
[90] B. Nilsson, et al., Phys. Lett. B 626 (2005) 65.
[91] D.P. Wells, et al., Phys. Rev. C 46 (1992) 449.
[92] B.L. Berman, D.D. Faul, P. Meyer, D.L. Olson, Phys. Rev. C 22 (1980) 2273.
[93] J.R. Calarco, B.L. Berman, T.W. Donnelly, Phys. Rev. C 27 (1983) 1866.
[94] T. Shima, et al., Phys. Rev. C 72 (2005) 044004;
See also T. Shima, et al., Nuclear Phys. A 687 (2001) 127c.
[95] S. Quaglioni, et al., Phys. Rev. C 69 (2004) 044002.
[96] B. Nilsson, et al., Phys. Rev. C 75 (2007) 014007.
[97] W.A. Fowler, Rev. Modern Phys. 56 (1984) 149.
[98] T.A. Weaver, E. Woosley, Phys. Rep. 227 (1993) 65.
[99] M. Phillips, Astrophys. J. Lett. 413 (1993) 105;
M. Hamuy, et al., Astron. J. 106 (1993) 2392;
M. Hamuy, et al., Astron. J. 109 (1995) 1;
A. Riess, W. Press, R. Kirshner, Astrophys. J. 473 (1996) 88.
[100] S. Perlmutter, Phys. Today 56 (2003) 4 and reference theirin.
[101] P. Hoeflich, C. Gerardy, E. Linder, H. Marion, in: D. Alloin, W. Gieren (Eds.), Steller Candles for the Extra Galactic Scale, Springer, 2003, p. 203. astro-ph/0301334.
[102] M. Gai, From the Sun to the Great Attractor, in: Lecture Notes in Physics, Springer, 2000, p. 49. http://astro.uconn.edu/Mex_Sum_Gai.pdf.
[103] F.C. Barker, Aust. J. Phys. 24 (1971) 777.
[104] X. Ji, et al., Phys. Rev. C 41 (1990) 1736.
[105] J. Humblet, et al., Phys. Rev. C 44 (1991) 2530.
[106] Z. Zhao, R.H. France III, K.S. Lai, S.L. Rugari, M. Gai, E.L. Wilds, Phys. Rev. Lett. 70 (1993) 2066; Phys. Rev. Lett. 70 (1993) 3524 (erratum).
[107] L. Buchmann, et al., Phys. Rev. Lett. 70 (1993) 726.
[108] R.E. Azuma, et al., Phys. Rev. C 50 (1994) 1194.
[109] R.H. France III, E.L. Wilds, N.B. Jevtic, J.E. McDonald, M. Gai, Nuclear Phys. A 621 (1997) 165c.
[110] R.H. France, E.L. Wilds, J.E. McDonald, M. Gai, Phys. Rev. C (2007) 065802.
[111] G.M. Hale, Nuclear Phys. A 621 (1997) 177c.
[112] X.D. Tang, et al., Phys. Rev. Lett. 99 (2007) 052502.
[113] R. Kunz, et al., Phys. Rev. Lett. 86 (2001) 3244.
[114] M. Assuncao, et al., Phys. Rev. C 73 (2006) 055801.
[115] A Proposal: "A free-electron laser generated gamma-ray beam for nuclear physics", W. Tornow, R. Walter, H.R. Weller, V. Litvinenko, B. Mueller, P. Kibrough, Duke/TUNL, 1997.
[116] Toni Feder, Phys. Today 55 (12) (2002) 26.
[117] T. Shima, Y. Nagai, T. Kii, T. Baba, T. Takahashi, H. Ohgaki, Nuclear Phys. A 629 (1998) 475c.
[118] C. Matei, et al., Phys. Rev. Lett. 97 (2006) 242503.
[119] P. Annis, et al., Nuclear Instrum. Methods A 367 (1995) 367.

[120] U. Titt, A. Breskin, R. Chechik, V. Dangendorf, H. Schmidt-Bocking, H. Schuhmacher, Nuclear Instrum. Methods A 416 (1998) 85;
U. Titt, V. Dangendorf, H. Schuhmacher, Nuclear Phys. B 78 (Supp.) (1999) 444;
U. Titt, Dissertation zur Erlangung des Doktorgrades, Ph.D. Thesis, J.W. Goethe Universitat Frankfurt, 1999.
[121] L. Weismann, M. Gai, A. Breskin, R. Chechik, V. Dangendorf, K. Tittelmeier, H.R. Weller, J. Instr. 1 (2006) 05002.
[122] A.H. Young, M. Gai, T.J. Kading, M.W. Ahmed, H.R. Weller, V. Dangendorf, K. Tittelemeier, Bull. Amer. Phys. Soc. 52 (9) (2007) 70.
[123] S.D. Drell, A.C. Hearn, Phys. Rev. Lett. 16 (1966) 908;
S.B. Gerasimov, Sov. J. Nuclear Phys. 2 (1966) 430.
[124] X. Ji, Y. Li, Phys. Lett., B 591 (2004) 76 and references therein.
[125] P. Mohr, B. Taylor, Rev. Modern Phys. 72 (2000) 351.
[126] H. Arenhövel, et al., Phys. Rev. Lett. 93 (2004) 202301 and references therein.
[127] H. Arenhövel, et al., Few-Body Systems 3 (1998) 111 and references therein.
[128] W. Tornow, et al., Phys. Lett. B 574 (2003) 8.
[129] B. Sawatzky, Ph.D Thesis, Department of Physics, University of Virginia, 2005.
[130] M. Blackston, et al., Phys. Rev. C (2008) (in press).
[131] E.C. Schreiber, et al., Phys. Rev. C 61 (2000) 061604.
[132] H.R. Weller, et al., Atomic Data Nuclear Tables 58 (1994) 219.
[133] M.W. Ahmed, et al., Phys. Rev. C 77 (2008) 044005 and references therein.
[134] J.-W. Chen, M. Savage, Phys. Rev. C 60 (1999) 065205.
[135] H. Arenhövel, et al., Phys. Lett. B 407 (1997) 1.
[136] R.J. Holt, et al., Phys. Rev. Lett. 50 (1983) 577.
[137] J.P. Soderstrum, et al., Phys. Rev. C 35 (1987) 1246.
[138] J. Drooks, Ph.D. Thesis, Department of Physics, Yale University, 1976.
[139] W. Del Bianco, et al., Phys. Rev. Lett. 47 (1981) 1118.
[140] R.G. Seyler, H.R. Weller, Phys. Rev. C 20 (1979) 453.
[141] Virginia Tech Partial-Wave Analysis Facility (SAID), George Washington University, http://gwdac.phys.gwu.edu/.
[142] L.D. Knutson, Phys. Rev. C 59 (1999) 2152.
[143] National Nuclear Data Center, Evaluated Nuclear Data File (ENDF), Brookhaven National Laboratory, http://www.nndc.bnl.gov/.
[144] F. James, CERN Program Library Long Writeup D506, Version 94.1, CERN Geneva, Switzerland.
[145] http://geant4.web.cern.ch/.
[146] H.R. Weller, et al., Atomic Data and Nuclear Tables 50 (1992) 29.
[147] B. Sawatsky, et al., Private communication.
[148] Jefferson Lab E94010 Collaboration, M. Amarian, et al., Phy. Rev. Lett. 89 (2002) 242301.
[149] J.L. Friar, et al., Phys. Rev. C 42 (1990) 2310.
[150] N. Bianchi, E. Thomas, Phys. Lett. B 450 (1999) 439.
[151] A. Deltuva, et al., Phys. Rev. C 69 (2004) 034004;
A. Deltuva, P. Sauer, Private communications.
[152] J. Golak, et al., Phys. Rev. C. 72 (2005) 044002.
[153] J. Carlson, R. Schiavilla, Rev. Modern Phys. 70 (1998) 743.
[154] J. Golak, et al., Phys. Rev. C 62 (2000) 054005.
[155] K. Kramer, et al., Nucl. Inst. Meth. Phys. Res. A 582 (2007) 318.
[156] M.A. Bouchiat, T.R. Carver, C.M. Varnum, Phys. Rev. Lett. 5 (1960) 373;
N.D. Bhaskar, W. Happer, T. McClelland, Phys. Rev. Lett. 49 (1982) 25;
W. Happer, et al., Phys. Rev. A 29 (1984) 3092.
[157] J.S. Jensen, Ph.D. Thesis, California Institute of Technology, 2000 (unpublished). available from: http://www.jlab.org/e94010/.
[158] A. Abragam, Principles of Nuclear Magnetism, Oxford University Press, New York, 1961.
[159] S.R. Scheafer, G.D. Cates, T.R. Chien, D. Gonatas, W. Happer, T.G. Walker, Phys. Rev. A 39 (1989) 5613.
[160] N.R. Newbury, A.S. Barton, P. Bogorad, G.D. Cates, M. Gatzke, H. Mabuchi, B. Saam, Phys.Rev. A 48 (1993) 558.
[161] A.S. Barton, N.R. Newbury, G.D. Cates, B. Driehuys, H. Middleton, B. Saam, Phys. Rev. A 49 (1994) 2766.
[162] M.V. Romalis, G.D. Cates, Phys. Rev. A 58 (1998) 3004.
[163] M. Schumacher, Prog. Part. Nuclear Phys. 55 (2005) 567.
[164] J. Schmiedmayer, P. Riehs, J.A. Harvey, N.W. Hill, Phys. Rev. Lett. 66 (1991) 1015;
L. Koester, et al., Phys. Rev. C 51 (1995) 3363.
[165] K. Kossert, et al., Phys. Rev. Lett. 88 (2002) 162301.
[166] J. McGovern, Private communication.
[167] R.P. Hildebrandt, H. Griesshammer, T.R. Hemmert, Eur. Phys. J. A 20 (2004) 329. nucl-th/0308054.
[168] B. Pasquini, et al., ArXiv:0705.0282.
[169] T.R. Hemmert, B.R. Holstein, J. Kambor, G. Knöchlein, Phys. Rev. D 57 (1998) 5746.
[170] J. Tonnison, et al., Phys. Rev. Lett. 80 (1998) 4382.
[171] A.I. L'vov, A.M. Nathan, Phys. Rev. C 59 (1999) 1064.
[172] D. Drechsel, G. Krein, O. Hanstein, Phys. Lett. B 420 (1998) 248.
[173] D. Babusci, G. Giordano, A.I. L'vov, G. Matone, A.M. Nathan, Phys. Rev. C 58 (1998) 1013.
[174] V. Olmos de Leon, et al., Eur. Phys. J. A 10 (2001) 207.
[175] F. Wissmann, in: D. Drechsel, L. Tiator (Eds.), Proceeding of the Symposium on the Gerasimov–Drell–Hearn Sum Rule and the Nucleon Spin Structure in the Resonance Region, World Scientific, 2000, p193.
[176] K. Kossert, et al., Eur. Phys. J. A 16 (2003) 259.
[177] M. Gell-Mann, M.L. Goldberger, W.E. Thirring, Phys. Rev. 95 (1954) 1612.
[178] A.M. Sandorfi, C.S. Whisnant, M. Khandaker, Phys. Rev. D 50 (1994) R6681.
[179] J. Ahrens, et al., GDH Collaboration, Phys. Rev. Lett. 87 (2001) 022003.
[180] D. Drechsel, B. Pasquini, M. Vanderhaeghen, Phys. Rep. 378 (2003) 100.
[181] B.E. MacGibbon, et al., Phys. Rev. C 52 (1995) 2097.
[182] M.A. Lucas, Ph.D. Thesis, University of Illinois at Urbana-Champaign, 1994.
[183] M. Lundin, et al., Phys. Rev. Lett. 90 (2003) 192501-1.
[184] D.L. Hornidge, et al., Phys. Rev. Lett. 84 (2000) 2334.
[185] R.P. Hildebrandt, H.W. Griesshammer, T.R. Hemmert, 2005. arXiv.nucl-th/0512063.
[186] A.M. Baldin, Nuclear Phys. 18 (1960) 310.
[187] H.W. Griesshammer, G. Rupak, Phys. Lett. B 529 (2002) 57.
[188] G. Rupak, Private communication, 2003.
[189] Jiunn-Wei Chen, Xiangdong Ji, Yingchuan Li, Phys. Lett. B620 (2005) 33. nucl-th/0408003.
[190] Jiunn-Wei Chen, Xiangdong Ji, Yingchuan Li, Phys. Rev. C 71 (2005) 044321. nucl-th/0408004.
[191] J. Alcorn, et al., Nuclear Instrum. Method A 522 (2004) 294–346.
[192] Steve Whisnant, Private communication, 2006.

[193] D. Crabb, B. Norum, U. Va, Private communication.
[194] Letter of intent to MAMI, "Spin Dependent Compton Scattering: Measuring the Spin Polarizabilities of the Proton", R. Miskimen contact person, 1998.
[195] Proposal to Mainz, Measurement of Polarized Target Asymmetries in Threshold Neutral Pion Photo-production on the Proton: Test of Chiral Dynamics, contact persons: M. Pavan, R. Beck, A.M. Bernstein.
[196] B. van den Brandt, et al., SPIN2002, Brookhaven, NY, 2002.
[197] G.C. Gellas, T.R. Hemmert, U.-G. Meissner, Phys. Rev. Lett. 85 (2000) 14.
[198] K.B. Vijay Kumar, J.A. McGovern, M.C. Birse, Phys. Lett. B 479 (2000) 167.
[199] V. Bernard, N. Kaiser, U.-G Meissner, Internat. J. Modern Phys. E 4 (1995) 193.
[200] B. Blankleider, R.M. Woloshyn, Phys. Rev. C 29 (1984) 538.
[201] D. Choudury, A. Nogga, D.R. Phillips, Phys. Rev. Lett. 98 (2007) 232303.
[202] X. Ji, C.-W. Kao, J. Osborne, Phys. Rev. D 61 (2000) 074003.
[203] G. Galler, et al., Phys. Lett. B 503 (2001) 245–255.